

Spectro-Photometric Evolution of Elliptical Galaxies. III.

Infall models with gradients in mass density and star formation

R. Tantaló¹, C. Chiosi^{2,1}, A. Bressan³, P. Marigo¹, L. Portinari¹

¹ Department of Astronomy, Vicolo dell'Osservatorio 5, 35122 Padua, Italy

² European Southern Observatory, Karl-Schwarzschild-strasse 2, D-85748, Garching bei Muenchen, Germany

³ Astronomical Observatory, Vicolo dell'Osservatorio 5, 35122 Padua, Italy

Received: October 1997, Accepted:

Abstract. In this study we present a simple model of elliptical galaxies aimed at interpreting the gradients in colours and narrow band indices observed across these systems. Salient features of the model are the gradients in mass density and star formation and infall of primordial gas aimed at simulating the collapse of a galaxy into the potential well of dark matter. Adopting a multi-zone model we follow in detail the history of star formation, gas consumption, and chemical enrichment of the galaxy and also allow for the occurrence of galactic winds according to the classical supernova (and stellar winds) energy deposit. The outline of the model, the time scale of gas accretion and rate of star formation as a function of the galactocentric distance in particular, seek to closely mimic the results from Tree-SPH dynamical models. Although some specific ingredients of the model can be questioned from many points of view (of which we are well aware), the model has to be considered as a gross tool for exploring the consequences of different recipes of gas accretion and star formation in which the simple one-zone scheme is abandoned. With the aid of this model we discuss the observational data on the gradients in metallicity, colours, and narrow band indices across elliptical galaxies.

Key words: Galaxies: ellipticals – Galaxies: evolution – Galaxies: stellar content – Galaxies: gradients

1. Introduction

Gradients in broad-band colours and line strength indices have been observed in elliptical galaxies (cf. Worthey et al. 1992; González 1993; Davies et al. 1993; Carollo et al. 1993; Carollo & Danziger 1994a,b; Balcells & Peletier 1994; Fisher et al. 1995, 1996). Since variations in colours

and line strength indices are eventually reduced to variations in age and chemical composition (metallicity), or both, of the underlying stellar populations, the interpretation of the gradients bears very much on the general mechanism of galaxy formation and evolution. Unfortunately, separating age from metallicity effects is a cumbersome affair, otherwise known as the *age-metallicity degeneracy* (cf. Worthey 1994 and references therein) which makes it difficult to trace back the history of star formation and chemical enrichment both in time and space. Despite this intrinsic difficulty, line strength indices such as H_β , Mg_2 , $\langle Fe \rangle$, and $[Mg/Fe]$ and broad-band colours and their gradients are customarily used to infer age and composition and their variations across galaxies.

Particularly significant in this context, is the different slope of the Mg_2 and $\langle Fe \rangle$ gradients observed across elliptical galaxies. The gradient in Mg_2 is often steeper than the gradient in $\langle Fe \rangle$, which is customarily interpreted as indicating that the ratio $[Mg/Fe]$ is stronger toward the center. Similar conclusion is reached interpreting the systematic increase of Mg_2 with the galaxy luminosity (mass): the ratio $[Mg/Fe]$ seems to increase with the galaxy mass (the so-called α -enhancement). This observational hint has been taken as one of the most important constraints to be met by any chemo-spectro-photometric model of elliptical galaxies (cf. Matteucci 1994, 1997 for recent reviews of the subject).

Owing to the primary importance of this topic, Tantaló et al. (1998) addressed the question to which extent the gradients in Mg_2 and $\langle Fe \rangle$ translate into gradients in chemical abundances and abundance ratios. To this aim, the above indices were calculated for a mix of stellar populations with known pattern of abundances as a function of the age and position to check whether a higher $[Mg/Fe]$ finds one-to-one correspondence with a stronger Mg_2 as compared to $\langle Fe \rangle$.

The need of a simple tool to follow the chemical history of a galaxy both in time and space spurred the model

Send offprint requests to: C. Chiosi

presented in this study. The bottom line is to abandon the widely adopted one-zone approximation however without embarking in a fully dynamical description which would hamper the quick analysis of the problem. The model allows for the infall of primordial gas into the potential well of dark matter (seeking to closely mimics results from fully hydrodynamical models) and the existence of gradients in mass density and star formation whose net result is to given rise to gradients in age and composition of the underlying stellar populations.

The plan of the paper is as follows. Section 2 sketches the model and presents the basic notation. Section 3 describes the spatial distribution of luminous and dark matter and their gravitational potentials. Section 4 presents in some detail the equations governing the chemical evolution together with the law of star formation and the initial mass function we have adopted. Section 5 deals with our modelling of the collapse and derives the law for the gas accretion time scale, and the specific efficiency of star formation as a function of the galacto-centric distance. Section 6 presents the empirical mass-radius (effective and total) relationships we have derived from fitting observational data. Section 7 clarifies some details of the mass zoning of the models. Section 8 deals with galactic winds and summarizes our prescription for the energy injection by supernova explosions, and stellar winds. Section 9 presents the general properties of the models and examines the internal consistency of the results. Specifically, it shows the evolution of the gas content, star formation rate and metallicity, and the spatial gradients in metallicity and relative distribution of stars per metallicity bin. Section 10 contains the photometric properties of the models (broad band colours and line strength indices), i.e. the color-magnitude relation, the mass to blue luminosity ratio, the UV excess, the surface brightness profiles, the gradients in broad-band colours and indices Mg_2 and $\langle Fe \rangle$, and the plane H_β -[MgFe] putting into evidence some difficulties encountered with the gradients in these quantities. Finally, Section 11 draws some concluding remarks.

2. Modeling elliptical galaxies

2.1. Sketch of the models and basic notation

Elliptical galaxies are assumed to be made of baryonic and dark material both with spherical distributions but different density profiles. Let $M_{L,T}(T_G)$ and $M_{D,T}(T_G)$ be the total luminous and dark mass, respectively, existing in the galaxy at the present time (T_G is the galaxy age). The two components have different effective (half mass) radii, named $R_{L,e}(T_G)$ and $R_{D,e}(T_G)$ (thereinafter shortly indicated as $R_{L,e}$ and $R_{D,e}$), and their masses are in the ratio $M_{D,T}(T_G)/M_{L,T}(T_G) = \theta$. Although θ may vary from galaxy to galaxy, for the purposes of this study it is supposed to be constant.

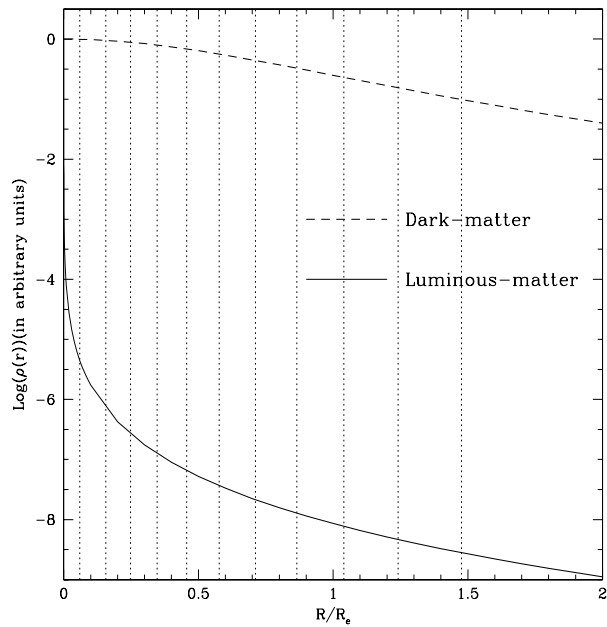


Fig. 1. The density profiles of baryonic and dark material in the prototype galaxy of $1 \times M_{L,T,12}$. For the baryonic component the asymptotic density is displayed (see the text for more details)

An essential feature of the model is that while dark matter is assumed to have remained constant in time, the luminous material is let fall at a suitable rate (to be defined below) into the potential well of the former. Owing to this hypothesis, no use is made of dark matter but for the calculation of the gravitational potential and the whole formulation of the problem stands on the mass and density of luminous material which are let grow with time from zero to their present day value.

The asymptotic model. The model whose radial density profile upon integration over radius and time yields the mass $M_{L,T}(T_G)$ is referred to as the asymptotic model. If $\rho_L(R, t)$ is the radial density profile of luminous matter at any age t and $\dot{\rho}_L(R, t)$ is the rate of variation by gas accretion, the following relation holds

$$M_{L,T}(T_G) = \int_0^{T_G} dt \int_0^{R_{L,T_G}} 4\pi R^2 \dot{\rho}_L(R, t) dR. \quad (1)$$

Mass and space zoning. The asymptotic model is divided into a number of spherical shells with equal value of the asymptotic luminous mass, typically 5% of $M_{L,T}(T_G)$. Since the density $\rho_L(R, T_G)$ is changing with radius (decreasing outward), the thickness and volume of the shells are not the same. They are indicated by

$$\Delta R_{j/2} = R_{j+1} - R_j$$

$$\Delta V(R_{j/2}) = \frac{4}{3}\pi(R_{j+1}^3 - R_j^3)$$

where R_{j+1} and R_j are the outer and inner radii of the shells, and $j = 0, \dots, J-1$ with $R_0 = 0$ (the center) and $R_J = R_{L,T_G}$ (the total radius). The radii R_j are not yet defined.

Thereinafter we will make use of the following notation and change of the radial coordinate:

- Each zone of a model is identified by its mid radius $R_{j+1/2} = (R_{j+1} + R_j) * 0.5$ shortly indicated by $R_{j/2}$.
- Radial distances are expressed in units of the effective radius of the luminous material in the asymptotic model, i.e. $r_{j/2} = R_{j/2}/R_{L,e}$.
- All masses are expressed in units of $10^{12} \times M_\odot$. Finally galactic models are labelled by their asymptotic total luminous mass $M_{L,T}(T_G)$ in the same units, shortly indicated by $M_{L,T,12}$.

Let us now define for each shell the mean density of total luminous material $\bar{\rho}_L(r_{j/2}, t)$, of stars $\bar{\rho}_s(r_{j/2}, t)$, and gas $\bar{\rho}_g(r_{j/2}, t)$, so that the corresponding masses are

$$\Delta M_L(r_{j/2}, t) = \bar{\rho}_L(r_{j/2}, t) \times \Delta V(r_{j/2}) \times R_{L,e}^3$$

$$\Delta M_g(r_{j/2}, t) = \bar{\rho}_g(r_{j/2}, t) \times \Delta V(r_{j/2}) \times R_{L,e}^3$$

$$\Delta M_s(r_{j/2}, t) = \bar{\rho}_s(r_{j/2}, t) \times \Delta V(r_{j/2}) \times R_{L,e}^3$$

By definition

$$\Sigma_{j=0}^{J-1} \Delta M_L(r_{j/2}, T_G) = M_{L,T}(T_G) \quad (2)$$

and

$$\Delta M_g(r_{j/2}, t) + \Delta M_s(r_{j/2}, t) = \Delta M_L(r_{j/2}, t). \quad (3)$$

Identical relationships can be defined for the dark matter by substituting its constant density profile. Since there would be no direct use of these relations, we just say that the space zoning of the dark matter distribution is the same as for the luminous component, so that the contribution of dark matter to the total gravitational potential in each zone is properly calculated (see below).

The dimension-less formulation. Finally, we define the dimension-less variables

$$G_g(r_{j/2}, t) = \frac{\Delta M_g(r_{j/2}, t)}{\Delta M_L(r_{j/2}, T_G)} = \frac{\bar{\rho}_g(r_{j/2}, t)}{\bar{\rho}_L(r_{j/2}, T_G)}$$

$$G_s(r_{j/2}, t) = \frac{\Delta M_s(r_{j/2}, t)}{\Delta M_L(r_{j/2}, T_G)} = \frac{\bar{\rho}_s(r_{j/2}, t)}{\bar{\rho}_L(r_{j/2}, T_G)} \quad (4)$$

where $\bar{\rho}_L(r_{j/2}, T_G)$ is the mean density of luminous mass within each shell at the present time.

Furthermore for each shell we introduce the gas components $G_{g,i}(r_{j/2}, t) = G_g(r_{j/2}, t) \times X_i(r_{j/2}, t)$ where $X_i(r_{j/2}, t)$ are the abundances by mass of the elemental species i . Summation of $X_i(r_{j/2}, t)$ over all the species in each shell is equal to unity.

2.2. The Infall scheme

The density of the luminous component in each shell is let increase with time according to

$$\left[\frac{d\bar{\rho}_L(r_{j/2}, t)}{dt} \right] = \bar{\rho}_{L0}(r_{j/2}) \exp \left[-\frac{t}{\tau(r_{j/2})} \right] \quad (5)$$

where $\tau(r_{j/2})$ is the local time scale of gas accretion for which a suitable prescription is required.

The function $\bar{\rho}_{L0}(r_{j/2})$ is fixed by imposing that at the present galactic age T_G the density of luminous material in each shell has grown to the value given by the adopted profile $\bar{\rho}_L(r, T_G)$

$$\bar{\rho}_{L0}(r_{j/2}) = \frac{\bar{\rho}_L(r_{j/2}, T_G)}{\tau(r_{j/2}) [1 - \exp(-\frac{T_G}{\tau(r_{j/2})})]} \quad (6)$$

It follows that the time dependence for $\bar{\rho}_L(r_{j/2}, t)$ is given by

$$\bar{\rho}_L(r_{j/2}, t) = \frac{\bar{\rho}_L(r_{j/2}, T_G)}{[1 - \exp(-\frac{T_G}{\tau(r_{j/2})})]} \times \left[1 - \exp(-\frac{t}{\tau(r_{j/2})}) \right] \quad (7)$$

For the asymptotic mass density in each shell we adopt the geometric mean of the values at inner and outer radii, i.e.

$$\bar{\rho}_L(r_{j/2}, T_G) = \sqrt{\rho_L(r_{j+1}, T_G) \times \rho_L(r_j, T_G)}. \quad (8)$$

To summarize, each shell is characterized by:

- The radius $r_{j/2}$.
- The asymptotic mass $\Delta M_L(r_{j/2}, T_G)$, which is a suitable fraction of the total asymptotic luminous mass $M_{L,T,12}$.
- The mass of dark matter $\Delta M_D(r_{j/2}, T_G)$. Since this mass is constant with time no other specification is required.
- The asymptotic mean density $\bar{\rho}_L(r_{j/2}, T_G)$ of baryonic mass (gas and stars).
- The gravitational potential for the luminous component $\varphi_L(r_{j/2}, t)$ varying with time, and the corresponding gravitational potential of dark-matter $\varphi_D(r_{j/2}, T_G)$, constant with time. Both will be defined below.

3. The spatial distribution of luminous and dark matter, and gravitational binding energies

Density profile of the luminous matter. The asymptotic spatial distribution of luminous matter is supposed to follow the Young (1976) density profile. This is derived from assuming that the $R^{1/4}$ -law holds and the mass to luminosity ratio is constant throughout the galaxy (cf. Poveda et al. 1960, Young 1976, Ciotti 1991). We remind the

reader that the density $\rho_L(R, T_G)$ and the gravitational potential $\varphi_L(R, T_G)$ are expressed by Young (1976) as a function of the effective radius for which a suitable relationship with the total luminous mass is required (see below).

The adoption of the Young (1976) density profile imposes that the resulting model at the age T_G has (i) a radially constant mass to luminosity ratio; (ii) a luminosity profile obeying the $R^{1/4}$ law.

Density profile of the dark matter. The mass distribution and gravitational potential of the dark-matter are derived from the density profiles by Bertin et al. (1992) and Saglia et al. (1992) however adapted to the Young formalism for the sake of internal consistency. In brief we start from the density law

$$\rho_D(R) = \frac{\rho_{D,0} \times R_{D,0}^4}{(R_{D,0}^2 + R^2)^2} \quad (9)$$

where $R_{D,0}$ and $\rho_{D,0}$ are two scale factors of the distribution. The density scale factor $\rho_{D,0}$ is derived from imposing the relation $M_{D,T} = \theta M_{L,T}$ and the definition of $M_{D,T}$ by means of its density law

$$M_{D,T} = 4\pi \int_0^\infty R^2 \rho(R) dR = 4\pi \rho_{D,0} R_{D,0}^3 m(\infty) \quad (10)$$

with

$$m(\infty) = \int_0^\infty \frac{R^2}{r_{D,0}^3 \left(1 + \left(\frac{R}{R_{D,0}}\right)^2\right)^2} dR \quad (11)$$

This integral is solved numerically. Finally, the density profile of dark-matter is

$$\rho_D(R) = \frac{M_{D,T}}{m(\infty)} \frac{1}{4\pi R_{D,0}^3} \frac{1}{\left(1 + \left(\frac{R}{R_{D,0}}\right)^2\right)^2}. \quad (12)$$

The radial dependence of the gravitational potential of dark matter is

$$\varphi_D(R) = -G \int_0^R \frac{M_D(R)}{r^2} dR \quad (13)$$

which upon integration becomes

$$\varphi_D(R) = -4\pi G \rho_{D,0} R_{D,0}^2 \widetilde{\varphi}_D \left(\frac{R}{R_{D,0}} \right) \quad (14)$$

where $\widetilde{\varphi}_D \left(\frac{R}{R_0} \right)$ is given by

$$\int_0^{R/R_{D,0}} \frac{m(R/R_{D,0})}{R_{D,0} \left(\frac{R}{R_{D,0}}\right)^2} dR \quad (15)$$

This integral is solved numerically and stored as a look-up table function of $R/R_{D,0}$.

We assume $R_{D,0} = \frac{1}{2} R_{D,e}$, where $R_{D,e}$ is the effective radius of dark matter. This can be derived from relation(10) looking for the radial distance within which half of the dark-matter mass is contained. Finally, all the models below are calculated adopting $\theta = 5$ in the ratio $M_{D,T}(T_G)/M_{L,T}(T_G) = \theta$.

The gravitational binding energies. The binding gravitational energy for the gas in each shell is given by:

$$\Omega_g(r_{j/2}, t) = \bar{\rho}_g(r_{j/2}, t) \Delta V(r_{j/2}) \varphi_L(r_{j/2}, t) + \bar{\rho}_g(r_{j/2}, t) \Delta V(r_{j/2}) \varphi_D(r_{j/2}, T_G) \quad (16)$$

4. The chemical equations

The chemical evolution of elemental species is governed by the same set of equations as in Tantaló et al. (1996, TCBF96) and Portinari et al. (1998) however adapted to the density formalism and improved as far the ejecta and the contribution from the Type Ia and Type II supernovae are concerned (cf. Portinari et al. 1998). Specifically, we follow in detail the evolution of the abundance of thirteen chemical elements (H, ^4He , ^{12}C , ^{13}C , ^{14}N , ^{16}O , ^{20}Ne , ^{24}Mg , ^{28}Si , ^{32}S , ^{40}Ca , ^{56}Fe , and the isotopic neutron-rich elements nr obtained by α -capture on ^{14}N , specifically ^{18}O , ^{22}Ne , ^{25}Mg). Furthermore, the stellar yields in usage here take into account the effects of different initial chemical compositions (cf. Portinari et al. 1998).

The equations governing the time variation of the $G_i(r, t)$ and hence $X_i(r, t)$ are:

$$\begin{aligned} \frac{dG_i(r_{j/2}, t)}{dt} = & -X_i(r_{j/2}, t) \Psi(r_{j/2}, t) + \\ & \int_{M_{min}}^{M_{Bm}} \Psi(r_{j/2}, t - \tau_M) Q_{M,i}(t - \tau_M) \phi(M) dM + \\ & \Lambda \int_{M_{Bm}}^{M_{BM}} \phi(M_B) dM_B \times \\ & \left[\int_{\mu_{min}}^{0.5} f(\mu) \Psi(r_{j/2}, t - \tau_{M_2}) Q_{M,i}(t - \tau_{M_2}) d\mu \right] + \\ & (1 - \Lambda) \int_{M_{Bm}}^{M_{BM}} \Psi(r_{j/2}, t - \tau_M) Q_{M,i}(t - \tau_M) \phi(M) dM + \\ & \int_{M_{BM}}^{M_{max}} \Psi(r_{j/2}, t - \tau_M) Q_{M,i}(t - \tau_M) \phi(M) dM + \\ & \left[\frac{dG_i(r_{j/2}, t)}{dt} \right]_{inf} \end{aligned} \quad (17)$$

where all the symbols have their usual meaning. Specifically $\Psi(r_{j/2}, t)$ is the normalized rate of star formation for the shell, $Q_{M,i}(t)$ are the restitution fractions of the elements i from stars of mass M (cf. Talbot & Arnett 1973),

$\phi(M)$ is the initial mass function (IMF), whose lower and upper mass limits are M_{min} and M_{max} (see below). τ_M is the lifetime of a star of mass M , for which the dependence on the initial chemical composition is also taken into account using the tabulations by Bertelli et al. (1994). The various integrals appearing in eq.(17) represent the separated contributions of Type II and Type Ia supernovae as introduced by Matteucci & Greggio (1986). In particular, the second integral stands for all binary systems having the right properties to become Type Ia supernovae. M_{Bm} and M_{BM} are the lower and upper mass limit for the total mass M_B of the binary system, $f(\mu)$ is the distribution function of their mass ratios, and μ_{min} is the minimum value of this, finally Λ is the fraction of such systems with respect to the total. It is assumed here that binary stars as a whole obey the same IMF of single stars. We adopt $B_m = 3M_\odot$, $B_M = 12M_\odot$, and $\Lambda = 0.02$. The stellar ejecta are from Marigo et al. (1996, 1997), and Portinari et al. (1998) to whom we refer for all details.

4.1. Star formation rate and IMF

The stellar birth rate, i.e. the number of stars with mass M born in the interval dt and mass interval dM , is expressed by

$$dN = \Psi(R, t, Z)\phi(M) dM dt \quad (18)$$

with obvious meaning of the symbols.

Neglecting the possible dependence on the gas composition, the rate of star formation (SFR), $\Psi(r_{j/2}, t, Z)$, is assumed to depend on the gas density according to the Schmidt (1959) law (see also Larson 1991)

$$\Psi(r_{j/2}, t) = \frac{d\bar{\rho}_g(r_{j/2}, t)}{dt} = \nu(r_{j/2})\bar{\rho}_g(r_{j/2}, t)^\kappa \quad (19)$$

where the specific efficiency of star formation $\nu(r_{j/2})$ is a suitable function to be specified below.

Upon normalization, the star formation rate becomes:

$$\Psi(r_{j/2}, t) = \nu(r_{j/2}, t)[\bar{\rho}_L(r_{j/2}, T_G)]^{\kappa-1} G_g(r_{j/2}, t)^\kappa. \quad (20)$$

All the models we are going to describe are for $\kappa = 1$.

For the IMF $\phi(M)$ we have adopted the Salpeter law:

$$\phi(M) \propto M^{-x} \quad (21)$$

where $x = 2.35$. The IMF is normalized by imposing the fraction ζ of mass in the IMF above a certain value M_* . i.e.

$$\zeta = \frac{\int_{M_*}^{M_U} \phi(M) \times M \times dM}{\int_{M_L}^{M_U} \phi(M) \times M \times dM} \quad (22)$$

A useful choice for M_* is the minimum star mass contributing to the nucleo-synthetic enrichment of the interstellar medium over a time scale comparable to the total

lifetime of a galaxy. This is approximately equal to $1M_\odot$. The upper limit is $M_U = 120M_\odot$ corresponding to the maximum mass in our data base of stellar models. The parameter ζ is fixed by imposing that our models match the mean mass to blue luminosity ratio for elliptical galaxies (Bender et al. 1992, 1993), this yields $\zeta = 0.50$. With this normalization the minimum star mass of the IMF is $M_L \sim 0.18M_\odot$.

5. Modelling the collapse

To proceed further, we need to supply our models with the radial dependence of the time scale of gas accretion $\tau(r_{j/2})$ and specific efficiency of star formation $\nu(r_{j/2})$.

The dynamical models of galaxy formation and evolution with the Tree-SPH technique (cf. Carraro et al. 1997 and references therein) hint the solution to this problem. In brief, looking at the paradigmatic case of the adiabatic collapse of a galaxy (dark plus baryonic material) of $10^{12}M_\odot$, initial mean density of $1.6 \times 10^{-25} \text{ g cm}^{-3}$, free-fall time scale of 0.25 Gyr, and age of 0.22 Gyr, we notice that the radial velocity $v(R)$ as a function of the radial distance R starts from zero at the center, increases to a maximum at a certain distance, and then decreases again moving further out. The situation is shown in Fig. 2, where the velocity is units $v^* = \sqrt{GM/R_0^2}$, the distance is units of the initial radius $R_0 = 100 \text{ kpc}$, and the maximum occurs at $R/R_0 \simeq 0.4$ (for this particular model).

This reminds the core collapse in a massive star (cf. Bethe 1990), which obeys the following scheme

- homologous collapse in all regions internal to a certain value of the radius (R^*): $v(R) \propto R$;
- free-fall outside: $v(R) \propto R^{-\frac{1}{2}}$;

where R^* is the radius at which the maximum velocity occurs.

How does the above simple scheme compare with the results of numerical calculations? To this aim, in Fig. 2 we plot the best fit of the data from the numerical model for the two branches of the velocity curve and compare them with the above relationships. In this particular example, the slope along the ascending branch ($R/R_0 < 0.4$) is $1.5 \div 2$ instead of 1, whereas that along the descending branch ($R/R_0 > 0.4$) is -0.87 instead of -0.5 .

A close inspection of the numerical Tree-SPH models reveals that neither the slopes of the velocity branches nor the radius of the peak velocity are constant in time. Therefore we will consider all of them as free parameters and cast the problem in a general fashion suited to our aims.

Let us express the velocity $v(R)$ as

$$v(R) = c_1 \times R^\alpha \quad \text{for } R \leq R^*$$

$$v(R) = c_2 \times R^{-\beta} \quad \text{for } R > R^*$$

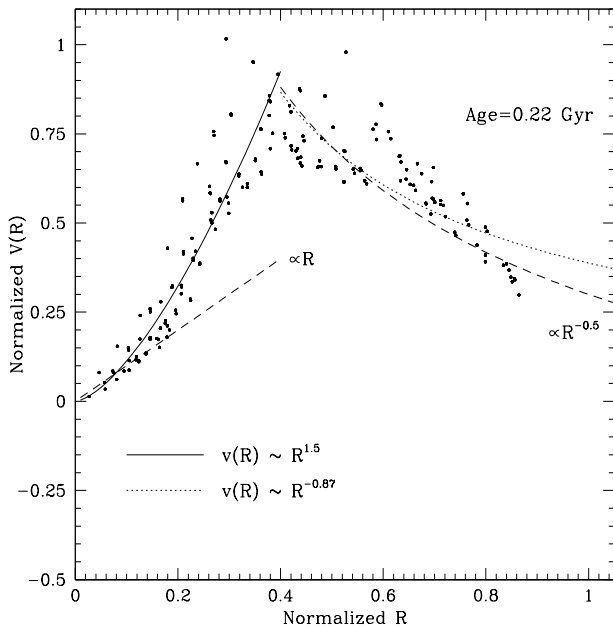


Fig. 2. The radial velocity $v(R/R_0)$ versus radius R/R_0 relationship for a Tree-SPH model of the adiabatic collapse of a galaxy with total mass (baryonic and dark matter) of $10^{12} M_\odot$ from Carraro et al. (1997). The velocity and radius are normalized to v^* and R_0 as described in the text. The full dots are the results of the numerical calculations. The *solid* and *dotted* lines are the best fits of the data: $v(R) \propto R^{1.5}$ for the inner core and $v(R) \propto R^{-0.87}$ for the external regions. The *dashed lines* are the same but for the strict homologous collapse and free-fall description

(where c_1 , c_2 , α and β are suitable constants), and the time scale of accretion as

$$\tau(R) \propto \frac{R}{v(R)}$$

Many preliminary models calculated with the above recipe, of which no detail is given here for the sake of brevity, indicate that $\alpha = 2$ and $\beta = 0.5$ are good choices. The value $\alpha = 2$ is indeed taken from the Tree-SPH models whereas $\beta = 0.5$ follows from the core collapse analogy. The determination of the constants c_1 and c_2 is not required as long as we seek for scaling relationships. Therefore the time scale of gas accretion can be written as proportional to some arbitrary time scale, modulated by a correction term arising from the scaling law for the radial velocity. For the time scale base-line we can take the free-fall time scale t_{ff} referred to the whole system. Passing to our notation for radial distances we get

$$\tau(r_{j/2}) = t_{ff} \times \frac{r^*}{r_{j/2}} \quad \text{if } r_{j/2} \leq r^* \quad (23)$$

$$\tau(r_{j/2}) = t_{ff} \times \left(\frac{r_{j/2}}{r^*}\right)^{3/2} \quad \text{if } r_{j/2} > r^* \quad (24)$$

For the free-fall time scale t_{ff} we make use of the relation by Arimoto & Yoshii (1987)

$$t_{ff} = 0.0697 \times M_{L,T,12}^{0.325} \quad \text{Gyr.} \quad (25)$$

Finally, we take $r^* = \frac{1}{2}$ for the sake of simplicity. Other choices are obviously possible. They would not change the main qualitative results of this study.

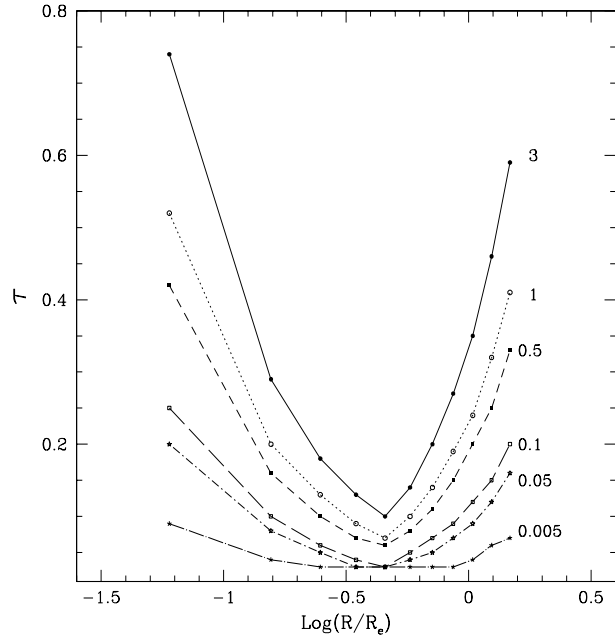


Fig. 3. The accretion time scale $\tau(r)$ as a function of the galacto-centric distance for the models with different asymptotic mass $M_{L,T,12}$ as indicated

In order to derive the specific efficiency of star formation $\nu(r_{j/2})$ we utilize the simple scale relations developed by Arimoto & Yoshii (1987) however adapted to the density formalism. At the typical galactic densities (10^{-22} - $10^{-24} \text{ g cm}^{-3}$) and considering hydrogen as the dominant coolant (Silk 1977) the critical Jeans length is much smaller than the galactic radius, therefore the galaxy gas can be considered as made of many cloudlets whose radius is as large as the Jeans scale. If these clouds collapse nearly isothermal without suffering from mutual collisions, they will proceed through subsequent fragmentation processes till opaque small subunits (stars) will eventually be formed. In such a case the stars are formed on the free-fall time scale. In contrast, if mutual collisions occur, they will be supersonic giving origin to layers of highly cooled and compressed material; the Jeans scale will then fall below the thickness of the compressed layer and fragmentation occurs on the free-fall time scale of the high density layers; and finally the whole star forming process is driven by the

Table 1. The radial dependence of $\tau(r_{j/2})$ and $\nu(r_{j/2})$ in galactic models of different asymptotic luminous mass as indicated. The collapse time scales $\tau(r_{j/2})$ are in Gyr. The galactic baryonic masses are in units of $10^{12}M_{\odot}$.

Region	$3M_{L,T,12}$	$1M_{L,T,12}$		$0.5M_{L,T,12}$		$0.1M_{L,T,12}$		$0.05M_{L,T,12}$		$0.005M_{L,T,12}$			
		τ	ν	τ	ν	τ	ν	τ	ν	τ	ν		
0	$r_{1/2}$	0.74	7.1	0.52	9.0	0.42	10.4	0.25	14.7	0.20	17.0	0.09	27.7
1	$r_{3/2}$	0.29	50.0	0.20	60.6	0.16	68.3	0.10	90.6	0.08	102.4	0.04	154.1
2	$r_{5/2}$	0.18	111.6	0.13	132.8	0.10	148.3	0.06	191.9	0.05	214.6	0.03	312.3
3	$r_{7/2}$	0.13	198.6	0.09	233.3	0.07	258.5	0.04	328.7	0.03	364.9	0.03	518.5
4	$r_{9/2}$	0.10	325.5	0.07	378.3	0.06	416.3	0.03	521.4	0.03	575.2	0.03	800.7
5	$r_{11/2}$	0.14	501.4	0.10	577.3	0.08	631.6	0.05	780.8	0.04	856.5	0.03	1171.1
6	$r_{13/2}$	0.20	753.8	0.14	860.3	0.11	936.1	0.07	1142.8	0.05	1247.1	0.03	1676.6
7	$r_{15/2}$	0.27	1116.0	0.19	1262.8	0.15	1366.9	0.09	1648.8	0.07	1790.2	0.03	2367.9
8	$r_{17/2}$	0.35	1632.9	0.24	1832.5	0.20	1973.4	0.12	2352.9	0.09	2542.1	0.04	3309.8
9	$r_{19/2}$	0.46	2383.7	0.32	2653.1	0.25	2842.6	0.15	3350.2	0.12	3602.2	0.06	4616.9
10	$r_{21/2}$	0.59	3493.2	0.41	3855.9	0.33	4110.1	0.20	4787.8	0.16	5122.6	0.07	6462.5

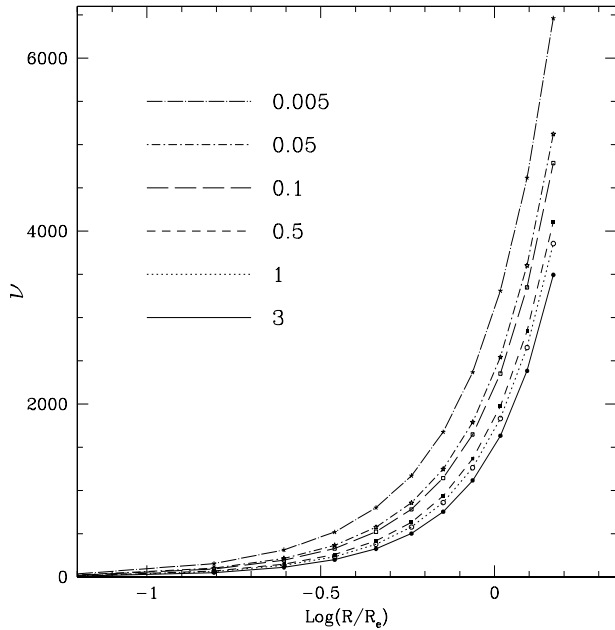


Fig. 4. The specific efficiency of star formation $\nu(r)$ as a function of the galacto-centric distance for the models with different asymptotic mass $M_{L,T,12}$ as indicated. See the text for more details

collision time scale. On the basis of these considerations, we take the ratio

$$\sqrt{\frac{1}{t_{ff} \times t_{col}}}. \quad (26)$$

as a measure of the net efficiency of star formation.

Let us express $\nu(r)$ as the product of a suitable yet arbitrary specific efficiency ν^* referred to the whole galaxy times a dimensionless quantity $F(r)$ describing as the above ratio varies with the galacto-centric distance. An obvious expression for $F(r)$ is the ratio (26) itself normalized to its central value.

According to Arimoto & Yoshii (1987) the mean collision time scale referred to the whole galaxy can be written as

$$t_{col} = 0.0072 \times M_{L,T,12}^{0.1} \quad \text{Gyr} \quad (27)$$

With the aid of this and the relation for the free-fall time scale above we can calculate ν^*

$$\nu^* = \left[\sqrt{\frac{1}{t_{ff} \times t_{col}}} \right]_{gal}. \quad (28)$$

Extending by analogy the above definition of free-fall and collision time scales to each individual region, we get

$$F(r) = \left(\frac{r_{1/2}}{r_{j/2}} \right)^{3\gamma} \times \left[\frac{\bar{\rho}_g(r_{1/2}, T_G)}{\bar{\rho}_g(r_{j/2}, T_G)} \right]^\gamma \quad (29)$$

with obvious meaning of the symbols.

In principle, the exponent γ could be derived from the mass dependence of t_{ff} and t_{col} , i.e. $\gamma \simeq 0.2$. However, a preliminary analysis of the problem has indicated that $F(r)$ must vary with the radial distance more strongly than this simple expectation. The following relation for γ has been found to give acceptable results as far as gradients in star formation, metallicity, colours, etc.. are concerned

$$\gamma = 0.98 \times (M_{L,12})^{0.02} \quad (30)$$

Finally, the total expression for $\nu(r)$ is

$$\nu(r) = \left[\frac{1}{t_{ff} \times t_{col}} \right]_{gal}^{0.5} \times \left(\frac{r_{1/2}}{r_{j/2}} \right)^{3\gamma} \times \left[\frac{\bar{\rho}_g(r_{1/2}, T_G)}{\bar{\rho}_g(r_{j/2}, T_G)} \right]^\gamma \text{ Gyr}^{-1} \quad (31)$$

Table 1 contains the values of $\tau(r_{j/2})$ and $\nu(r_{j/2})$ as a function of the galacto-centric distance for all the galactic models under consideration, whereas Figs. 3 and 4 show the same in graphical form. As expected, in a galaxy the specific efficiency of star formation increases going outward. Likewise, at given relative distance from the galactic center, passing from a low to a high mass galaxy.

6. The mass-radius relationships

To proceed further we need to adopt suitable relationships between the $R_{L,e}$ and $M_{L,T}$, so that once the total baryonic mass is assigned, the effective radius is derived, and all the other quantities are properly re-scaled.

For the purposes of this study and limited to the case of $H_0 = 50 \text{ km sec}^{-1} \text{ Mpc}^{-1}$, we derive from the data of Carollo et al. (1993), Goudfrooij et al. (1994) the following relation

$$R_{L,e} = 17.13 \times M_{L,T,12}^{0.557} \quad (32)$$

where $R_{L,e}$ is in kpc.

For the same objects and using the diameters from the RC3 catalogue we also derived the relation between total radius and mass of the luminous material

$$R_{L,T} = 39.10 \times M_{L,T,12}^{0.402} \quad (33)$$

in the same units as above.

The relations above are displayed in Fig. 5 and compared with the mass radius relation by Saito (1979a,b). Finally, Table 2 lists $R_{L,e}$ and $R_{L,T}$ as assigned to each model galaxy.

7. Mass zoning of the models

The mass zoning of our models is chosen in such a way that within each shell about 5% of the luminous mass $M_{L,T,12}$ is contained. From the tabulations of Young (1976) we derive the corresponding fractionary radius $R/R_{L,e}$, and from the mass-radius relationships above we fix the effective radius $R_{L,e}$, and the real inner and outer radii of each shell. The results are given in Table 3, whereby the meaning of the various symbols is self-explanatory.

Since the observational data for the gradients do not extend beyond $\sim 2R_{L,e}$ (see Carollo & Danziger 1994a,b), our models are limited to the first eleven regions of the galaxy, i.e. to fractionary radii $R/R_{L,e} = 1.6$ or equivalently the inner sphere containing 55% of the total luminous mass $M_{L,T,12}$. Care must be paid when comparing integrated observational quantities, such as magnitudes and colours (see below), with model results.

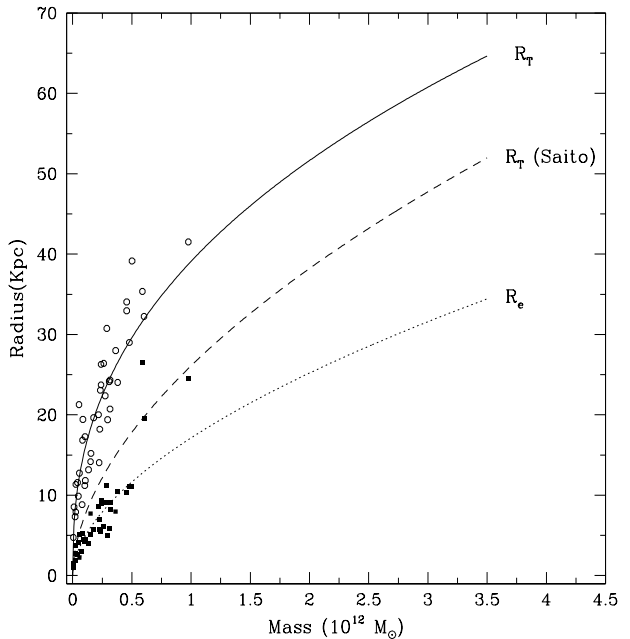


Fig. 5. The mass-radius relationships derived from the observational data by Carollo et al. (1993): the *open circles* are the total radius, whereas *filled squares* are the effective radius. The *dotted*, and *dashed* lines show the relationships $M_L(R_T)$ and $M_L(R_e)$. Finally, the *long-dashed* line displays the relation by Saito (1979a,b) for purposes of comparison

Table 2. Effective and total radii (in kpc) assigned to model galaxies of different $M_{L,T,12}$.

$M_{L,T,12}$	$R_{L,T}$	$R_{L,e}$
3	60.78	31.60
1	39.10	17.13
0.5	29.60	11.64
0.1	15.51	4.75
0.05	11.74	3.23
0.005	4.66	0.90

8. Galactic Winds

Baum (1959) first discovered that elliptical galaxies obey a mean color-magnitude relation (CMR): colours get redder at increasing luminosity. Long ago Larson (1974) postulated that the present-day CMR could be the result of *galactic winds* powered by supernova explosions thus initiating a long series of chemo-spectro-photometric models of elliptical galaxies standing on this idea (Saito 1979a,b;

Table 3. Percentage of luminous mass contained in the sphere of fractionary radius $r'/R_{L,e}$, and actual radius r' (in kpc) for model galaxies with different $M_{L,T,12}$ as indicated.

$M_{L,T,12}$		3	1	0.5	0.01	0.05	0.005	
$\%M_{L,T,12}$	j	$\frac{R}{R_e}$	R	R	R	R	R	
5	0	0.1106	3.49	1.89	1.29	0.53	0.36	0.10
10	1	0.2005	6.33	3.43	2.33	0.95	0.65	0.18
15	2	0.2954	9.33	5.06	0.69	1.40	0.95	0.26
20	3	0.3983	12.58	6.82	4.64	1.89	1.29	0.36
25	4	0.5127	16.20	8.78	5.97	2.44	1.66	0.46
30	5	0.6405	20.24	11.05	7.46	3.04	2.07	0.57
35	6	0.7833	24.75	13.42	9.12	3.72	2.53	0.70
40	7	0.9464	29.90	16.21	11.02	4.50	3.06	0.85
45	8	1.1330	35.80	19.41	13.19	5.38	3.66	1.01
50	9	1.3490	42.62	23.11	15.71	6.41	4.36	1.21
55	10	1.6020	50.62	27.45	18.65	7.61	5.17	1.43
60	11	1.9030	60.13	32.60	22.16	9.04	6.14	1.70
65	12	2.2690	71.69	38.87	26.42	10.78	7.33	2.03
70	13	2.7240	86.07	46.67	31.72	12.94	8.79	2.44
75	14	3.3060	104.45	56.64	38.49	15.70	10.67	2.96
80	15	4.0870	129.13	70.02	47.59	19.41	13.19	3.66
85	16	4.9580	156.65	84.94	57.73	23.55	16.01	4.44

Matteucci & Tornambé 1987; Arimoto & Yoshii 1987; Angeletti & Giannone 1990; Mihara & Tahara 1994; Matteucci 1994; Bressan et al. 1994; Tantalo et al. 1996; Gibson 1994, 1996, 1997; Gibson & Matteucci 1997, and references therein). In brief, gas is let escape from the galaxy and star formation is supposed to halt when the total thermal energy of the gas equates its gravitational binding energy.

The same scheme is adopted here, however with minor modifications due to the overall properties of the models and the present formalism.

The thermal energy of the gas is sum of three contributions, namely type I and II supernovae and stellar winds from massive stars:

$$E_{th}(r_{j/2}, t) = E_{th}(r_{j/2}, t)_{SNI} + E_{th}(r_{j/2}, t)_{SNII} + E_{th}(r_{j/2}, t)_W \quad (34)$$

where:

$$E_{th}(r_{j/2}, t)_{SNI} = \int_0^t \epsilon_{SN}(t-t') R_{SNI}(r_{j/2}, t') \Delta M_L(r_{j/2}, T_G) dt' \quad (35)$$

$$E_{th}(r_{j/2}, t)_{SNII} = \int_0^t \epsilon_{SN}(t-t') R_{SNII}(r_{j/2}, t') \Delta M_L(r_{j/2}, T_G) dt' \quad (36)$$

and

$$E_{th}(r_{j/2}, t)_W =$$

$$\int_0^t \epsilon_W(t-t') R_W(r_{j/2}, t') \Delta M_L(r_{j/2}, T_G) dt' \quad (37)$$

with obvious meaning of the symbols. As the production rates $R_{SNI}(r_{j/2}, t)$, $R_{SNII}(r_{j/2}, t)$ and $R_W(r_{j/2}, t)$ are the same as in the set of equations governing the chemical evolution, which are expressed as a function of the dimensionless variables $G_{g,i}(r_{j/2}, t)$, the normalization factor $\Delta M_L(r_{j/2})$ in the equations above is required to calculate the energy in physical units.

The time t' is either the SN explosion time or the time of ejection of the stellar winds as appropriate. The functions $\epsilon_{SN}(t)$ and $\epsilon_W(t)$ are cooling laws governing the energy content of supernova remnants and stellar winds, respectively.

Finally, shell by shell, star formation and chemical enrichment are halted, and the remaining gas content is supposed to be expelled out of the galaxy (winds) when the condition

$$E_{th}(r_{j/2}, t) \geq \Omega_g(r_{j/2}, t) \quad (38)$$

is verified.

8.1. Supernovae and Wind Rates

Although the production rates have already been used to define the set of equations governing the evolution of the $G_{g,i}(r_{j/2}, t)$, they are also re-written here for the sake of clarity.

$$R_{SNI}(r_{j/2}, t) =$$

$$\Lambda \int_{M_{Bm}}^{M_{BM}} \phi(M_B) \int_{\mu_{min}}^{0.5} f(\mu) \Psi(r_{j/2}, t - t_{M_2}) d\mu dM_B \quad (39)$$

$$R_{SNII}(r_{j/2}, t) = (1 - \Lambda) \int_6^{16} \phi(M) \Psi(r_{j/2}, t - t_M) dM \\ + \int_{16}^{M_{max}} \phi(M) \Psi(r_{j/2}, t - t_M) dM \quad (40)$$

and finally

$$R_W(r_{j/2}, t) = \int_{30}^{M_{max}} \phi(M) \Psi(r_{j/2}, t - t_M) dM \quad (41)$$

The meaning of all the symbols is the same as above.

8.2. Evolution of supernova remnants

In this section we briefly summarize the prescription we have adopted for the cooling law of supernova remnants and the final energy deposit. The formulation strictly follows Gibson (1994, 1996 and references therein).

The evolution of a SNR can be characterized by three dynamical phases: (i) free expansion (until the mass of the swept up interstellar material reaches that of the SN ejecta); (ii) adiabatic expansion until the radiative cooling time of newly shocked gas equals the expansion time of the remnant; (iii) formation of a cold dense shell (behind the front) which begins when some sections of the shocked gas have radiate most of their thermal energy, begin further compressed by the pressure of the remainder of the shocked material.)

In the earliest phase the evolution of the supernova remnant is governed by the Sedov-Taylor solution for a self-similar adiabatic shock (Ostriker & McKee 1988)

$$R_s(t) = 1.15 \left(\frac{E_0}{\bar{\rho}_g(t)} \right)^{1/5} t^{2/5} \quad (42)$$

where $R_s(t)$ is the radius of the outer edge of the SNR shock front, E_0 is the initial blast energy in units of 10^{50} ergs (or equivalently $E_0 = 10 \times \epsilon_0$, where ϵ_0 is the same energy in units of 10^{51} erg), and $\bar{\rho}_g(t)$ is the gas mass density of the environment.

Radiative cooling of the shocked material leads to the formation of a thin, dense shell at time t_{sf}

$$t_{sf} = 3.61 \times 10^4 \epsilon_0^{3/14} n_0^{-4/7} \left(\frac{Z}{Z_\odot} \right)^{-5/14} \text{ yr} \quad (43)$$

where n_0 is the hydrogen number density, Z is the metallicity of the interstellar medium, and $Z_\odot = 0.016$. The blast wave decelerates until the radiative energy lost in the shell's material starts to dominate. At this point, the shell enters the so-called ‘‘pressure-driven snowplow’’ (PDS) phase at the time $t_{pds} \approx 0.37 t_{sf}$.

The evolution of the thermal energy in the hot, dilute interior of the supernova remnants can be taken equal to

$$\epsilon_{SN}(t_{SN}) = 0.717 E_0 \quad \text{erg} \quad (44)$$

when $t_{SN} \leq t_{pds}$ i.e. during the adiabatic phase. Note that $t_{SN} = t - t'$ is the time elapsed since the supernova explosion. During the early PDS-phase, when $t_{pds} \leq t_{SN} \leq 1.17 t_{sf}$, the thermal energy evolution is given by

$$\epsilon_{SN}(t_{SN}) = 0.29 E_0 \left[1 - \left(\frac{0.86 t_{SN}}{t_{sf}} \right)^{14/5} \right] + \\ 0.43 E_0 \left[\left(\frac{R_s}{R_{sf}} \right)^{10} + 1 \right]^{-1/5} \left[\left(\frac{t_{SN}}{t_{sf}} \right)^4 + 1 \right]^{-1/9} \text{ erg} \quad (45)$$

and the radius changes according to

$$R_s(t_{SN}) = R_{pds} \left(\frac{4 t_{SN}}{3 t_{pds}} - \frac{1}{3} \right)^{3/10} \text{ pc} \quad (46)$$

where R_{pds} is the radius at the beginning of the PDS-stage

$$R_{pds} = 14. \epsilon_0^{2/7} n_0^{3/7} \left(\frac{Z}{Z_\odot} \right)^{-1/7} \text{ pc} \quad (47)$$

The interior continues to lose energy by pushing the shell through the interstellar medium and by radiative cooling. At time t_{merge}

$$t_{merge} = 21.1 t_{sf} \epsilon_0^{5/49} n_0^{10/49} \left(\frac{Z}{Z_\odot} \right)^{15/49} \text{ yr} \quad (48)$$

the remnants merge with the interstellar medium and lose their identity as separate entities.

The thermal energy during the time interval $1.17 t_{sf} \leq t_{SN} \leq t_{merge}$ is given by the second term of Eq. 45. The evolution after the t_{merge} time is described again by the second term of Eq. 45, but the radius R_s is given by

$$R_s = R_{merge} = 3.7 R_{pds} \epsilon_0^{3/98} n_0^{3/49} \left(\frac{Z}{Z_\odot} \right)^{9/98} \text{ pc} \quad (49)$$

Finally, when $t_{SN} \geq t_{cool}$ in which

$$t_{cool} = 203 t_{sf} \left(\frac{Z}{Z_\odot} \right)^{-9/14} \text{ yr} \quad (50)$$

the thermal energy is given by the second term of Eq. 45 but with $R_s = R_{merge}$.

The time dependence of the cooling law for interstellar media with different metallicities is shown in Fig. 6 and is compared with the classical one by Cox (1972). It is soon evident that this more elaborated scheme for the cooling of supernova remnants supplies more energy to the interstellar medium than the old one. The adoption of the Cox (1972) cooling law by Bressan et al. (1994) and TCBF96 may also explain why they had to invoke other sources of energy to power galactic winds (see the remark below).

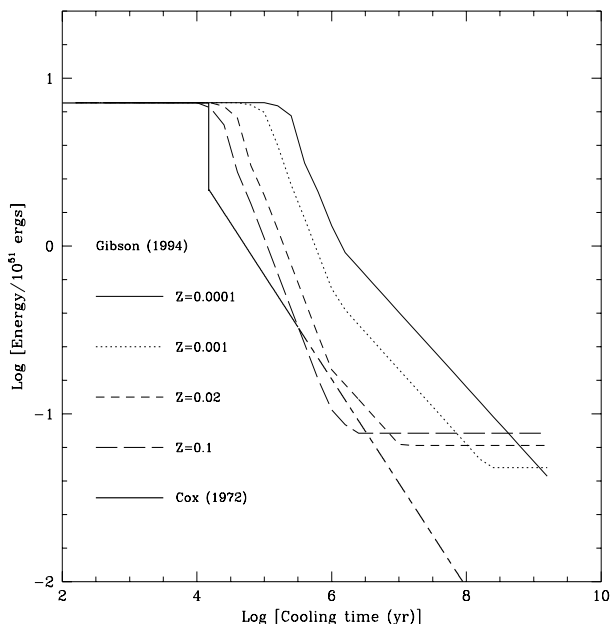


Fig. 6. The cooling law of supernova remnants as a function of the gas metallicity as indicated

8.3. Thermal content of the winds

The thermal content in the winds ejected by massive stars is estimated in the following way. A typical massive star (say in the range $20M_{\odot}$ to $120M_{\odot}$) in the course of evolution ejects about half of its mass in the form of a wind with terminal velocity of about 2000 km sec^{-1} (see Chiosi & Maeder 1986) and therefore injects into the interstellar medium an energy of about

$$\epsilon_{W0} = \eta \frac{1}{2} \left(\frac{M}{2} \right) \left(\frac{Z}{Z_*} \right)^{0.75} V^2 \quad \text{erg} \quad (51)$$

where the term $(Z/Z_*)^{0.75}$ takes into account that both mass loss rates and terminal velocities depend on metallicity (Kudritzki et al. 1987, Theis et al. 1992), and η is the efficiency parameter of kinetic energy thermalization. The reference metallicity is $Z_* = 0.02$.

The evolution of adiabatic interstellar bubbles as a result of stellar winds interacting with the surrounding medium, including radiative losses, confines the efficiency parameter in the range $0.2 \leq \eta \leq 0.4$ (Weaver et al. 1977; Koo & McKee 1992; Gibson 1994). We have assumed $\eta = 0.3$.

By analogy with the formalism used to calculate the residual thermal energy of supernova remnants as a function of time, we write

$$\epsilon_W(t_W) = \epsilon_{W0} \quad \text{if } 0 \leq t_W \leq t_{cw}$$

or

$$\epsilon_W(t_W) = \epsilon_{W0} \left(\frac{t_W}{t_{cw}} \right)^{-0.62} \quad \text{if } t_W \geq t_{cw} \quad (52)$$

where $t_W = t - t'$ is the time elapsed since the birth of a massive star, t_{cw} is the cooling time scale. When stellar winds were first introduced by Bressan et al. (1994) in the calculation of the total thermal budget, the following parameters were adopted: $\eta = 1$ and $t_{cw} = 15 \times 10^6$ yr. This latter in particular was conceived as the typical lifetime of a newly born group of massive stars (either in clusters or associations) able to lose mass at a significant rate (indeed $t_{cw} = 15 \times 10^6$ yr is the typical lifetime of a $10M_{\odot}$ object). Bressan's et al. (1994) approach did not pass Gibson's (1994) scrutiny who correctly pointed out that only a fraction of the kinetic energy goes thermalized ($\eta = 0.3$) and that t_{cw} should be set equal to a star's lifetime and therefore should vary with the star mass. Of course the adoption of that particular set of parameters by Bressan et al. (1994) and later by TCBF96 led to *early* galactic winds as compared to the significantly *later* winds found by Gibson (1994). In a subsequent paper along the same vein, Gibson (1996) suggested that part of the reason why Bressan et al. (1994) looked for additional sources of energy (the stellar winds) in addition to supernovae in order to avoid saturation in the metallicity and failure in matching the CMR resided in a mismatch of the stellar yields of metals in their chemical code. Since our goal is not to argue against Gibson's criticism, nor to embark in a *vis-a-vis* comparison of the codes, in the mean time the chemical code has been fully revised and up-graded with respect to the old one, and the arguments given by Gibson (1994, 1996) are convincing, we definitely follow his favourite prescription: $\eta = 0.3$ and t_{cw} shorter than mean lifetime of the most massive stars contributing to stellar wind energies. In the models below $t_{cw} = 10^6$ yr, see Fig.2 in Gibson (1994).

9. General properties of the models

The main properties of each model at the stage of galactic wind are summarized in Table 4 (not given here but available from the A&A electronic data-base) as a function of the radial distance from the center. Column (1) is the asymptotic mass $M_{L,T,12}$, column (2) is the efficiency of star formation $\nu(r_{j/2})$; column (3) is the IMF parameter ζ ; column (4) is the time scale of mass accretion $\tau(r_{j/2})$ in Gyr. Column (5) shows the value reached by $M_{L,t}$ at the onset of galactic wind. This is the real luminous mass of the galaxy built up by the infall process, all the remaining gas (both already accreted and still on the way) being swept away by galactic winds. Columns (6) through (8) are the age in Gyr at which the galactic wind occurs, and the corresponding dimensionless mass of gas $G(r, t)$ and living stars $S(r, t)$, respectively. According to their definition, in order to obtain the real mass in gas

and stars (in solar units) one has to multiply them by the normalization mass of each shell, i.e. $\Delta M_L(r_{j/2}, T_G)$. Likewise, to get from $G(r, t)$ and $S(r, t)$ the corresponding densities, the multiplicative factor is $\bar{\rho}_L(r_{j/2}, T_G)$. Columns (9) and (10) are the maximum and mean metallicity, $Z(r_{j/2}, t)$ and $\langle Z(r_{j/2}, t) \rangle$ reached by each shell at the onset of the galactic wind. Column (11) contains the rate of star formation $\Psi(r_{j/2}, t)$ in units of M_\odot/yr . Columns (12) through (16) are the gravitational binding energy of the gas $\Omega_g(r_{j/2}, t)$, the total thermal energy of this $E_g(r_{j/2}, t)$, and the separated contributions by Type I, Type II supernovae, and stellar winds, respectively. All energy are in units of 10^{50} ergs. Finally, column (17) is the mid shell fractionary radius $r_{j/2}$.

9.1. Internal consistency of the models

The scheme we have elaborated in the previous sections is self-contained in absence of galactic winds, because in such case at the galaxy age T_G all shells have reached their asymptotic mass and the effective radius $R_{L,e}$ (the basic scale factor associating the asymptotic density of the Young profile to each radius) is consistent with $M_{L,T}(T_G)$.

At the stage of galactic wind we suppose that all the gas contained in the shell, the one still in the infall process and the one expelled by supernova explosions and stellar winds are ejected into the intergalactic medium and never re-used to form stars. This implies that at the stage of galactic wind the real mass of each shell (the fraction of gas turned into long-lived stars up to this stage), is smaller than the corresponding asymptotic mass $\Delta M_L(r_{j/2}, T_G)$. Indeed in each shell the luminous mass has grown up to the value $\Delta M_L(r_{j/2}, t_{gw})$, where t_{gw} is the local value of the age at the onset of the galactic wind. Therefore

$$\sum_{j=0}^{J-1} \Delta M_L(r_{j/2}, t_{gw}) < M_{L,T}(T_G) \quad (53)$$

Recalling that our calculations refer to the innermost part of the galaxy (the one containing 55% of the mass $M_{L,T}(T_G)$), the relation (53) should be replaced by

$$\sum_{j=0}^{10} \Delta M_L(r_{j/2}, t_{gw}) < 0.55 \times M_{L,T}(T_G) \quad (54)$$

Looking at the case of the $3M_{L,T,12}$ galaxy, the sphere we have been following in detail has total asymptotic mass of $1.65 \times 10^{12} M_\odot$, each shell containing about $0.15 \times 10^{12} M_\odot$ (cf. Column (5) of Table 4). In contrast, the total mass reached in the same sphere at the onset of the galactic wind amounts only to $0.66 \times 10^{12} M_\odot$, i.e. some 40% of the expected mass. Even more important, while the innermost shells were able to convert in stars about 0.8 of their asymptotic mass, this is not the case of the outermost shells in which only about 2% of the potential mass has been turned into stars, all the rest being dispersed by a very early wind. Considering that owing to the very low densities in regions above our last shell (approximately $1.5R_{L,e}$) the galactic winds would occur even

earlier than in the last computed shell, this means that starting with $3M_{L,T,12}$ of gas eligible to star formation only 22% of it has been actually turned into long-lived stars visible today. The situation gets slightly better at decreasing $M_{L,T}(T_G)$ because of the much shorter mean infall time scale (cf. Tables 5 and 1).

Furthermore, if we look at the radial profile of $\bar{\rho}_L(r_{j/2}, t_{gw})$ and compare it with $\bar{\rho}_L(r_{j/2}, T_G)$, the former is steeper than the latter, over the shells external $R_{L,e}$ in particular. However, if we limit the comparison to the shells inside $R_{L,e}$ (up to $j = 8$ in our notation), the difference is remarkably smaller. This implies that the region inside $R_{L,e}$ does not depart too much from the basic hypothesis. Finally, the effective radius $R_{L,e}$ used to interpolate in the Young (1976) density profile and to assign $\bar{\rho}_L(r_{j/2}, T_G)$ referred to the asymptotic mass $M_{L,T}(T_G)$. Since the actual present-day mass of the galaxy is smaller than this, we expect the actual effective radius to be smaller than the originally adopted value. With the aid of relation (32) above, the $3M_{L,T,12}$ galaxy has $R_{L,e} \simeq 31.9$ Kpc, whereas the $0.66M_{L,T,12}$ daughter should have $R_{L,e} \simeq 13.7$ kpc (a factor 2.3 smaller). This means that the ratio of the mean density (inside $R_{L,e}$) of the parent to daughter galaxy is about 0.5. It is as if we calculated our models underestimating their real density by a factor of about two. Considering that even within the effective radius passing from the center to the periphery the density of luminous mass drops by orders of magnitude, cf. Young (1976), and all other uncertainties affecting our models, we can perhaps tolerate the above discrepancy. The results we are going to present perhaps constitute the best justification of these models, which do not dare to replace more sophisticated, physically grounded formulations in literature, but simply aim at providing a simple tool to investigate the chemospectro-photometric properties and their spatial gradients of spherical systems roughly simulating elliptical galaxies.

Table 5 summarizes the data relative to the above discussion for all the model galaxies under examination. It lists the asymptotic total mass $M_{L,T}(T_G)$ (column 1), the corresponding effective radius $R_{L,e}(T_G)$ (column 2), the asymptotic mass $M_L(1.5R_{L,e}, T_G)$ within $1.5R_{L,e}$ (the studied model, column 3), the actual mass $M_{L,T}(t_{gw})$ of the galaxy within $1.5R_{L,e}$ at the age t_{gw} (column 4), the actual mass $M_{L,T}(R_{L,e}, t_{gw})$ of the galaxy within $R_{L,e}$ at the age t_{gw} (column 5), and the real effective radius $R_{L,e}(t_{gw})$ (column 6).

9.2. Gas content, metallicity, SFR, and $N(Z)$

The fractionary gas content $G(r, t)$ and metallicity $Z(r, t)$ for the central core of the models (up the fractionary radius $r_{1/2}$) are shown as function of time in panels (a) and (b), respectively, of Fig. 7. In all the models, the fractionary gas density $G_g(r_{1/2}, t)$ starts small, increases up to a maximum and then decreases exponentially to zero as a result of the combined effect of gas accretion by infall

Table 5. Fractionary masses of gas and stars components in units of $10^{12}M_{\odot}$ for the models presented in this work.

$M_{L,T}(T_G)$	$R_{L,e}(T_G)$	$M_L(1.5R_{L,e}, T_G)$	$M_{L,T}(1.5R_{L,e}, t_{gw})$	$M_L(R_{L,e}, t_{gw})$	$R_{L,e}(t_{gw})$
3	31.6	1.65000	0.65700	0.65600	13.55
1	17.1	0.55000	0.21800	0.21500	7.33
0.5	11.7	0.27500	0.10900	0.10700	4.98
0.1	4.7	0.05500	0.02200	0.02100	2.04
0.05	3.2	0.02750	0.01090	0.01070	1.38
0.005	0.9	0.00275	0.00102	0.00097	0.37

and gas consumption by star formation, but owing to the different value of τ in the core from model to model, the peak occurs later at increasing galaxy mass $M_{L,T}(T_G)$.

As far as the metallicity is concerned, this increases more slowly at increasing galaxy mass up to the maximum value reached in coincidence of the galactic wind. As expected the maximum metallicity increases with the galaxy mass, because in this type of model galactic winds occur later at increasing galaxy mass (cf. the entries of Table 4 and Fig. 10 below).

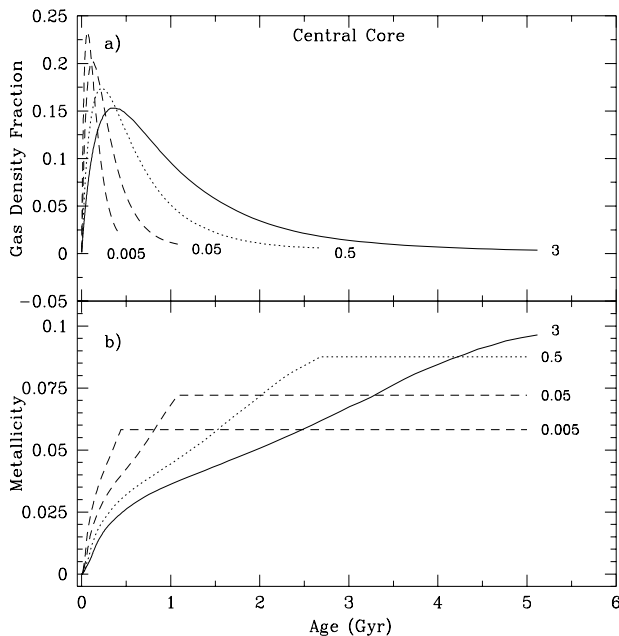
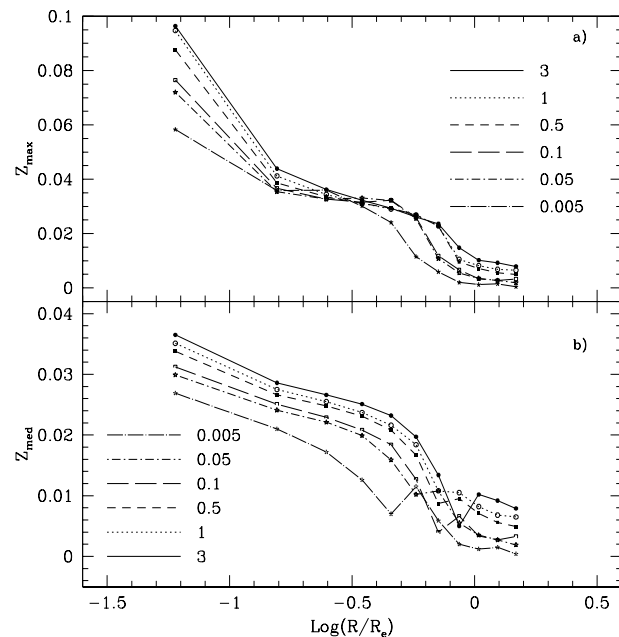

Fig. 7. The gas fraction $G(r,t)$ (top panel) and metallicity $Z(r,t)$ (bottom panel) as a function of the age in *Gyr* for the central core of the galaxy models with different asymptotic mass $M_{L,T,12}$ as indicated

Fig. 8 shows the maximum (Z_{max} , top panel) and mean (Z_{mean} , bottom panel) metallicity as a function of the radial distance from the center (normalized to the

effective radius of each galaxy) for all the models as in Figs. 3 and 4. The mean gradient in the maximum metallicity, $dZ_{max}/d\log(r)$, within $1.5R_{L,e}$ ranges from -0.064 to -0.042 going from massive to dwarf galaxies, whereas the mean gradient in mean metallicity, $dZ_{mean}/d\log(r)$, over the same radial distance and galaxy mass interval goes from -0.021 to -0.019 .


Fig. 8. The gradients in maximum (top panel) and mean metallicity (bottom panel) for the model galaxies with different $M_{L,T,12}$ as indicated

The top panel of Fig. 9 shows the rate of star formation (in units of M_{\odot}/yr) as a function of time (in *Gyr*) for the central core of the models, up to the onset of galactic winds. As expected, the rate of star formation starts very small, grows to a maximum, and then declines exponentially with time, closely mimicking the gas content.

The gas liberated by evolving stars (supernova explosions, stellar winds, and PN) in subsequent epochs is not shown here as all this gas is supposed to be rapidly heated up to the escape velocity.

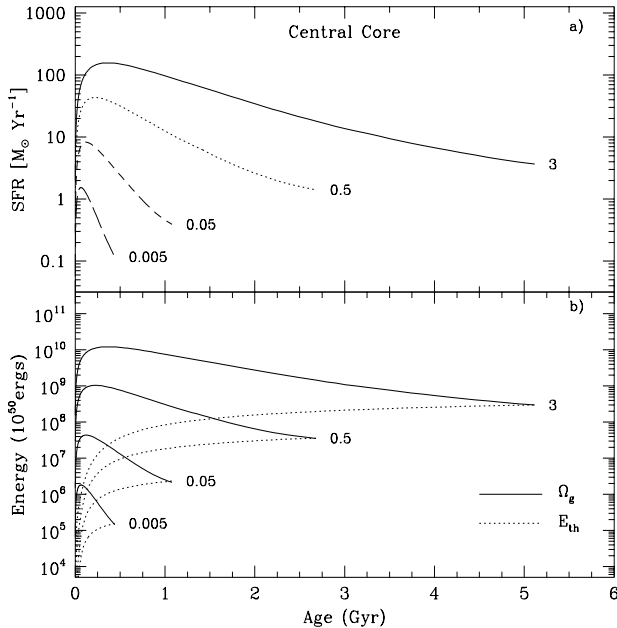


Fig. 9. *Panel a:* the star formation rate as a function of time for the central core of the galaxy models with different asymptotic mass $M_{L,T,12}$ as indicated. *Panel b:* the gravitational binding energy $\Omega_g(r, t)$ and thermal content of the gas $E_{th}(r, t)$, for the same models as above. Energies are in units of 10^{50} ergs

The bottom panel of Fig. 9 displays the comparison between the thermal and the binding energy of the gas, $E_{th}(r, t)$ and $\Omega_g(r, t)$, respectively, as a function of time for the nuclear regions. All the energies are in units of 10^{50} erg. The intersection between $\Omega_g(r, t)$ and $E_{th}(r, t)$ corresponds to the onset of the galactic wind for the innermost region. Similar diagrams can be drawn for all the remaining shells. They are not displayed for the sake of brevity.

In this type of model galactic winds occur earlier passing from the center to external regions, or at given relative distance from the center, going from massive to low mass galaxies. This is shown in Fig. 10 which displays the age of the galactic wind t_{gw} as a function of the galacto-centric distance. The stratification in metallicity, and relative percentage of stars in different metallicity bins resulting from the above trend in t_{gw} bears very much on inferring chemical abundances from local or integrated photometric properties of elliptical galaxies. This topic will be addressed below in some detail.

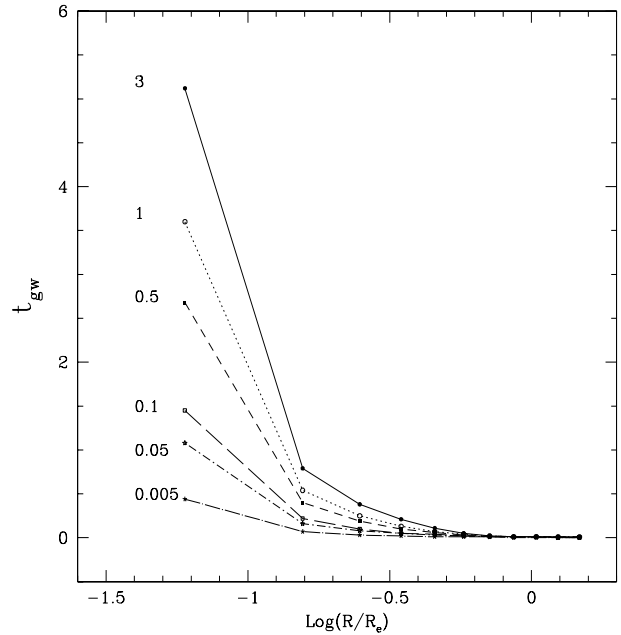


Fig. 10. The age at which galactic winds occur in regions of increasing distance from the galactic centre. The models are the same as in Figs. 3 and 4.

The chemical structure of the models is best understood looking at the fractionary cumulative mass distribution of living stars, $\Sigma_0^Z S_Z/S$, where S is the mass fraction in stars, and S_Z is the mass fraction of stars with metallicity up to Z , and at the so-called *partition function* $N(Z)$, i.e. the relative number of living stars per metallicity bin. Within a galaxy (or region of it) both distributions vary as a function of the age.

The fractionary, cumulative mass distribution as a function of Z is shown in Fig. 11 limited to the central core ($r_{1/2}$, left panel) and the first shell ($r_{3/2}$, right panel) for all the models at the present age ($T_G = 15$ Gyr). The vertical line corresponds to the solar metallicity. In the core and the first shell of the most massive galaxy, about 10% of the stars have metallicity lower than solar. In contrast, the central region of the lowest mass galaxy has about 25% of its stellar content with metallicity lower than solar. This percentage increases to about 36% in the first shell. In all galaxies the percentage of stars with metallicity lower than solar increases as we move further out.

The partition function $N(Z)$ for our model galaxies at the age of 15 Gyr is shown in Fig. 12 limited to the central core (left panel) and first shell (right panel). We learn from this diagram that the mean metallicity of the stars in the core goes from $Z \simeq 0.03$ to $Z \simeq 0.04$; the peak value tends to slightly shift toward higher metallicities at increasing galaxy mass; and there are wings toward both low and high metallicities. The distribution tends to be more concentrated in the first shell, where we notice a

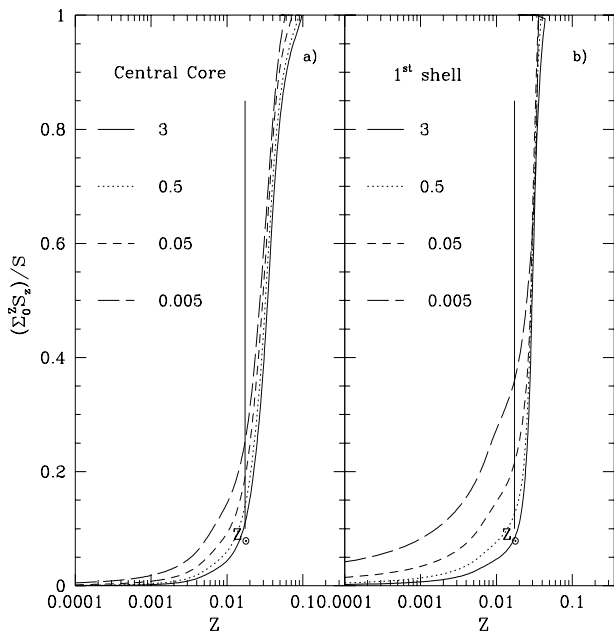


Fig. 11. The cumulative fractionary mass of living stars as a function of the metallicity for the galaxy models with mass 3, 0.5, 0.05, and 0.005 $M_{L,T,12}$. Panels a and b corresponds to the central core and first shell respectively

more abundant population of low metallicity stars and a sharper cut-off at the high metallicity edge caused by the action of galactic winds. Likewise for the remaining shells not displayed here.

10. Photometric Properties

As already mentioned, the guide-line for the layout of the model and the choice of the various parameters was to impose that a number of properties of elliptical galaxies could be simultaneously matched. Specifically: (i) the slope of color-magnitude relation (CMR) (Bower et al. 1992a,b); (ii) the mean value of the broad-band colours; (iii) the UV excess as measured by the colour (1550–V) (Burstein et al. 1988); (iv) the mass to blue luminosity ratio (M/L_B) $_{\odot}$ as a function of the B luminosity (Bender et al. 1992, 1993); (v) the $R^{1/4}$ luminosity profile (Fasano et al. 1996); (vi) the gradient in (B–R) colour measured by Carollo & Danziger (1994a,b) in a sample of elliptical galaxies; (vii) the gradients in line strength indices Mg_2 and $\langle Fe \rangle$ measured by Carollo & Danziger (1994a,b). (viii) and finally, the data of González (1993) for the H_{β} and $[MgFe]$ line strength indices. In this section, we present the comparison of model results with the observational data in relation to the above list of observational *constraints*.

To this aim we need to calculate the integrated colours and line strength indices together with their gradients for

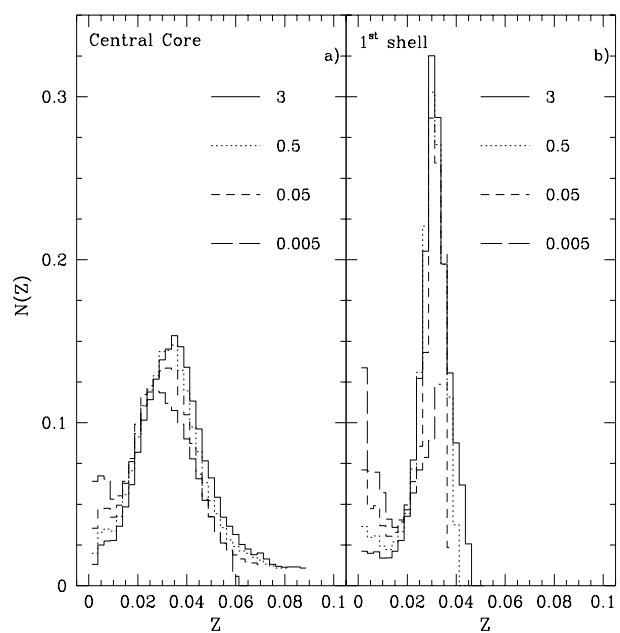


Fig. 12. Relative number of living stars per metallicity bin in the central core *panel a*) and first shell *panel b*) for the models with 3, 0.5 0.05 and 0.005 $M_{L,T,12}$ (the same models as in Fig. 11)

the stellar mix in the model galaxies. The technique in usage here is based on the concept of single stellar populations (SSP) as elemental seeds to derive the integrated stellar energy distribution (ISED) of a galaxy, from which magnitudes, broad-band colours, and line strength indices immediately follow. The SSP's adopted in this paper are those calculated by TCBF96, see also Bressan et al. (1994, 1996), to whom the reader should refer for technical details. First we have calculated the integrated ISED, magnitudes, colours etc. for each zone of our models, and then we have derived the total magnitudes, colours etc. for the whole galaxy.

Table 6 (not given here but available in A&A electronic data-base) lists the integrated magnitudes and broad-band colours of every zone of the model galaxies at three different ages (15, 10, and 5 Gyr). Columns (1) through (5) display: the asymptotic mass of the model (in units of $10^{12}M_{\odot}$), $\nu(r_{j/2})$, $\tau(r_{j/2})$ (in Gyr), the asymptotic mass of each zone (in units of $10^{12}M_{\odot}$) and the age in Gyr, respectively. Columns (6) and (7) give the integrated absolute bolometric (M_{bol}) and visual magnitudes (M_V) of each zone, respectively. Columns (8) through (15) are the integrated colours (U–B), (B–V), (V–R), (V–I), (V–J), (V–H), (V–K), and (1550–V). Finally, Column (16) gives the fractionary radii $r_{j/2}$.

Table 7 shows the same quantities but integrated from the center up the $1.5R_{L,e}$ radius. These are the quantities to be used to compare theory with observations.

Table 7. Integrated magnitude and colours from the center up to the $1.5R_{L,e}$ -sphere of the model galaxies

$M_{L,T,12}$	Age	M_{bol}	M_V	(U-B)	(B-V)	(V-R)	(V-I)	(V-J)	(V-H)	(V-K)	(1550-V)	$r_{j/2}$
(1)	(2)	(3)	(4)	(5)	(6)	(7)	(8)	(9)	(10)	(11)	(12)	(13)
3.0	15	-23.536	-22.700	0.557	0.991	0.596	1.201	2.396	3.117	3.323	3.135	1.48
3.0	10	-23.925	-23.071	0.502	0.962	0.582	1.180	2.432	3.161	3.379	4.762	1.48
3.0	5	-24.697	-23.798	0.300	0.845	0.538	1.112	2.440	3.176	3.412	1.283	1.48
1.0	15	-22.316	-21.512	0.515	0.972	0.588	1.186	2.348	3.064	3.264	3.279	1.48
1.0	10	-22.697	-21.878	0.461	0.946	0.575	1.166	2.379	3.103	3.314	4.237	1.48
1.0	5	-23.357	-22.536	0.368	0.882	0.545	1.118	2.384	3.115	3.338	5.652	1.48
0.5	15	-21.563	-20.786	0.484	0.957	0.581	1.174	2.309	3.021	3.217	3.404	1.48
0.5	10	-21.940	-21.147	0.434	0.936	0.570	1.155	2.340	3.060	3.267	4.257	1.48
0.5	5	-22.581	-21.790	0.348	0.873	0.540	1.107	2.340	3.067	3.284	5.506	1.48
0.1	15	-19.802	-19.101	0.389	0.906	0.560	1.134	2.192	2.888	3.070	3.490	1.48
0.1	10	-20.170	-19.455	0.350	0.898	0.552	1.121	2.223	2.928	3.121	4.561	1.48
0.1	5	-20.784	-20.076	0.281	0.834	0.523	1.072	2.212	2.923	3.125	5.078	1.48
0.05	15	-19.059	-18.392	0.350	0.885	0.551	1.116	2.141	2.828	3.006	3.512	1.48
0.05	10	-19.425	-18.742	0.315	0.881	0.544	1.106	2.173	2.869	3.057	4.769	1.48
0.05	5	-20.034	-19.358	0.254	0.818	0.515	1.058	2.160	2.862	3.058	4.916	1.48
0.005	15	-16.404	-15.813	0.266	0.829	0.527	1.070	2.016	2.679	2.843	3.456	1.48
0.005	10	-16.762	-16.159	0.236	0.837	0.524	1.066	2.047	2.719	2.891	5.151	1.48
0.005	5	-17.359	-16.766	0.189	0.774	0.495	1.017	2.023	2.701	2.881	4.544	1.48

10.1. Color-Magnitude relation

The CMR for the models in Tables 6 and 7 is compared with the data by Bower et al. (1992a,b) for the Virgo and Coma elliptical galaxies. Since the observational data refer to the whole galaxies, the theoretical results of Table 7 must be suitably corrected to take into account the contribution from all the other regions not considered here. To this aim we proceed as follows: the integrated magnitudes (Table 7) refer to the sphere of $1.5 \times R_{L,e}$ in which 55% of the total mass is contained; the models supposedly obey the $R^{1/4}$ law (see also the discussion below); with the aid of items (i) and (ii) we calculate the fraction of light coming from the regions from $1.5 \times R_{L,e}$ to ∞ . To a first approximation the total magnitudes are simply given by

$$M_{\Delta\lambda,T} = M_{\Delta\lambda,(1.5 \times R_e)} - 0.3342 \quad (55)$$

where $\Delta\lambda$ indicates the pass-band and all the other symbols are self-explanatory.

The comparison between theory and observations is shown in Fig. 13. for three values of the age as indicated. The Virgo and Coma galaxies are displayed with different symbols: open and filled circles, respectively. The absolute magnitudes V are calculated assuming the distance modulus to Virgo of $(m - M)_o = 31.54$ (Branch & Tammann 1992) and applying to the Coma galaxies the shift $\delta(m - M)_o = 3.58$ (Bower et al. 1992a,b).

The agreement is remarkably good both as far as the absolute colours and the slope of the CMR are concerned. According to Bower et al. (1992a,b) the thickness of the Virgo-Coma CMR in the (U-V) versus M_V plane implies

that elliptical galaxies in these clusters are old with little age dispersion say $13 \div 15$ Gyr. Although this conclusion is compatible with the data in Fig. 13, our isochrones in the (V-K) versus M_V plane span a small range in colour passing from 5 to 15 Gyr, so that confirmation of an old age from this side is not possible.

10.2. Mass to blue luminosity ratio

To calculate the $(M/L_B)_\odot$ ratios for the model galaxies the following procedure is adopted: first using the data of Tables 4 and 5 we derive the total present-day value of the galactic mass *up to the last calculated shell*, second we utilize the integrated magnitudes of Table 7 *to evaluate the blue luminosity*. The results are presented in Table 8 which lists the age in Gyr (Column 1), the asymptotic mass $M_{L,T,12}$ (Column 2), the current mass of the galaxy in units of $10^{12}M_\odot$ (Column 3), the blue magnitude M_B (Column 4), the blue luminosity L_B in solar units (Column 5), and finally, the mass to blue luminosity ratio $(M/L_B)_\odot$ (Column 6). As long known, on the theoretical side the mass to blue luminosity ratio $(M/L_B)_\odot$ is very sensitive to the IMF, i.e. for a Salpeter-like case to the slope and ζ (the fraction of IMF mass stored above say $1M_\odot$). In this study we have adopted the Salpeter law and $\zeta = 0.5$. With this assumption, at any given age the models predict $(M/L_B)_\odot$ ratios that are nearly constant at increasing luminosity (mass) of the galaxy, and at fixed galactic mass they increase by a factor of about 3 as the age goes from 5 to 15 Gyr.

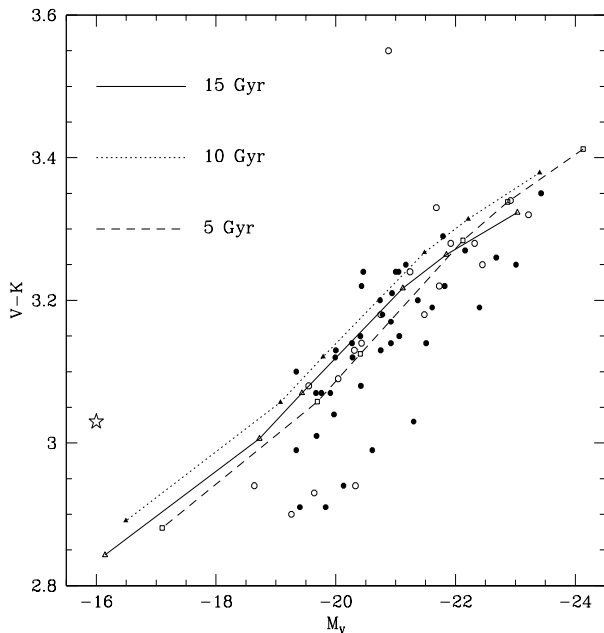


Fig. 13. The CMR for models with mass of 3, 1, 0.5, 0.1, 0.05, and 0.005 $M_{L,12}$ and different ages as indicated. The data for the galaxies in Virgo (*open circles*) and Coma (*filled circles*) are by Bower et al. (1992a,b). The *star* is the galaxy M32.

On the observational side, the M/L_B ratios (in solar units) by Bender et al. (1992, 1993) and Terlevich & Boyle (1993) – scaled to the Hubble constant $H_0 = 50 \text{ km sec}^{-1} \text{ Mpc}^{-1}$ – range from 1 to 18.

The comparison with the observational data is presented in Fig. 14 for different values of the age as indicated.

Therefore, while the mean values of the mass to blue luminosity ratios agree with the data, this type of model is still unable to explain the systematic increase of the mass to blue luminosity ratio with the galaxy luminosity for coeval, old objects as suggested by the CMR. Possible ways out are: (i) either faint galaxies are younger than the bright ones in contrast with the CMR hint or (ii) other causes must exist. In relation to this, Chiosi et al. (1998) have investigated the possibility that the IMF (cut-off mass and slope) vary from galaxy to galaxy in a systematic fashion: the IMF is more top-heavy (higher cut-off mass and shallower slope) in the massive elliptical galaxies than in the low mass ones (lower cut-off mass and steeper slope). Indeed Chiosi et al. (1998) models explain the inclination of the mass to light ratio versus luminosity (otherwise known as the inclination of the Fundamental Plane).

Before concluding this section we have to check the radial dependence of the $(M/L_B)_\odot$ predicted by the models. To this aim we calculate the cumulative $(M/L_B)_\odot(r_{j/2})$ moving from the center up to the last computed zone. The

results are presented in Table 9 limited to a few selected radii and the 3 and 0.1 $M_{L,T,12}$ galaxies. The selected radii $r_{j/2}$ correspond to the central core, $0.6R_{L,e}$, $R_{L,e}$ and $2R_{L,e}$. It is soon evident that the $(M/L_B)(r_{j/2})$ ratio is nearly constant (within about 10%) passing from the center to the external regions. *This implies that the first condition imposed by the choice of the Young (1976) density profile for the luminous material, i.e. radially constant mass to luminosity ratio, is almost fully verified.*

Table 8. The mass to blue-luminosity ratio (in solar units) as function of the age for the model galaxies with different mass.

Age	$M_{L,T,12}$	$M_{L,T}(t_{gw})$	M_B	L_B	$(M/L_B)_\odot$
15	3	0.660	-21.71	7.509e10	8.793
10	3		-22.11	1.085e11	6.083
5	3		-22.95	2.362e11	2.796
15	1	0.218	-20.54	2.559e10	8.540
10	1		-20.93	3.671e10	5.952
5	1		-21.65	7.138e10	3.061
15	0.5	0.109	-19.83	1.329e10	8.225
10	0.5		-20.21	1.890e10	5.786
5	0.5		-20.92	3.621e10	3.020
15	0.1	0.022	-18.19	2.951e9	7.463
10	0.1		-18.56	4.119e9	5.347
5	0.1		-19.24	7.741e9	2.845
15	0.05	0.011	-17.51	1.566e9	7.034
10	0.05		-17.86	2.170e9	5.077
5	0.05		-18.54	4.055e9	2.717

Table 9. The cumulative mass to blue-luminosity ratio $\log(M/L_B)_\odot$ at the age of 15 Gyr and as a function of the galacto-centric distance. $M_L(r_{j/2})$ in the mass in units of $10^{12} \times M_\odot$ contained in the sphere of radius $r_{j/2}$. The magnitudes and colours are the integrated values within the same sphere. The radii $r_{j/2}$ correspond to the central core, $0.6R_{L,e}$, $R_{L,e}$ and $2R_{L,e}$.

$M_{L,T,12}$	$r_{j/2}$	M_V	(B-V)	M_B	$M_L(r_{j/2})$	M/L_B
3	0.06	-21.07	1.00	-20.07	0.123	7.448
	0.58	-22.60	1.00	-21.64	0.632	8.976
	1.04	-22.69	0.99	-21.70	0.656	8.856
	1.48	-22.70	0.99	-21.70	0.660	8.803
0.1	0.06	-17.31	1.01	-16.30	0.004	8.466
	0.58	-18.96	0.93	-18.03	0.021	8.141
	1.04	-19.08	0.91	-18.17	0.022	7.511
	1.48	-19.10	0.91	-18.19	0.022	7.462

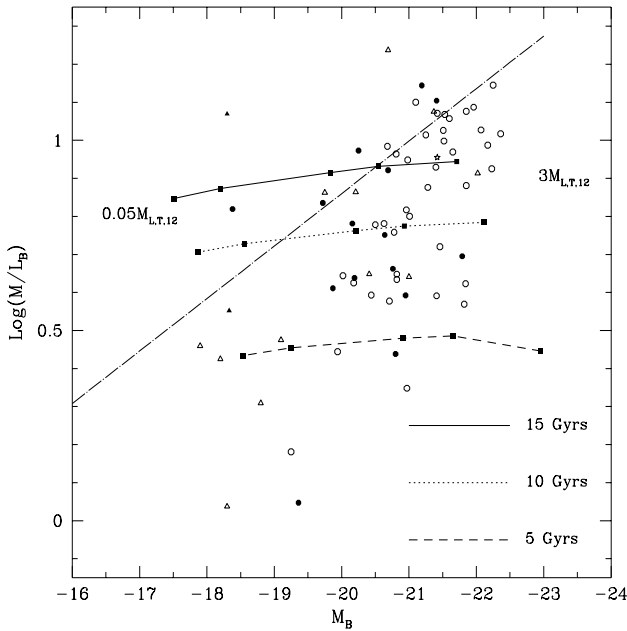


Fig. 14. The logarithm of the mass to B-luminosity ratio M/L_B versus the absolute blue magnitude M_B for the model galaxies at three different ages, i.e. 15, 10 and 5 Gyrs. The mass used to calculate M/L_B and M_B refers to the present-day mass in form of living stars. The ratio M/L_B is expressed in solar units. The *dashed line* is the relation by Terlevich & Boyle (1993) for $H_0 = 50 \text{ km sec}^{-1} \text{ Mpc}^{-1}$. The data are from Bender et al. (1992,1993), i.e. *open dots*: giant elliptical's; *full dots*: intermediate elliptical's; *stars*: bright dwarf elliptical's; *open squares*: compact elliptical's; *open triangles*: bulges

10.3. The UV excess

All studied elliptical galaxies have detectable UV flux short-ward of about 2000\AA (Burstein et al. 1988) with large variation from galaxy to galaxy. The intensity of the UV emission is measured by the colour $(1550-V)$. Our galaxy models are compared in the plane $(1550-V)$ versus M_V to the sample of galaxies by Burstein et al. (1988), see also Bender et al. (1992, 1993).

The 1550 fluxes by Burstein et al. (1988) are derived from IUE data, which refer to the region of a galaxy within $14''$ aperture. Assigning to the galaxies of Burstein et al. (1988) the distances calculated by Davies et al. (1987), the IUE aperture roughly corresponds to a radius of $\sim 1.234 \text{ Kpc}$ ($H_0 = 50 \text{ km/sec/Mpc}$). In contrast, the V magnitudes refer to the whole galaxy and therefore a different kind of correction to the theoretical data is required (see the case of the CMR above). Having done that, we derive the $(1550-V)$ colours of our model galaxies and compare it to the observational data. This is shown in the $(1550-V)$ versus M_V plane of Fig. 15 for three different values of the age (15, 10, and 5 Gyr) as indicated.

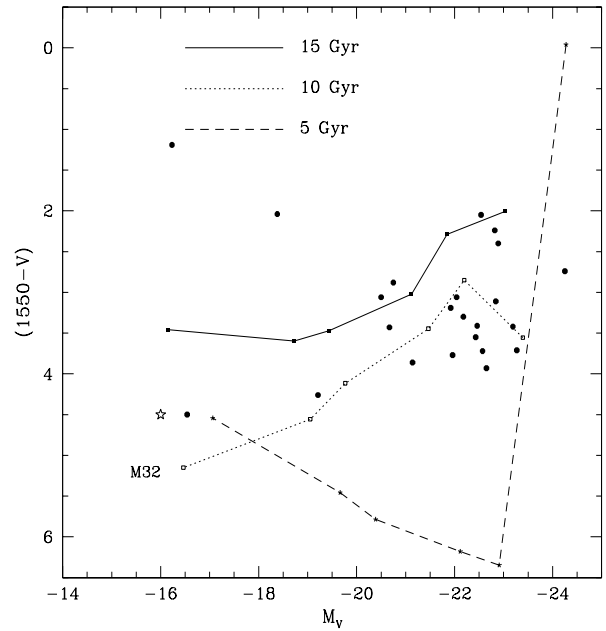


Fig. 15. The $(1550-V)$ versus M_V relation: the full dots are the data by Burstein et al. (1988), the lines show the theoretical predictions for the values of the age: 15 (*solid line*), 10 (*dotted line*), and 5 (*dashed line*) Gyr

10.4. Surface brightness

One of the key assumptions of our models was the adoption of the Young (1976) density profile for the luminous material and the implicit use of the condition that the models should asymptotically reproduce the $R^{1/4}$ law. Do the models match this constraint?

To answer the above question, we need to calculate the surface brightness of our models as a function of the age. The method is as follows. Let for each shell $F_{\Delta\lambda}(j/2)$ and $M_{\Delta\lambda}(j/2)$ indicate the total flux emitted in the pass-band $\Delta\lambda$ and the corresponding magnitude, respectively,

$$F_{\Delta\lambda}(j/2) = 10^{-0.4M_{\Delta\lambda}(j/2)} \quad (56)$$

where the flux $F_{\lambda}(j/2)$ is $\text{erg/s/cm}^2/\text{str}/\text{\AA}$. The flux per unit volume of each shell is

$$\Omega_{F_{\Delta\lambda}}(j/2) = \frac{F_{\Delta\lambda}(j/2)}{\Delta V_{j/2}} \quad (57)$$

where $\Delta V_{j/2}$ is the volume in kpc^3 of the j -th shell and $\Omega_{F_{\Delta\lambda}}(j/2)$ is in $\text{erg/s/cm}^2/\text{str}/\text{\AA}/\text{kpc}^3$.

Projecting the spherical shells onto a plane perpendicular to the line of sight and passing through the center, we can define the elemental volume

$$dV = \frac{(r_{j+1} - r_j)}{2} \times (r_{j+1} + r_j) \times d\theta \times dl \quad (58)$$

where r_{j+1} and r_j are the outer and inner radius of each shell, dl is the elemental length along the line of sight, and θ is the angle between a given reference line passing through the center and drawn on the above plane and any radial direction from the same center on the same plane. The angle θ varies in the interval $0 < \theta < \pi$. Elementary geometrical considerations set for the coordinate l the range of variation $0 < l < \sqrt{R^2 - r_j^2}$, where R is the external radius of the last shell. With the aid of this the flux emerging from the j -th shell corrected for the contribution from all overlaying layers is

$$F_{tot,\lambda}(j/2) = 2 \times \int_0^\pi d\theta \times \int_0^{\sqrt{r_{tot}^2 - r_j^2}} (r_{j+1} - r_j) \times (r_{j+1} + r_j) \Omega_{F_\lambda}(l) dl \quad (59)$$

with obvious meaning of $\Omega_{F_\lambda}(l)$.

Known the total flux emerging from each shell (since this flux has been derived from absolute magnitudes it corresponds to a source located at the distance of $10pc$), we derive the apparent magnitude and finally the surface brightness. To this aim, we fix an arbitrary distance d and scale the flux $F_{tot,\lambda}(j)$ of the ratio

$$\frac{1}{4\pi} \times \frac{(10pc)^2}{(d)^2}$$

thus obtaining the flux emitted per unit solid angle by a source located at the distance d .

Finally, the surface brightness is given by

$$\mu_\lambda(j) = -2.5 \log \left(\frac{F_{tot,\lambda}(j)(10pc)^2}{d^2 4\pi} \frac{1}{\Sigma} \right) \quad (60)$$

where Σ is the apparent projected surface of the galaxy up to the j -th shell as it would appear at the distance d . Given the external radius r_{j+1} of the shell, the corresponding angular surface up to that position is

$$\pi(\Theta(arcsec))^2 \quad \text{and} \quad \Theta = 206264.8 \frac{r_{j+1}}{d}$$

As expected the surface brightness $\mu_\lambda(j)$ does not depend on the arbitrary distance d introduced to calculate the apparent flux.

The surface brightness obtained from the above procedure is shown in Fig. 16 as a function of $(r/R_e)^{1/4}$ for the case of the $3M_{L,T,12}$ galaxy at the age of 15 Gyr. For the purpose of comparison, we also plot the reference $R^{1/4}$ law in arbitrary units (heavy solid line). *Despite the crudeness of our modelling the structure and evolution of elliptical galaxies, this fundamental condition is verified.*

In the same diagram we also plot the surface brightness at other ages, i.e. 0.005 Gyr (very early stage), 0.2 Gyr, and 1 Gyr. Since the mass-luminosity ratio is no longer constant in time and in space at these early epochs, larger

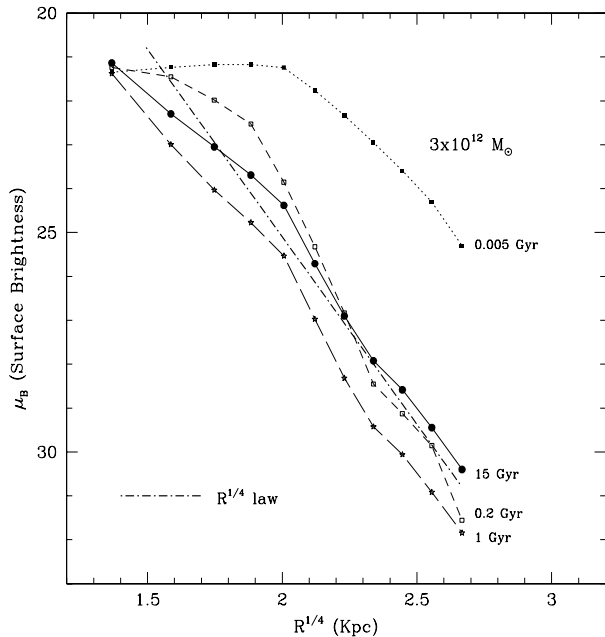


Fig. 16. The theoretical surface brightness profile for a model with $3M_{L,T,12}$ at different ages as indicated. The dot-dashed line is the $R^{1/4}$ law. Note how the models match the $R^{1/4}$ law when star formation throughout the galaxy is completed

departures from the $R^{1/4}$ law are expected and noticed. Remarkably at increasing galaxy age the luminosity profile gets closer and closer to the $R^{1/4}$ law simply reflecting the fact that a constant mass to luminosity ratio across the galaxy is gradually built up. Therefore we expect strong departures from the $R^{1/4}$ law over the period of time in which the front of star formation activity recedes from the periphery toward the center.

10.5. Gradients in broad-band colours and line strength indices

In this section we compare theoretical models and observational data in relation to the gradients in broad-band colours and line strength indices across individual galaxies. The discussion is limited to (B-R) and (1550-V), and H_β , Mg_2 , and (Fe). To this aim we prefer to adopt a unique albeit small set of data, i.e. the five galaxies studied by Carollo & Danziger (1994a), for the sake of internal homogeneity. The basic data for the galaxies in question are summarized in Table 10. Finally, we examine the distribution of the galaxies in the H_β versus [MgFe] plane and compare them with the predictions of theoretical models. The analysis is limited to the galaxies of the González (1993) sample.

Table 10. Basic data for the Carollo & Danziger (1994a) galaxies. The various quantities are: V the recession velocity; R_e the effective radius in arcsec; σ_0 the central velocity dispersion; D the distance in 10^4 kpc; R_e the effective radius in kpc; M the estimated mass in $10^{12}M_\odot$; m_B and M_B the apparent and absolute B-magnitudes, respectively; L_B/L_\odot the blue luminosity in solar units; $(M/L_B)_\odot$ the blue mass to luminosity ratio.

Name	V km/s	R_{eff} "	σ_0 km/s	D 10^4 kpc	R_{eff} kpc	M $10^{12}M_\odot$	m_B	M_B	L_B/L_\odot	$(M/L_B)_\odot$
NGC439	5679	45	—	11.36	24.78	—	12.38	-22.89	2.24(11)	—
NGC2434	1388	24	205	2.77	3.23	0.084	12.50	-19.72	1.20(10)	7.00
NGC3706	3046	27	281	6.09	7.97	0.39	11.87	-22.05	1.63(11)	3.78
NGC6407	4625	33	—	9.25	14.80	—	12.88	-21.95	9.38(10)	—
NGC7192	2761	28	185	5.52	7.50	0.16	12.21	-21.50	6.20(10)	2.56

10.5.1. Gradients in broad-band colours

To compare theoretical and observational colours we consider two galaxies of different luminosity and mass in turn, namely the high luminosity galaxy NGC 6407 shown in Fig. 17 and the somewhat fainter object NGC 2434 shown in Fig. 18. The colours are plotted as a function of the galacto-centric distance in units of effective radius. In Figs. 17 and 18, panels (a) show the data and the theoretical results for models of the same age (15 Gyr) and different mass, whereas panels (b) show the same but for models of given mass and different age.

In order to choose the model galaxy best matching the observational data we have made use of the $(M/L_B)_\odot$ ratio and selected the models whose $(M/L_B)_\odot$ is comparable to the observational one. We find that NGC 6407 and NGC 2434 well correspond to the 3 and $0.1M_{L,T,12}$ models, respectively. It is worth recalling that the two models have different properties: specifically star formation in the core stops at 5.12 and 1.45 Gyr and the mean metallicity is $Z_{mean} = 0.036$ and 0.031 in the 3 and $0.1M_{L,T,12}$ models respectively.

In the case of NGC 6407, it seems that the observational gradient is compatible with that of the old age model (15 Gyr). In the case of NGC 2434 the situation is less clear. First, there seems to be a systematic offset along the x-axis perhaps caused by an uncertainty in the distance. We estimate that a 5% shorter distance would yield a better agreement. Second, the slope of the colour gradient in the central regions is first flatter and then steeper than indicated by old ages curves. Perhaps, the hint arises for a mean age of the stellar content in the region $-1.5 \leq \log R/r_e \leq 1$ younger by several Gyr than in the outer regions. Recurrent or much prolonged episodes of star formation activity in the central regions would lead to bluer colours. The very central core require a slightly

different explanation, because if younger ages are invoked, they should be accompanied by significant metal enrichment in order to get a red colour over there, which indeed is as red as that of the old age case. The other galaxies of the sample show similar problems. This more complex history of star formation cannot be described by the present models, because they follow the classical SN-driven wind scheme according to which star formation is monolithic and of shorter duration at decreasing galaxy mass.

10.5.2. Gradients in (1550-V)

Another interesting gradient to look at is the one in the (1550-V) colour, whose theoretical expectation is shown in Fig. 19. The easiest way to understand the behaviour of the (1550-V) colour across the model galaxies is by means of SSP's with different metallicity, cf. for instance Fig. 5 in TCBF96. Our models have the following basic features: (i) the metallicity (both mean and maximum) increases toward the center; (ii) the relatively early galactic winds but for the very central region (cf. the entries of Table 4 or Fig. 10) secure that at the present age most of the galaxy is made by old stars with little age difference as we move inside (the oldest stars are in the outermost regions), whereas the central region may contain stars over a much wider age range. However, even in this case the bulk population is relatively old because of the time dependence of the star formation rate. Therefore, for the whole galaxy but the center, to a first approximation we can assume that all stars are nearly coeval but get more and more metal-rich going toward the center. In such a case the effect of an increasing metallicity is that the colour (1550-V) gets larger and larger. In the central core we have the combined effect of a higher metallicity and the presence of a younger stellar component. If the metallicity is $Z \leq 0.05$, the presence of younger ages would increase (1550-V) even

further (cf. Fig. 5 in TCBF96). However, this trend is destroyed by the presence of even small traces of high metallicity stars (say $Z \geq 0.05$). In such a case, AGB-manqué and H-HB stars older than about 5.6 Gyr (with the SSP's in usage) that are powerful, long-lived sources of UV radiation reverse the trend in (1550-V) colour, which gets "blue" again. A detailed discussion of this effect can be found in Bressan et al. (1994) and TCBF96 to whom the reader should refer. Observational data on gradients in (1550-V) are not yet available to our knowledge.

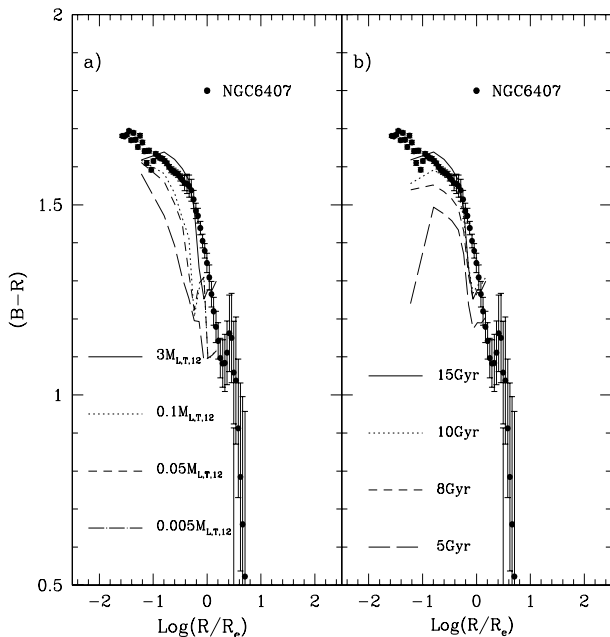


Fig. 17. The gradient in the (B-R) colour across the galaxy NGC 6407 (full dots). The data are from Carollo & Danziger (1994a). Panel (a) shows the colour gradient for models of the same age (15 Gyr) and different $M_{L,T,12}$ as indicated. Panel (b) displays the colour gradient for the model with $3M_{L,T,12}$ and different ages: 15 (solid line), 10 (dotted line), and 5 (dashed line) Gyr

10.5.3. Gradients in line strength indices

Adopting the method described in Bressan et al. (1996), we have calculated the temporal and spatial evolution of the line strength indices in our model galaxies. The definition of the line strength indices strictly follows Worthey (1992) and Worthey et al. (1994). In particular we made use of their fitting functions, in which there is no dependence on the possible enhancement in α elements with respect to iron expressed by $[\alpha/\text{Fe}]$ with the usual meaning of the notation. Complete tabulations of the indices are available from the authors upon request.

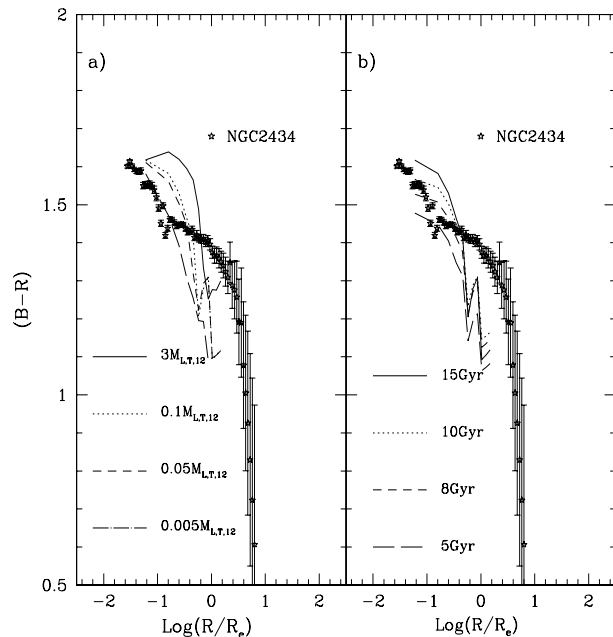


Fig. 18. The gradient in the (B-R) colour across the galaxy NGC 2434 (full dots). The data are from Carollo & Danziger (1994a). Panel (a) shows the colour gradient for models of the same age (15 Gyr) and different $M_{L,T,12}$ as indicated. Panel (b) displays the colour gradient for the model with $0.1M_{L,T,12}$ and different ages: 15 (solid line), 10 (dotted line), and 5 (dashed line) Gyr

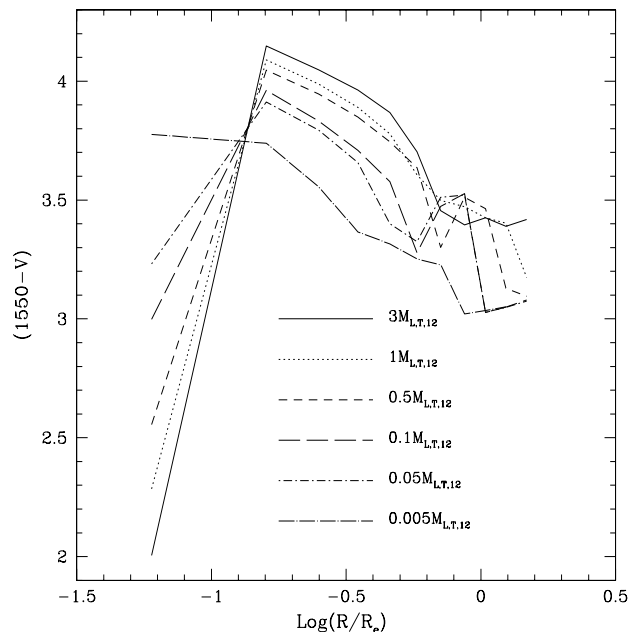


Fig. 19. The predicted gradient in the (1550-V) colour for the models with different $M_{L,T,12}$ as indicated

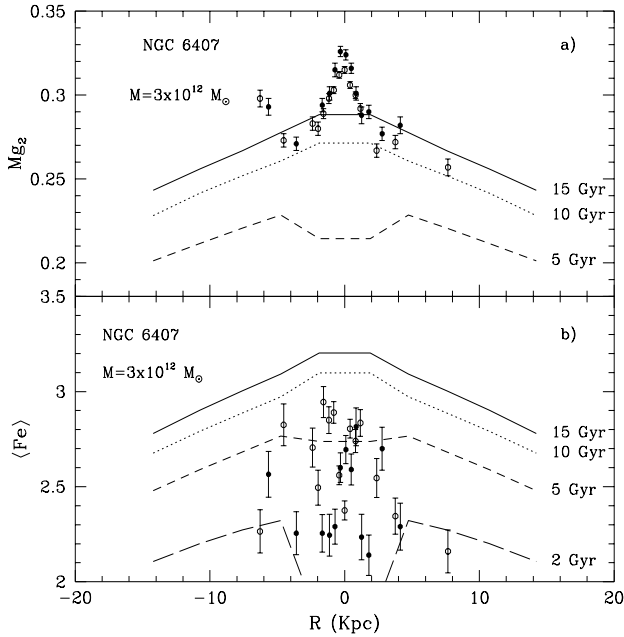


Fig. 20. The line indices Mg_2 and $\langle Fe \rangle$ as function of the galacto-centric distance, *panel a*) and *panel b*) respectively, as measured by Carollo & Danziger (1994a) along the major (*full dots*) and minor axis (*empty dots*) of NGC 6407. Superposed are the theoretical gradients at three different values of the age as indicated

We compare here the gradients in Mg_2 and $\langle Fe \rangle$ observed in the galaxies NGC 6407 (Fig. 20) and NGC 2434 (Fig. 21), with those predicted by the same models used in the analysis of the (B-R) colours. In both diagrams, the top panel is for Mg_2 , the bottom panel for $\langle Fe \rangle$. The filled circles indicate the indices measured along the major axis, while the open circles show the same but along the minor axis. The theoretical gradients are displayed for several values of the age as indicated.

It is soon evident that these models fail in reproducing the gradients in the Mg_2 and $\langle Fe \rangle$. The situation is nearly the same for both galaxies. Surprisingly, the disagreement is stronger for NGC 6407 for which the gradient in (B-R) was reproduced. No obvious causes of the failure can be found on the basis of the present calculations.

10.5.4. The H_β -[MgFe] plane

Despite the above failure we look at the evolutionary path of the central region of the models in the H_β -[MgFe] plane and compare it with the Re/8-data from the González (1993) sample of elliptical galaxies, which is indicative of the central properties of the galaxies. The comparison is shown in Fig. 22 limited to the models with total mass of 3, 0.1 and $0.005 M_{L,T,12}$. Since the theoretical indices are calculated using calibrations that do not take into account

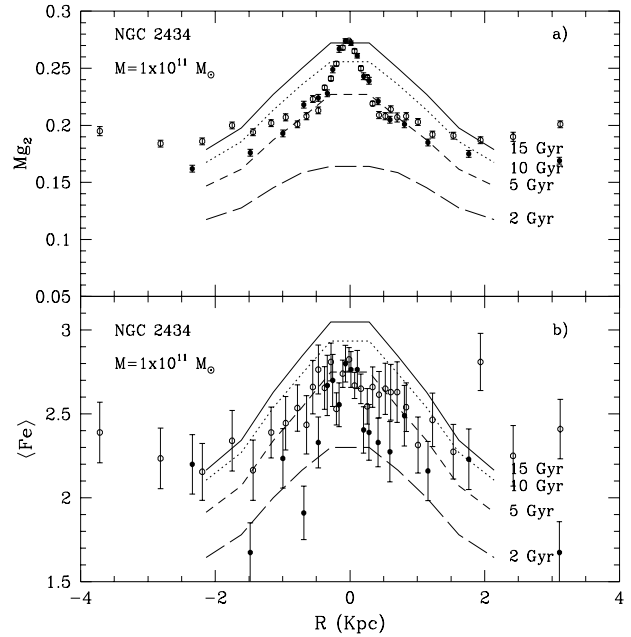


Fig. 21. The line indices Mg_2 and $\langle Fe \rangle$ as function of the galacto-centric distance, *panel a*) and *panel b*) respectively, as measured by Carollo & Danziger (1994a) along the major (*full dots*) and minor axis (*empty dots*) of NGC 2434. Superposed are the theoretical gradients at three different values of the age as indicated

the possible enhancement in α -elements which in contrast is suspected to exist in elliptical galaxies from the analysis of the line strength indices Mg_2 and $\langle Fe \rangle$ and their gradients, see for instance the recent reviews by Matteucci (1994, 1997) and the above discussion, to somehow cope with this marginal discrepancy in plotting the theoretical results we have applied the offset $\Delta \log [MgFe] = 0.05$ (cf. also Bressan et al. 1996).

Remarkably and even more intriguing, data and theoretical results seem to agree each other, in the sense that the general trend shown by the data is recovered by the models.

The long debated question posed by this diagram is whether or not galaxies span a large range of ages. The point is made evident looking at line of constant age drawn in Fig. 22. It is worth recalling that along each theoretical sequence the age increases from the top to the bottom of the diagram.

Before going further, we clarify that the observational uncertainty cannot be the cause of the observed spread, along the H_β axis in particular. According to González (1993) the uncertainty in [MgFe] is very small, not exceeding $\Delta[MgFe] = \pm 0.03$, whereas that in H_β is larger, but also in this case not exceeding $\Delta H_\beta = \pm 0.06$.

The studies by Bressan et al. (1996) and Greggio (1996) on the distribution of galaxies in the H_β versus

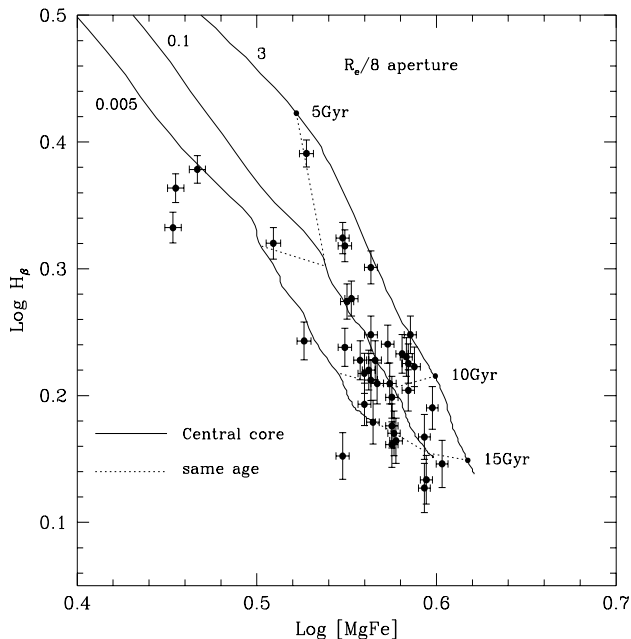


Fig. 22. Evolution of central region of the model galaxies (solid lines) in the H_β -[MgFe] plane. The dotted lines are the loci of constant age as indicated. The full dots are the $R_e/8$ -data of González (1993) with their observational uncertainties

[MgFe] plane with the aid of SSP's and/or complete models or both have come to a number of interesting yet demanding conclusions:

- Galaxies span a small range of mean metallicities (Bressan et al. 1996; Greggio 1966).
- The percentage of low metallicity stars is small. This can be achieved either by infall (TCBF96) or prompt enrichment (Greggio 1966).
- The distribution of galaxies in the H_β versus [MgFe] plane does not agree with the expectation from the CMR if this latter is the locus of old, nearly coeval galaxies (see the 15 Gyr locus in Fig. 22). However, as the CMR we refer to is for cluster galaxies, whereas the González sample includes both cluster and field objects, the discrepancy is not conclusive, see Bressan et al. (1996) for more details.
- Based on the difference between the $R_e/8$ and $R_e/2$ -data (this latter sampling a wider area of the galaxies, cf. González 1993 for details) Bressan et al. (1996) suggested that in most galaxies the nucleus was younger, or more precisely star formation lasted longer, and more metal-rich than the external regions.
- Finally, Bressan et al. (1996) also proposed that the overall duration of the star formation activity, at least

in the central regions, ought to be increase at decreasing galaxy mass.

In the present models, while star formation in the nucleus lasts longer thus leading to higher metallicities than in the external regions, still the total duration of the star forming activity is shorter at decreasing galaxy mass (the SN-driven wind scheme with constant IMF). Therefore, the questions posed by the H_β versus [MgFe] plane cannot be answered by the models in question even if with their spatial gradients in star formation they provide better leverage than the classical one-zone models.

11. Summary and Conclusions

In this paper we have described a simple multi-zone model of spherical galaxies in which spatial gradients in mass density and star formation are taken into account. The model, which is an extension of the classical one-zone infall model, aims at following the history of star formation and chemical enrichment taking place in primeval gas falling into the potential well of dark matter.

Given a certain spherical distribution of dark matter supposedly constant with time, the primeval gas is let flow in and gradually build up the spherical distribution of baryonic mass originally in form of gas and later in form of stars. Since there is no dynamics in our model, the action consists in supposing that the mass of each spherical shell gradually increase at a suitable rate so that the final radial distribution of baryonic mass matches the one inferred from observational data for real galaxies. In the adopted scheme each shell is supposed to evolve without exchanging material with the surrounding shells, in a sort of one-zone approximation. The lack of radial motions of gas toward the center is clearly the major drawback of our model, which eventually finds its justification only in the quality and robustness of the final results as compared to observational data.

The time of the local increase in baryonic mass seeks to closely follow the gross features emerging from fully dynamical models of galaxy formation: in a typical structure the radial velocity first increases to a maximum and then decrease to zero at decreasing galacto-centric distance. This implies that the rate of mass accretion is a function of the radial distance, being large both at the center and in the external regions and small in between, the minimum being reached at a certain typical radius.

The local rate of star formation is assumed to follow the Schmidt law, i.e. $\dot{\rho}(r, t)_s = \nu(r)\rho_g(r, t)^\kappa$ with $\kappa = 1$, where the proportionality factor $\nu(r)$ is a suitable function of the galacto-centric distance. It ultimately stems from the competition between the local free-fall and collision time scale as far as the global mode of star formation is concerned. This makes the specific efficiency of star formation increase outward.

It is worth recalling that owing to the way the problem has been formulated there are no free parameters in the

accretion time scale and efficiency of star formation. Both follow from assigning the mass of the galaxy.

All other physical ingredients of the model, e.g. the ratio of dark matter to baryonic mass, the IMF, and the nucleosynthesis prescriptions are standard. They can be changed without altering the main scenario emerging from this study. The mass of dark matter and its spatial distribution simply affect the total gravitational potential, and the epoch of galactic wind in turn. The IMF is the classical Salpeter law with $x = 2.35$ and $\zeta = 0.5$. This latter parameter is the fraction of mass in the IMF above $1M_{\odot}$, driving the nucleosynthesis enrichment and the mass-luminosity ratio. As already recalled, the value $\zeta = 0.5$ has been chosen so that the mean mass to blue luminosity ratios for the elliptical galaxies of the Bender et al. (1992, 1993) sample are matched.

Care has been paid to check whether the baryonic component of the model satisfies its most demanding constraints: (i) constant mass-luminosity ratio with the radius; (ii) $R^{1/4}$ luminosity profile. Considering the fully independent scheme on which the building up of the luminous component and associated star formation are based, the successful matching of the above constraints perhaps hints that the model despite its crudeness is on the right track and can be safely utilized to predict the gross features of the spatial gradients in metallicity, partition function $N(Z)$, ages, broad-band colours, and line strength indices of spherical (elliptical as well) galaxies to be compared with observational data. Main results of this study are:

(1) Galactic winds occur later (more precisely star formation is halted because the local thermal content of the gas exceeds the gravitational potential) as we move inward, i.e. galaxies are viewed as an *outside-in process*, in such a way that the older populations are expected in the external regions of the galaxy. Likewise, the star forming activity lasts longer at increasing galactic mass. In this context, the present models strictly conform to the classical supernova driven galactic wind scenario.

(2) As a result, the external regions contain stars that are richer in α -elements than the inner ones, and the more massive models are on the average less enhanced in α -elements than the low mass ones. Also in this respect, the present models conform the expectation from the classical supernova driven galactic wind scenario. This is not specific to our model but common to all chemical models with monolithic star formation and constant IMF. Line strength indices such as Mg_2 and $\langle Fe \rangle$ seem to require the opposite trend: more α -enhancement toward the center in more massive galaxies.

(3) The color-magnitude relation, and the mean mass to blue luminosity ratios can be easily matched. The CMR is best explained by old, nearly coeval galaxies of different mean metallicity (increasing with the galaxy luminosity and hence mass). However, concerning the M/L_B ratio, like all other models of this type (i.e. with constant IMF)

the increase by approximately a factor of 3 to 5 passing from low to high mass elliptical galaxies (the so-called tilt of the FP) cannot be reproduced without relaxing the notion of coevality.

(4) The observational H_{β} and $[MgFe]$ for the central regions of elliptical galaxies are reproduced by the models, which however are still not able to answer the question posed by H_{β} - $[MgFe]$ plane, i.e. if and why elliptical galaxies may have undergone star formation over long periods of time, some in the far past other in more recent epochs.

(5) The models are marginally able to reproduce gradients in broad band colors but have serious difficulties as far as the gradients in the line strength gradients are concerned. The nature of the disagreement is not easy to understand because all the models possess well behaved gradients in star formation (lasting longer toward the center) and mean and maximum metallicity (increasing toward the center). It seems as if in addition to the gross scheme we have considered, real galaxies had a more complicated history of star formation to which the line strength indices are more sensitive than the broad band colors or the integrated properties. Reconstructing the kind of star formation that satisfies all the constraints imposed by observational data of real galaxies is a cumbersome affair beyond the capability of the present model. Owing to its importance, the whole problem is addressed in a companion paper (Tantalo et al. 1998), in which the effects of different calibrations for the indices as a function of effective temperature, gravity, metal content, and degree of enhancement in α -elements of the constituent stars, and different histories of star formation and chemical enrichment of the models have been thoroughly scrutinized. No details of this investigation are given here for the sake of brevity.

In summary, despite its gross simplification of the physics leading to the formation of a galaxy, the model we have presented successfully reproduces some of the properties of real galaxies but fails in others, the gradients in line strength indices in particular. However, considering the global performance of the model, we are confident that it can be safely utilized to investigate the properties of elliptical under different assumptions concerning the IMF, the past history of star formation (monolithic in the early past or recurrent in several episodes), and the SN-driven galactic wind mechanism.

Acknowledgements. C.C. is pleased to acknowledge the kind hospitality and the highly stimulating environment provided by ESO in Garching where this paper was written up during sabbatical leave from the Astronomy Department of the Padua University. This study has been funded by the Italian Ministry of University, Scientific Research and Technology (MURST), the Italian Space Agency (ASI), and the European Community TMR grant # ERBFMRX-CT96-0086.

References

- Arimoto N., & Yoshii, Y. 1987, A&A 173, 23
- Angeletti L., & Giannone P., 1990, A&A 234, 53
- Balcells M., & Peletier R. F., 1994, AJ 107, 135
- Baum W.A., 1959, PASP 71, 106
- Bender R., Burstein D., & Faber S.M., 1993, ApJ 411, 153
- Bender R., Burstein D., & Faber S.M., 1992, ApJ 399, 462
- Bertelli G., Bressan A., Chiosi C., Fagotto F., & Nasi E., 1994, A&AS 106, 275
- Bertin G., Saglia R. P., & Stiavelli M., 1992, ApJ 384, 423
- Bethe H.A. 1990, Reviews of Modern Physics, 62, no. 4, 801
- Bower R. G., Lucey J. R., & Ellis R.S., 1992a, MNRAS 254, 589
- Bower, R. G., Lucey J. R., & Ellis R.S., 1992b, MNRAS 254, 601
- Branch D., & Tammann G.A., 1992, ARA&A 30, 359
- Bressan A., Chiosi C., & Fagotto F., 1994, ApJS 94, 63
- Bressan A., Chiosi C., & Tantalo R., 1996, A&A 311, 425
- Burstein D., Bertola F., Buson L.M., Faber S.M., & Lauer T.R., 1988, ApJ 328, 440
- Carollo C.M., & Danziger I.J., 1994a, MNRAS 270, 523
- Carollo C.M., & Danziger I.J., 1994b, MNRAS 270, 743
- Carollo C.M., Danziger I.J., & Buson L., 1993, MNRAS 265, 553
- Carraro G., Lia C., & Chiosi C. 1997, MNRAS, submitted
- Chiosi C., Bressan A., Portinari L., & Tantalo R., 1998, A&A, accepted, *astro-ph/9708123*
- Chiosi C., & Maeder A., 1986, ARA&A 24, 329
- Cioffi D.F., McKee C.F., & Bertschinger E., 1988, ApJ 334, 252
- Ciotti L., 1991, A&A 249, 99
- Cox D.P., 1972, ApJ 178, 159
- Davies R.L., Burstein D., Dressler A., Faber S.M., Lynden-Bell D., Terlevich R.J., & Wagner G., 1987, ApJS 64, 581
- Davies R.L., Sadler E.M., & Peletier R., 1993, MNRAS 262, 650
- Fasano G., Filippi M., & Bertola F., 1997, in press
- Fisher D., M. Franx, & Illingworth G., 1995, ApJ 448, 119
- Fisher D., M. Franx, & Illingworth G., 1996, ApJ 459, 110
- Gibson B.K., 1994, MNRAS 271, L35
- Gibson B.K., 1996, MNRAS 278, 829
- Gibson B.K., 1997, preprint
- Gibson B.K., & Matteucci F., 1997, ApJ 475, 47
- González J.J., 1993, Ph.D. Thesis, Univ. California, Santa Cruz
- Goudfrooij P., Hansen L., Jørgensen H.E., Nørgaard-Nielsen H.U., de Jong T., & van den Hoek L.B., A&AS 104, 179
- Greggio L., 1996, MNRAS 285, 151
- Koo B.C., & McKee C.F., 1992, ApJ 388, 103
- Kudritzki K.P., Pauldrach A., & Puls J., 1987, A&A 173, 293
- Larson R.B., 1991, in *Frontiers of Stellar Evolution*, D. L. Lambert (ed.), ASP Conference Series, Vol. 20, p.571
- Larson R.B., 1974, MNRAS 166, 585
- Marigo P., Bressan A., & Chiosi C., 1996, A&A 313, 545
- Marigo P., Bressan A., & Chiosi C., 1998, A&A, accepted, *astro-ph/9710093*
- Matteucci F., & Greggio L., 1986, A&A 154, 279
- Matteucci F., & Tornambé A., 1987, A&A 185, 51
- Matteucci F., 1997, *Fund. Cosmic Phys.*, in press
- Matteucci F., 1994, A&A 288, 57
- Mihara K., & Takahara F., 1994, PASJ 46, 447
- Ostriker J.P., & McKee C.F., 1988, Rev. Mod. Phys. 60, 1
- Portinari L., Chiosi C., & Bressan A., 1998, A&A accepted, *astro-ph/97111337*
- Poveda A., Iturriaga R., & Orozco I., 1960, Bol. Obs. Tonantzintla 20, 3
- Saito M., 1979a, PASJ 31, 181
- Saito M., 1979b, PASJ 31, 193
- Saglia R.P., Bertin G., & Stiavelli M., 1992, ApJ 384, 433
- Schmidt M., 1959, ApJ 129, 243
- Silk J., 1977, ApJ 214, 718
- Talbot R.J., & Arnett D.W., 1973, ApJ 170, 409
- Tantalo R., Chiosi C., Bressan A., & Fagotto F., 1996, A&A 311, 361, TCBF96
- Tantalo R., Bressan A., & Chiosi C., 1998, A&A, accepted, *astro-ph/9710101*
- Terlevich R., & Boyle B.J., 1993, MNRAS, in press
- Theis Ch., Burkert A., & Hensler G., 1992, A&A 265, 465
- Young P.J., 1976, AJ 81, 807
- Weaver R., McCray R., Castor J, Shapiro P., & Moore R., 1977, ApJ 218, 377
- Worthey G., Faber S.M., González J.J., & Burstein D., 1994, ApJS 94, 687
- Worthey G., Faber S.M., & González J.J., 1992, ApJ 398, 69

Table 4: Chemical Models at the Stage of Wind Ejection

$M_{L,T,12}$	$\nu(r_{j/2})$	ζ	$\tau(r_{j/2})$	$M_{L,t}$	$t_{g\omega}$	$G(r_{j/2,t})$	$S(r_{j/2,t})$	$Z(r_{j/2,t})$	$\langle Z(r_{j/2,t}) \rangle$	Ψ	Ω_g	E_g	E_{SNI}	E_{SNIH}	E_{SW}
(1)	(2)	(3)	(4)	(5)	(6)	(7)	(8)	(9)	(10)	(11)	(12)	(13)	(14)	(15)	(16)
3.0	7.1	0.50	0.74	0.14550	5.12	0.004	0.845	0.0964	0.0365	3.67E+00	2.99E+08	2.99E+08	7.99E+07	2.18E+08	1.67E+06
3.0	50.0	0.50	0.29	0.15000	0.79	0.010	0.874	0.0439	0.0286	6.97E+01	2.34E+08	2.34E+08	2.26E+07	2.06E+08	4.82E+06
3.0	111.6	0.50	0.18	0.15010	0.38	0.011	0.834	0.0362	0.0266	1.74E+02	2.04E+08	2.28E+08	1.20E+07	2.09E+08	6.97E+06
3.0	198.6	0.50	0.13	0.14990	0.21	0.013	0.764	0.0323	0.0251	3.63E+02	2.08E+08	2.30E+08	6.35E+06	2.14E+08	9.27E+06
3.0	325.5	0.50	0.10	0.15000	0.11	0.015	0.637	0.0293	0.0232	6.97E+02	2.20E+08	2.41E+08	1.84E+06	2.28E+08	1.14E+07
3.0	501.4	0.50	0.14	0.15000	0.05	0.012	0.284	0.0261	0.0197	9.04E+02	1.73E+08	1.81E+08	0.00E+00	1.73E+08	7.91E+06
3.0	753.8	0.50	0.20	0.15000	0.02	0.007	0.102	0.0236	0.0134	7.79E+02	9.28E+07	9.53E+07	0.00E+00	9.16E+07	3.76E+06
3.0	1116.0	0.50	0.27	0.15000	0.01	0.004	0.038	0.0148	0.0050	5.83E+02	4.54E+07	4.56E+07	0.00E+00	4.45E+07	1.10E+06
3.0	1632.9	0.50	0.35	0.15020	0.01	0.002	0.022	0.0102	0.0102	4.41E+02	2.30E+07	2.30E+07	0.00E+00	2.25E+07	5.05E+05
3.0	2383.7	0.50	0.46	0.14990	0.01	0.001	0.016	0.0092	0.0092	3.38E+02	1.21E+07	1.26E+07	0.00E+00	1.23E+07	3.07E+05
3.0	3493.2	0.50	0.59	0.15020	0.01	0.001	0.011	0.0079	0.0079	2.61E+02	6.41E+06	6.56E+06	0.00E+00	6.38E+06	1.86E+05
1.0	9.0	0.50	0.52	0.04850	3.60	0.005	0.864	0.0947	0.0351	1.92E+00	7.59E+07	8.37E+07	2.01E+07	6.30E+07	6.72E+05
1.0	60.6	0.50	0.20	0.05001	0.54	0.012	0.875	0.0412	0.0275	3.41E+01	5.80E+07	6.56E+07	4.61E+06	5.90E+07	1.95E+06
1.0	132.8	0.50	0.13	0.05002	0.25	0.014	0.818	0.0344	0.0255	9.21E+01	5.55E+07	6.20E+07	1.86E+06	5.72E+07	2.90E+06
1.0	233.3	0.50	0.09	0.04995	0.13	0.018	0.722	0.0311	0.0237	2.01E+02	6.01E+07	6.03E+07	5.86E+05	5.59E+07	3.86E+06
1.0	378.3	0.50	0.07	0.05001	0.07	0.020	0.592	0.0290	0.0216	3.64E+02	6.05E+07	6.22E+07	2.26E+04	5.76E+07	4.60E+06
1.0	577.3	0.50	0.10	0.05001	0.04	0.015	0.309	0.0268	0.0184	4.11E+02	4.19E+07	4.50E+07	0.00E+00	4.18E+07	3.23E+06
1.0	860.3	0.50	0.14	0.04999	0.02	0.009	0.112	0.0228	0.0108	3.60E+02	2.31E+07	2.35E+07	0.00E+00	2.21E+07	1.42E+06
1.0	1262.8	0.50	0.19	0.05000	0.01	0.004	0.044	0.0105	0.0105	2.71E+02	1.14E+07	1.15E+07	0.00E+00	1.11E+07	3.44E+05
1.0	1832.5	0.50	0.24	0.05006	0.01	0.002	0.027	0.0082	0.0082	2.07E+02	5.91E+06	6.70E+06	0.00E+00	6.54E+06	1.60E+05
1.0	2653.1	0.50	0.32	0.04997	0.01	0.001	0.019	0.0068	0.0068	1.59E+02	3.13E+06	3.47E+06	0.00E+00	3.38E+06	8.91E+04
1.0	3855.9	0.50	0.41	0.05007	0.01	0.001	0.014	0.0065	0.0065	1.23E+02	1.68E+06	2.13E+06	0.00E+00	2.07E+06	6.12E+04
0.5	10.4	0.50	0.42	0.02425	2.68	0.006	0.879	0.0876	0.0338	1.41E+00	3.54E+07	3.60E+07	7.59E+06	2.80E+07	3.91E+05
0.5	68.3	0.50	0.16	0.02500	0.40	0.015	0.860	0.0386	0.0266	2.52E+01	2.78E+07	2.81E+07	1.41E+06	2.55E+07	1.15E+06
0.5	148.3	0.50	0.10	0.02501	0.19	0.018	0.803	0.0335	0.0248	6.25E+01	2.48E+07	2.71E+07	4.99E+05	2.49E+07	1.67E+06
0.5	258.5	0.50	0.07	0.02498	0.10	0.020	0.723	0.0311	0.0231	1.24E+02	2.46E+07	2.71E+07	1.24E+05	2.48E+07	2.19E+06
0.5	416.3	0.50	0.06	0.02500	0.06	0.022	0.593	0.0293	0.0208	2.24E+02	2.49E+07	2.60E+07	0.00E+00	2.34E+07	2.61E+06
0.5	631.6	0.50	0.08	0.02500	0.03	0.017	0.305	0.0269	0.0167	2.55E+02	1.74E+07	1.77E+07	0.00E+00	1.60E+07	1.75E+06
0.5	936.1	0.50	0.11	0.02499	0.02	0.010	0.118	0.0227	0.0087	2.20E+02	9.55E+06	9.56E+06	0.00E+00	8.82E+06	7.37E+05
0.5	1366.9	0.50	0.15	0.02500	0.01	0.005	0.049	0.0095	0.0095	1.68E+02	4.81E+06	4.98E+06	0.00E+00	4.82E+06	1.64E+05
0.5	1973.4	0.50	0.20	0.02503	0.01	0.003	0.032	0.0071	0.0071	1.28E+02	2.51E+06	3.18E+06	0.00E+00	3.10E+06	7.94E+04
0.5	2842.6	0.50	0.25	0.02498	0.01	0.001	0.022	0.0056	0.0056	9.87E+01	1.34E+06	1.52E+06	0.00E+00	1.48E+06	3.82E+04
0.5	4110.1	0.50	0.33	0.02503	0.01	0.001	0.016	0.0049	0.0049	7.65E+01	7.21E+05	8.70E+05	0.00E+00	8.47E+05	2.35E+04
0.1	14.7	0.50	0.25	0.00485	1.45	0.008	0.902	0.0765	0.0312	5.74E-01	4.99E+06	5.33E+06	8.14E+05	4.41E+06	1.07E+05
0.1	90.6	0.50	0.10	0.00500	0.22	0.022	0.850	0.0367	0.0251	9.43E+00	3.84E+06	4.36E+06	9.66E+04	3.95E+06	3.14E+05
0.1	191.9	0.50	0.06	0.00500	0.10	0.027	0.766	0.0327	0.0229	2.48E+01	3.71E+06	3.93E+06	1.03E+04	3.45E+06	4.66E+05
0.1	328.7	0.50	0.04	0.00500	0.05	0.029	0.681	0.0315	0.0208	4.64E+01	3.53E+06	3.67E+06	0.00E+00	3.07E+06	6.00E+05
0.1	521.4	0.50	0.03	0.00500	0.04	0.028	0.617	0.0323	0.0184	6.98E+01	3.03E+06	3.54E+06	0.00E+00	2.85E+06	6.91E+05
0.1	780.8	0.50	0.05	0.00500	0.02	0.021	0.326	0.0260	0.0127	8.11E+01	2.20E+06	2.29E+06	0.00E+00	1.86E+06	4.25E+05
0.1	1142.8	0.50	0.07	0.00500	0.01	0.013	0.129	0.0118	0.0040	7.04E+01	1.22E+06	1.22E+06	0.00E+00	1.11E+06	1.14E+05
0.1	1648.8	0.50	0.09	0.00500	0.01	0.007	0.067	0.0066	0.0066	5.48E+01	6.39E+05	7.26E+05	0.00E+00	6.95E+05	3.03E+04
0.1	2352.9	0.50	0.12	0.00501	0.01	0.004	0.041	0.0034	0.0034	4.22E+01	3.38E+05	3.58E+05	0.00E+00	3.51E+05	7.00E+03
0.1	3350.2	0.50	0.15	0.00500	0.00	0.002	0.029	0.0027	0.0027	3.26E+01	1.83E+05	1.89E+05	0.00E+00	1.86E+05	2.90E+03
0.1	4787.8	0.50	0.20	0.00501	0.00	0.001	0.024	0.0033	0.0033	2.54E+01	1.01E+05	1.63E+05	0.00E+00	1.60E+05	3.16E+03
0.05	17.0	0.50	0.20	0.00243	1.08	0.010	0.912	0.0720	0.0299	3.90E-01	2.15E+06	2.34E+06	2.95E+05	1.98E+06	6.19E+04
0.05	102.4	0.50	0.08	0.00250	0.16	0.028	0.825	0.0354	0.0241	7.04E+00	1.86E+06	1.86E+06	2.04E+04	1.65E+06	1.86E+05
0.05	214.6	0.50	0.05	0.00250	0.08	0.031	0.759	0.0327	0.0221	1.59E+01	1.56E+06	1.72E+06	9.21E+02	1.45E+06	2.67E+05
0.05	364.9	0.50	0.03	0.00250	0.05	0.032	0.689	0.0331	0.0199	2.82E+01	1.42E+06	1.52E+06	0.00E+00	1.18E+06	3.41E+05
0.05	575.2	0.50	0.03	0.00250	0.03	0.033	0.591	0.0322	0.0159	4.54E+01	1.31E+06	1.36E+06	0.00E+00	9.89E+05	3.74E+05
0.05	856.5	0.50	0.04	0.00250	0.02	0.024	0.325	0.0255	0.0102	4.98E+01	9.04E+05	9.14E+05	0.00E+00	6.96E+05	2.18E+05
0.05	1247.1	0.50	0.05	0.00250	0.01	0.014	0.140	0.0108	0.0108	4.31E+01	5.04E+05	5.07E+05	0.00E+00	4.51E+05	5.60E+04
0.05	1790.2	0.50	0.07	0.00250	0.01	0.008	0.077	0.0055	0.0055	3.38E+01	2.67E+05	3.15E+05	0.00E+00	3.02E+05	1.39E+04
0.05	2542.1	0.50	0.09	0.00250	0.01	0.004	0.051	0.0035	0.0035	2.61E+01	1.43E+05	2.06E+05	0.00E+00	2.02E+05	4.51E+03

Table 4: Chemical Models at the Stage of Wind Ejection *continued*

(1)	(2)	(3)	(4)	(5)	(6)	(7)	(8)	(9)	(10)	(11)	(12)	(13)	(14)	(15)	(16)	(17)
0.05	3602.2	0.50	0.12	0.00250	0.00	0.002	0.037	0.0027	0.0027	2.02E+01	7.81E+04	1.16E+05	0.00E+00	1.15E+05	1.79E+03	1.241
0.05	5122.6	0.50	0.16	0.00250	0.00	0.001	0.026	0.0019	0.0019	1.58E+01	4.30E+04	4.73E+04	0.00E+00	4.69E+04	4.00E+02	1.476
0.005	27.7	0.50	0.09	0.00024	0.44	0.018	0.920	0.0583	0.0269	1.18E-01	1.43E+05	1.57E+05	9.09E+03	1.38E+05	1.03E+04	0.060
0.005	154.1	0.50	0.04	0.00025	0.07	0.048	0.785	0.0358	0.0210	1.81E+00	1.14E+05	1.21E+05	6.61E+00	9.11E+04	3.01E+04	0.156
0.005	312.3	0.50	0.03	0.00025	0.03	0.049	0.686	0.0360	0.0172	3.76E+00	9.10E+04	9.52E+04	0.00E+00	5.59E+04	3.93E+04	0.248
0.005	518.5	0.50	0.03	0.00025	0.02	0.044	0.521	0.0301	0.0126	5.52E+00	7.02E+04	7.26E+04	0.00E+00	3.78E+04	3.48E+04	0.347
0.005	800.7	0.50	0.03	0.00025	0.01	0.035	0.376	0.0241	0.0070	6.85E+00	5.11E+04	5.12E+04	0.00E+00	2.77E+04	2.35E+04	0.456
0.005	1171.1	0.50	0.03	0.00025	0.01	0.027	0.265	0.0115	0.0115	7.72E+00	3.69E+04	3.72E+04	0.00E+00	2.62E+04	1.10E+04	0.577
0.005	1676.6	0.50	0.03	0.00025	0.01	0.020	0.199	0.0059	0.0059	8.23E+00	2.59E+04	2.72E+04	0.00E+00	2.35E+04	3.71E+03	0.712
0.005	2367.9	0.50	0.03	0.00025	0.00	0.012	0.120	0.0020	0.0020	6.69E+00	1.44E+04	1.57E+04	0.00E+00	1.54E+04	3.59E+02	0.865
0.005	3309.8	0.50	0.04	0.00025	0.00	0.007	0.085	0.0012	0.0012	5.27E+00	7.98E+03	1.07E+04	0.00E+00	1.07E+04	5.94E+01	1.040
0.005	4616.9	0.50	0.06	0.00025	0.00	0.004	0.068	0.0015	0.0015	4.12E+00	4.48E+03	1.07E+04	0.00E+00	1.06E+04	6.69E+01	1.241
0.005	6462.5	0.50	0.07	0.00025	0.00	0.002	0.047	0.0004	0.0004	3.23E+00	2.52E+03	2.67E+03	0.00E+00	2.67E+03	5.82E-04	1.476

Table 6: Integrated magnitude and colours of galaxy models

$M_{L,T,12}$	$\nu(r_{j/2})$	$\tau(r_{j/2})$	$M_{L,t}$	Age	M_{bol}	M_V	(U-B)	(B-V)	(V-R)	(V-I)	(V-J)	(V-H)	(V-K)	(1550-V)	$r_{j/2}$
(1)	(2)	(3)	(4)	(5)	(6)	(7)	(8)	(9)	(10)	(11)	(12)	(13)	(14)	(15)	(16)
3.0	7.10	0.74	0.14550	15.000	-22.017	-21.072	0.615	1.005	0.613	1.235	2.531	3.260	3.487	2.005	0.06
3.0	50.00	0.29	0.15000	15.000	-21.783	-20.917	0.644	1.031	0.608	1.223	2.444	3.170	3.379	4.148	0.16
3.0	111.60	0.18	0.15010	15.000	-21.680	-20.836	0.609	1.017	0.602	1.212	2.411	3.135	3.339	4.047	0.25
3.0	198.60	0.13	0.14990	15.000	-21.544	-20.724	0.569	0.999	0.596	1.200	2.375	3.096	3.296	3.963	0.35
3.0	325.50	0.10	0.15000	15.000	-21.325	-20.532	0.522	0.978	0.587	1.184	2.334	3.050	3.246	3.868	0.46
3.0	501.40	0.14	0.15000	15.000	-20.239	-19.529	0.415	0.923	0.565	1.142	2.206	2.908	3.088	3.703	0.58
3.0	753.80	0.20	0.15000	15.000	-19.084	-18.555	0.248	0.816	0.518	1.053	1.903	2.561	2.692	3.455	0.71
3.0	1116.00	0.27	0.15000	15.000	-18.216	-17.806	0.165	0.761	0.491	0.998	1.690	2.288	2.387	3.396	0.87
3.0	1632.90	0.35	0.15020	15.000	-17.990	-17.551	0.189	0.778	0.499	1.014	1.743	2.362	2.467	3.425	1.04
3.0	2383.70	0.46	0.14990	15.000	-17.558	-17.107	0.192	0.776	0.499	1.015	1.764	2.389	2.497	3.389	1.24
3.0	3493.20	0.59	0.15020	15.000	-17.248	-16.771	0.214	0.792	0.507	1.030	1.809	2.450	2.562	3.418	1.48
3.0	7.10	0.74	0.14550	10.000	-22.456	-21.497	0.558	0.960	0.596	1.212	2.574	3.311	3.549	3.553	0.06
3.0	50.00	0.29	0.15000	10.000	-22.170	-21.280	0.572	0.999	0.593	1.199	2.484	3.219	3.441	5.946	0.16
3.0	111.60	0.18	0.15010	10.000	-22.055	-21.193	0.543	0.987	0.588	1.189	2.444	3.177	3.394	5.907	0.25
3.0	198.60	0.13	0.14990	10.000	-21.913	-21.078	0.509	0.973	0.582	1.178	2.404	3.133	3.345	5.860	0.35
3.0	325.50	0.10	0.15000	10.000	-21.688	-20.884	0.467	0.956	0.574	1.163	2.358	3.082	3.288	5.793	0.46
3.0	501.40	0.14	0.15000	10.000	-20.592	-19.879	0.372	0.910	0.555	1.125	2.221	2.929	3.116	5.675	0.58
3.0	753.80	0.20	0.15000	10.000	-19.429	-18.904	0.218	0.823	0.516	1.047	1.911	2.575	2.707	5.419	0.71
3.0	1116.00	0.27	0.15000	10.000	-18.555	-18.146	0.142	0.776	0.492	1.001	1.703	2.308	2.405	5.328	0.87
3.0	1632.90	0.35	0.15020	10.000	-18.333	-17.895	0.165	0.790	0.499	1.015	1.755	2.381	2.484	5.375	1.04
3.0	2383.70	0.46	0.14990	10.000	-17.902	-17.452	0.166	0.790	0.500	1.016	1.776	2.408	2.515	5.330	1.24
3.0	3493.20	0.59	0.15020	10.000	-17.594	-17.120	0.188	0.803	0.507	1.028	1.819	2.468	2.579	5.375	1.48
3.0	7.10	0.74	0.14550	5.000	-23.556	-22.462	0.143	0.726	0.514	1.092	2.594	3.340	3.609	-0.041	0.06
3.0	50.00	0.29	0.15000	5.000	-22.833	-21.951	0.452	0.932	0.562	1.149	2.473	3.213	3.445	6.249	0.16
3.0	111.60	0.18	0.15010	5.000	-22.691	-21.841	0.428	0.920	0.556	1.138	2.427	3.164	3.388	6.076	0.25
3.0	198.60	0.13	0.14990	5.000	-22.535	-21.714	0.402	0.907	0.551	1.126	2.384	3.117	3.336	5.870	0.35
3.0	325.50	0.10	0.15000	5.000	-22.300	-21.511	0.371	0.890	0.544	1.112	2.336	3.064	3.277	5.614	0.46
3.0	501.40	0.14	0.15000	5.000	-21.188	-20.490	0.294	0.845	0.525	1.074	2.195	2.908	3.101	5.197	0.58
3.0	753.80	0.20	0.15000	5.000	-19.985	-19.485	0.161	0.753	0.484	0.990	1.859	2.523	2.659	4.589	0.71
3.0	1116.00	0.27	0.15000	5.000	-19.133	-18.732	0.105	0.711	0.463	0.954	1.672	2.287	2.385	4.365	0.87
3.0	1632.90	0.35	0.15020	5.000	-18.897	-18.475	0.120	0.722	0.468	0.963	1.712	2.343	2.447	4.452	1.04
3.0	2383.70	0.46	0.14990	5.000	-18.456	-18.030	0.120	0.721	0.468	0.960	1.721	2.354	2.462	4.407	1.24
3.0	3493.20	0.59	0.15020	5.000	-18.137	-17.692	0.133	0.731	0.473	0.968	1.756	2.402	2.514	4.491	1.48
1.0	9.00	0.52	0.04850	15.000	-20.780	-19.854	0.620	1.011	0.611	1.232	2.509	3.237	3.460	2.285	0.06
1.0	60.60	0.20	0.05001	15.000	-20.563	-19.712	0.620	1.021	0.604	1.215	2.422	3.146	3.352	4.090	0.16
1.0	132.80	0.13	0.05002	15.000	-20.441	-19.617	0.575	1.002	0.597	1.202	2.380	3.102	3.302	3.988	0.25
1.0	233.30	0.09	0.04995	15.000	-20.265	-19.471	0.526	0.980	0.588	1.186	2.336	3.053	3.249	3.889	0.35
1.0	378.30	0.07	0.05001	15.000	-20.010	-19.286	0.440	0.935	0.570	1.152	2.228	2.935	3.116	3.778	0.46
1.0	577.30	0.10	0.05001	15.000	-19.088	-18.437	0.351	0.884	0.549	1.112	2.109	2.800	2.965	3.606	0.58
1.0	860.30	0.14	0.04999	15.000	-18.478	-17.865	0.293	0.850	0.534	1.085	2.050	2.722	2.887	3.498	0.71
1.0	1262.80	0.19	0.05000	15.000	-17.591	-17.162	0.188	0.781	0.500	1.015	1.724	2.336	2.437	3.472	0.87
1.0	1832.50	0.24	0.05006	15.000	-17.188	-16.747	0.190	0.778	0.499	1.015	1.746	2.365	2.470	3.425	1.04
1.0	2653.10	0.32	0.04997	15.000	-16.802	-16.348	0.195	0.780	0.501	1.017	1.768	2.394	2.503	3.402	1.24
1.0	3855.90	0.41	0.05007	15.000	-15.794	-15.425	0.107	0.704	0.465	0.948	1.609	2.170	2.266	3.174	1.48
1.0	9.00	0.52	0.04850	10.000	-21.201	-20.263	0.538	0.959	0.593	1.204	2.540	3.275	3.509	2.849	0.06
1.0	60.60	0.20	0.05001	10.000	-20.943	-20.071	0.553	0.991	0.590	1.193	2.459	3.192	3.411	5.920	0.16
1.0	132.80	0.13	0.05002	10.000	-20.813	-19.972	0.514	0.976	0.583	1.180	2.412	3.141	3.354	5.868	0.25
1.0	233.30	0.09	0.04995	10.000	-20.630	-19.824	0.471	0.957	0.575	1.165	2.363	3.087	3.294	5.804	0.35
1.0	378.30	0.07	0.05001	10.000	-20.373	-19.638	0.396	0.921	0.560	1.136	2.252	2.966	3.157	5.718	0.46
1.0	577.30	0.10	0.05001	10.000	-19.441	-18.788	0.314	0.879	0.542	1.098	2.123	2.821	2.992	5.569	0.58
1.0	860.30	0.14	0.04999	10.000	-18.821	-18.210	0.260	0.852	0.529	1.074	2.059	2.736	2.906	5.442	0.71
1.0	1262.80	0.19	0.05000	10.000	-17.931	-17.504	0.166	0.791	0.499	1.016	1.736	2.355	2.454	5.435	0.87
1.0	1832.50	0.24	0.05006	10.000	-17.530	-17.091	0.165	0.790	0.499	1.015	1.757	2.384	2.487	5.375	1.04
1.0	2653.10	0.32	0.04997	10.000	-17.146	-16.694	0.170	0.792	0.501	1.018	1.779	2.413	2.520	5.348	1.24
1.0	3855.90	0.41	0.05007	10.000	-16.133	-15.764	0.081	0.734	0.473	0.960	1.628	2.194	2.288	5.035	1.48
1.0	9.00	0.52	0.04850	5.000	-21.988	-21.022	0.432	0.900	0.564	1.163	2.587	3.333	3.582	6.346	0.06

Table 6: Integrated magnitude and colours of galaxy models *continued*

(1)	(2)	(3)	(4)	(5)	(6)	(7)	(8)	(9)	(10)	(11)	(12)	(13)	(14)	(15)	(16)
1.0	60.60	0.20	0.05001	5.000	-21.586	-20.725	0.436	0.924	0.558	1.141	2.442	3.180	3.408	6.138	0.16
1.0	132.80	0.13	0.05002	5.000	-21.436	-20.609	0.406	0.909	0.552	1.128	2.392	3.126	3.347	5.906	0.25
1.0	233.30	0.09	0.04995	5.000	-21.242	-20.450	0.373	0.891	0.544	1.113	2.340	3.069	3.283	5.650	0.35
1.0	378.30	0.07	0.05001	5.000	-20.962	-20.245	0.308	0.853	0.529	1.081	2.224	2.942	3.140	5.332	0.46
1.0	577.30	0.10	0.05001	5.000	-20.017	-19.384	0.243	0.811	0.510	1.044	2.087	2.787	2.965	4.941	0.58
1.0	860.30	0.14	0.04999	5.000	-19.417	-18.817	0.209	0.790	0.501	1.028	2.034	2.719	2.892	4.676	0.71
1.0	1262.80	0.19	0.05000	5.000	-18.505	-18.086	0.122	0.725	0.469	0.966	1.705	2.335	2.436	4.516	0.87
1.0	1832.50	0.24	0.05006	5.000	-18.094	-17.671	0.120	0.723	0.469	0.963	1.713	2.345	2.450	4.453	1.04
1.0	2653.10	0.32	0.04997	5.000	-17.700	-17.271	0.122	0.723	0.469	0.962	1.725	2.360	2.468	4.431	1.24
1.0	3855.90	0.41	0.05007	5.000	-16.711	-16.355	0.061	0.672	0.445	0.914	1.581	2.153	2.246	3.994	1.48
0.5	10.40	0.42	0.02425	15.000	-19.993	-19.084	0.622	1.014	0.610	1.229	2.490	3.217	3.437	2.555	0.06
0.5	68.30	0.16	0.02500	15.000	-19.771	-18.934	0.599	1.012	0.601	1.209	2.401	3.125	3.328	4.046	0.16
0.5	148.30	0.10	0.02501	15.000	-19.652	-18.846	0.549	0.990	0.592	1.193	2.356	3.074	3.272	3.946	0.25
0.5	258.50	0.07	0.02498	15.000	-19.514	-18.753	0.484	0.958	0.580	1.170	2.286	2.998	3.187	3.849	0.35
0.5	416.30	0.06	0.02500	15.000	-19.279	-18.565	0.419	0.925	0.566	1.145	2.213	2.915	3.096	3.745	0.46
0.5	631.60	0.08	0.02500	15.000	-18.706	-18.047	0.364	0.891	0.552	1.118	2.123	2.817	2.984	3.636	0.58
0.5	936.10	0.11	0.02499	15.000	-17.271	-16.884	0.137	0.736	0.479	0.976	1.647	2.226	2.323	3.301	0.71
0.5	1366.90	0.15	0.02500	15.000	-17.218	-16.779	0.202	0.792	0.504	1.025	1.745	2.366	2.469	3.512	0.87
0.5	1973.40	0.20	0.02503	15.000	-16.803	-16.351	0.204	0.790	0.504	1.025	1.767	2.394	2.501	3.464	1.04
0.5	2842.60	0.25	0.02498	15.000	-15.572	-15.221	0.091	0.689	0.458	0.933	1.575	2.118	2.212	3.128	1.24
0.5	4110.10	0.33	0.02503	15.000	-15.114	-14.783	0.076	0.675	0.450	0.919	1.535	2.059	2.149	3.095	1.48
0.5	10.40	0.42	0.02425	10.000	-20.404	-19.478	0.540	0.969	0.593	1.203	2.522	3.257	3.488	2.834	0.06
0.5	68.30	0.16	0.02500	10.000	-20.148	-19.290	0.535	0.984	0.587	1.187	2.436	3.168	3.384	5.902	0.16
0.5	148.30	0.10	0.02501	10.000	-20.022	-19.199	0.491	0.966	0.579	1.172	2.386	3.113	3.323	5.839	0.25
0.5	258.50	0.07	0.02498	10.000	-19.880	-19.105	0.435	0.940	0.569	1.152	2.314	3.034	3.234	5.764	0.35
0.5	416.30	0.06	0.02500	10.000	-19.638	-18.915	0.377	0.913	0.557	1.129	2.236	2.945	3.136	5.681	0.46
0.5	631.60	0.08	0.02500	10.000	-19.063	-18.399	0.326	0.885	0.545	1.104	2.141	2.842	3.015	5.593	0.58
0.5	936.10	0.11	0.02499	10.000	-17.610	-17.223	0.113	0.756	0.483	0.983	1.663	2.248	2.342	5.197	0.71
0.5	1366.90	0.15	0.02500	10.000	-17.559	-17.121	0.179	0.799	0.503	1.023	1.756	2.384	2.485	5.493	0.87
0.5	1973.40	0.20	0.02503	10.000	-17.146	-16.696	0.180	0.799	0.503	1.023	1.778	2.413	2.517	5.431	1.04
0.5	2842.60	0.25	0.02498	10.000	-15.910	-15.559	0.064	0.721	0.467	0.947	1.595	2.143	2.234	4.974	1.24
0.5	4110.10	0.33	0.02503	10.000	-15.450	-15.119	0.048	0.710	0.461	0.936	1.557	2.085	2.172	4.930	1.48
0.5	10.40	0.42	0.02425	5.000	-21.146	-20.201	0.444	0.914	0.565	1.162	2.560	3.305	3.550	6.294	0.06
0.5	68.30	0.16	0.02500	5.000	-20.781	-19.936	0.422	0.917	0.555	1.135	2.418	3.155	3.379	6.043	0.16
0.5	148.30	0.10	0.02501	5.000	-20.639	-19.830	0.388	0.899	0.548	1.120	2.365	3.096	3.314	5.778	0.25
0.5	258.50	0.07	0.02498	5.000	-20.481	-19.722	0.342	0.873	0.537	1.098	2.289	3.013	3.221	5.496	0.35
0.5	416.30	0.06	0.02500	5.000	-20.235	-19.526	0.298	0.847	0.526	1.077	2.212	2.926	3.124	5.222	0.46
0.5	631.60	0.08	0.02500	5.000	-19.637	-18.994	0.251	0.816	0.513	1.048	2.104	2.807	2.988	5.000	0.58
0.5	936.10	0.11	0.02499	5.000	-18.191	-17.812	0.085	0.694	0.455	0.937	1.629	2.225	2.319	4.192	0.71
0.5	1366.90	0.15	0.02500	5.000	-18.130	-17.701	0.132	0.733	0.473	0.973	1.724	2.362	2.465	4.604	0.87
0.5	1973.40	0.20	0.02503	5.000	-17.706	-17.273	0.130	0.730	0.472	0.970	1.733	2.372	2.479	4.537	1.04
0.5	2842.60	0.25	0.02498	5.000	-16.493	-16.153	0.049	0.661	0.440	0.903	1.549	2.104	2.193	3.918	1.24
0.5	4110.10	0.33	0.02503	5.000	-16.041	-15.716	0.039	0.652	0.436	0.894	1.516	2.054	2.139	3.860	1.48
0.1	14.70	0.25	0.00485	15.000	-18.186	-17.312	0.608	1.011	0.606	1.219	2.446	3.171	3.383	2.998	0.06
0.1	90.60	0.10	0.00500	15.000	-17.977	-17.171	0.549	0.990	0.592	1.193	2.355	3.073	3.271	3.961	0.16
0.1	191.90	0.06	0.00500	15.000	-17.826	-17.070	0.472	0.952	0.578	1.166	2.279	2.988	3.178	3.832	0.25
0.1	328.70	0.04	0.00500	15.000	-17.694	-17.011	0.388	0.905	0.559	1.130	2.163	2.860	3.034	3.709	0.35
0.1	521.40	0.03	0.00500	15.000	-17.575	-16.926	0.330	0.870	0.544	1.104	2.109	2.794	2.965	3.577	0.46
0.1	780.80	0.05	0.00500	15.000	-16.737	-16.355	0.131	0.729	0.476	0.970	1.637	2.211	2.307	3.278	0.58
0.1	1142.80	0.07	0.00500	15.000	-16.415	-15.989	0.187	0.780	0.499	1.014	1.720	2.331	2.432	3.473	0.71
0.1	1648.80	0.09	0.00500	15.000	-16.110	-15.656	0.214	0.800	0.508	1.032	1.770	2.399	2.504	3.527	0.87
0.1	2352.90	0.12	0.00501	15.000	-14.500	-14.191	0.056	0.654	0.439	0.897	1.490	1.989	2.076	3.027	1.04
0.1	3350.20	0.15	0.00500	15.000	-14.214	-13.898	0.063	0.661	0.443	0.904	1.506	2.013	2.101	3.050	1.24
0.1	4787.80	0.20	0.00501	15.000	-13.933	-13.607	0.071	0.670	0.448	0.914	1.525	2.044	2.133	3.079	1.48
0.1	14.70	0.25	0.00485	10.000	-18.582	-17.686	0.535	0.976	0.591	1.196	2.483	3.217	3.442	3.212	0.06
0.1	90.60	0.10	0.00500	10.000	-18.349	-17.525	0.492	0.966	0.579	1.173	2.388	3.115	3.325	5.841	0.16
0.1	191.90	0.06	0.00500	10.000	-18.192	-17.422	0.424	0.936	0.567	1.149	2.308	3.026	3.226	5.736	0.25
0.1	328.70	0.04	0.00500	10.000	-18.058	-17.363	0.349	0.898	0.551	1.117	2.191	2.897	3.080	5.627	0.35
0.1	521.40	0.03	0.00500	10.000	-17.936	-17.275	0.296	0.870	0.540	1.095	2.137	2.830	3.010	5.469	0.46
0.1	780.80	0.05	0.00500	10.000	-17.075	-16.694	0.106	0.751	0.481	0.978	1.652	2.233	2.326	5.167	0.58
0.1	1142.80	0.07	0.00500	10.000	-16.755	-16.330	0.164	0.790	0.498	1.015	1.732	2.350	2.448	5.435	0.71

Table 6: Integrated magnitude and colours of galaxy models *continued*

(1)	(2)	(3)	(4)	(5)	(6)	(7)	(8)	(9)	(10)	(11)	(12)	(13)	(14)	(15)	(16)
0.1	1648.80	0.09	0.00500	10.000	-16.452	-16.000	0.191	0.806	0.506	1.030	1.779	2.416	2.520	5.518	0.87
0.1	2352.90	0.12	0.00501	10.000	-14.835	-14.526	0.026	0.693	0.453	0.917	1.514	2.017	2.100	4.845	1.04
0.1	3350.20	0.15	0.00500	10.000	-14.549	-14.233	0.033	0.699	0.455	0.923	1.528	2.041	2.125	4.873	1.24
0.1	4787.80	0.20	0.00501	10.000	-14.269	-13.943	0.043	0.706	0.459	0.931	1.547	2.070	2.156	4.910	1.48
0.1	14.70	0.25	0.00485	5.000	-19.259	-18.361	0.436	0.917	0.561	1.151	2.494	3.235	3.471	6.166	0.06
0.1	90.60	0.10	0.00500	5.000	-18.966	-18.156	0.388	0.899	0.548	1.120	2.367	3.098	3.316	5.788	0.16
0.1	191.90	0.06	0.00500	5.000	-18.795	-18.039	0.335	0.869	0.536	1.096	2.284	3.007	3.215	5.417	0.25
0.1	328.70	0.04	0.00500	5.000	-18.639	-17.962	0.270	0.828	0.519	1.061	2.160	2.868	3.059	5.095	0.35
0.1	521.40	0.03	0.00500	5.000	-18.520	-17.877	0.233	0.804	0.509	1.041	2.105	2.801	2.988	4.775	0.46
0.1	780.80	0.05	0.00500	5.000	-17.657	-17.283	0.080	0.689	0.453	0.932	1.618	2.208	2.302	4.152	0.58
0.1	1142.80	0.07	0.00500	5.000	-17.330	-16.913	0.121	0.725	0.469	0.966	1.703	2.332	2.432	4.514	0.71
0.1	1648.80	0.09	0.00500	5.000	-17.016	-16.578	0.139	0.738	0.475	0.977	1.742	2.387	2.492	4.653	0.87
0.1	2352.90	0.12	0.00501	5.000	-15.429	-15.126	0.023	0.636	0.428	0.878	1.471	1.984	2.063	3.758	1.04
0.1	3350.20	0.15	0.00500	5.000	-15.142	-14.832	0.028	0.641	0.431	0.883	1.487	2.008	2.089	3.791	1.24
0.1	4787.80	0.20	0.00501	5.000	-14.860	-14.541	0.035	0.648	0.434	0.890	1.506	2.039	2.122	3.836	1.48
0.05	17.00	0.20	0.00243	15.000	-17.406	-16.548	0.598	1.008	0.603	1.214	2.425	3.149	3.358	3.232	0.06
0.05	102.40	0.08	0.00250	15.000	-17.179	-16.393	0.517	0.975	0.586	1.182	2.323	3.039	3.233	3.912	0.16
0.05	214.60	0.05	0.00250	15.000	-17.057	-16.331	0.437	0.933	0.570	1.152	2.231	2.936	3.119	3.794	0.25
0.05	364.90	0.03	0.00250	15.000	-16.934	-16.253	0.363	0.893	0.554	1.122	2.163	2.852	3.033	3.658	0.35
0.05	575.20	0.03	0.00250	15.000	-16.777	-16.210	0.230	0.803	0.515	1.049	1.974	2.623	2.787	3.400	0.46
0.05	856.50	0.04	0.00250	15.000	-16.206	-15.813	0.144	0.742	0.482	0.982	1.659	2.243	2.340	3.325	0.58
0.05	1247.10	0.05	0.00250	15.000	-15.801	-15.367	0.198	0.790	0.503	1.022	1.735	2.351	2.453	3.512	0.71
0.05	1790.20	0.07	0.00250	15.000	-15.583	-15.126	0.216	0.801	0.509	1.033	1.777	2.408	2.514	3.521	0.87
0.05	2542.10	0.09	0.00250	15.000	-13.983	-13.675	0.056	0.654	0.440	0.897	1.491	1.991	2.077	3.028	1.04
0.05	3602.20	0.12	0.00250	15.000	-13.701	-13.385	0.062	0.661	0.443	0.904	1.505	2.013	2.100	3.049	1.24
0.05	5122.60	0.16	0.00250	15.000	-13.421	-13.097	0.070	0.669	0.447	0.912	1.522	2.040	2.128	3.075	1.48
0.05	17.00	0.20	0.00243	10.000	-17.798	-16.916	0.530	0.977	0.589	1.192	2.464	3.197	3.419	3.536	0.06
0.05	102.40	0.08	0.00250	10.000	-17.548	-16.746	0.464	0.954	0.574	1.163	2.355	3.078	3.284	5.806	0.16
0.05	214.60	0.05	0.00250	10.000	-17.424	-16.683	0.394	0.920	0.561	1.137	2.262	2.976	3.170	5.696	0.25
0.05	364.90	0.03	0.00250	10.000	-17.294	-16.600	0.327	0.888	0.547	1.111	2.192	2.889	3.080	5.548	0.35
0.05	575.20	0.03	0.00250	10.000	-17.131	-16.553	0.201	0.817	0.515	1.048	2.005	2.663	2.835	5.249	0.46
0.05	856.50	0.04	0.00250	10.000	-16.545	-16.152	0.120	0.761	0.485	0.988	1.673	2.264	2.359	5.229	0.58
0.05	1247.10	0.05	0.00250	10.000	-16.141	-15.709	0.175	0.797	0.501	1.021	1.745	2.370	2.469	5.491	0.71
0.05	1790.20	0.07	0.00250	10.000	-15.926	-15.470	0.192	0.807	0.507	1.031	1.786	2.426	2.530	5.510	0.87
0.05	2542.10	0.09	0.00250	10.000	-14.319	-14.009	0.027	0.693	0.453	0.918	1.514	2.018	2.101	4.846	1.04
0.05	3602.20	0.12	0.00250	10.000	-14.037	-13.720	0.033	0.699	0.455	0.923	1.528	2.040	2.124	4.872	1.24
0.05	5122.60	0.16	0.00250	10.000	-13.757	-13.433	0.042	0.705	0.459	0.930	1.544	2.066	2.151	4.905	1.48
0.05	17.00	0.20	0.00243	5.000	-18.453	-17.576	0.427	0.914	0.558	1.144	2.463	3.202	3.434	6.102	0.06
0.05	102.40	0.08	0.00250	5.000	-18.158	-17.371	0.366	0.887	0.543	1.111	2.333	3.061	3.275	5.643	0.16
0.05	214.60	0.05	0.00250	5.000	-18.016	-17.292	0.308	0.852	0.529	1.082	2.236	2.953	3.155	5.291	0.25
0.05	364.90	0.03	0.00250	5.000	-17.897	-17.213	0.263	0.825	0.517	1.062	2.171	2.874	3.071	4.925	0.35
0.05	575.20	0.03	0.00250	5.000	-17.732	-17.162	0.165	0.757	0.488	1.003	1.982	2.647	2.825	4.371	0.46
0.05	856.50	0.04	0.00250	5.000	-17.125	-16.740	0.090	0.698	0.457	0.941	1.640	2.241	2.337	4.233	0.58
0.05	1247.10	0.05	0.00250	5.000	-16.715	-16.290	0.129	0.731	0.472	0.972	1.717	2.352	2.454	4.593	0.71
0.05	1790.20	0.07	0.00250	5.000	-16.488	-16.048	0.140	0.738	0.475	0.977	1.746	2.392	2.498	4.648	0.87
0.05	2542.10	0.09	0.00250	5.000	-14.913	-14.610	0.023	0.637	0.428	0.878	1.472	1.985	2.065	3.760	1.04
0.05	3602.20	0.12	0.00250	5.000	-14.629	-14.319	0.028	0.641	0.431	0.883	1.486	2.007	2.089	3.790	1.24
0.05	5122.60	0.16	0.00250	5.000	-14.349	-14.031	0.034	0.647	0.434	0.889	1.503	2.034	2.117	3.829	1.48
0.005	27.70	0.09	0.00024	15.000	-14.839	-14.030	0.547	0.988	0.593	1.194	2.358	3.076	3.275	3.776	0.06
0.005	154.10	0.04	0.00025	15.000	-14.600	-13.908	0.395	0.910	0.561	1.134	2.178	2.875	3.053	3.739	0.16
0.005	312.30	0.03	0.00025	15.000	-14.442	-13.816	0.303	0.855	0.538	1.091	2.072	2.746	2.916	3.555	0.25
0.005	518.50	0.03	0.00025	15.000	-14.143	-13.596	0.221	0.796	0.511	1.041	1.940	2.587	2.742	3.366	0.35
0.005	800.70	0.03	0.00025	15.000	-13.825	-13.358	0.171	0.761	0.493	1.005	1.798	2.412	2.544	3.315	0.46
0.005	1171.10	0.03	0.00025	15.000	-13.316	-12.940	0.123	0.722	0.473	0.964	1.625	2.194	2.290	3.252	0.58
0.005	1676.60	0.03	0.00025	15.000	-13.309	-12.926	0.123	0.720	0.473	0.963	1.638	2.211	2.309	3.227	0.71
0.005	2367.90	0.03	0.00025	15.000	-12.544	-12.237	0.054	0.651	0.438	0.894	1.486	1.982	2.069	3.021	0.87
0.005	3309.80	0.04	0.00025	15.000	-12.264	-11.953	0.058	0.656	0.441	0.899	1.496	1.998	2.085	3.035	1.04
0.005	4616.90	0.06	0.00025	15.000	-11.985	-11.669	0.063	0.661	0.443	0.905	1.507	2.015	2.103	3.051	1.24
0.005	27.70	0.09	0.00024	10.000	-15.220	-14.387	0.491	0.964	0.581	1.176	2.398	3.126	3.338	4.778	0.06
0.005	154.10	0.04	0.00025	10.000	-14.966	-14.258	0.356	0.902	0.553	1.122	2.210	2.916	3.103	5.641	0.16
0.005	312.30	0.03	0.00025	10.000	-14.800	-14.162	0.271	0.857	0.533	1.084	2.101	2.784	2.962	5.438	0.25

Table 6: Integrated magnitude and colours of galaxy models *continued*

(1)	(2)	(3)	(4)	(5)	(6)	(7)	(8)	(9)	(10)	(11)	(12)	(13)	(14)	(15)	(16)
0.005	518.50	0.03	0.00025	10.000	-14.491	-13.939	0.191	0.810	0.511	1.039	1.962	2.614	2.775	5.243	0.35
0.005	800.70	0.03	0.00025	10.000	-14.167	-13.698	0.144	0.779	0.495	1.008	1.817	2.437	2.572	5.196	0.46
0.005	1171.10	0.03	0.00025	10.000	-13.654	-13.278	0.098	0.746	0.478	0.973	1.642	2.216	2.309	5.134	0.58
0.005	1676.60	0.03	0.00025	10.000	-13.649	-13.266	0.098	0.745	0.479	0.972	1.654	2.234	2.330	5.103	0.71
0.005	2367.90	0.03	0.00025	10.000	-12.879	-12.572	0.024	0.692	0.452	0.915	1.509	2.010	2.093	4.837	0.87
0.005	3309.80	0.04	0.00025	10.000	-12.600	-12.288	0.029	0.695	0.454	0.919	1.519	2.025	2.109	4.854	1.04
0.005	4616.90	0.06	0.00025	10.000	-12.321	-12.004	0.034	0.699	0.456	0.924	1.529	2.042	2.126	4.874	1.24
0.005	6462.50	0.07	0.00025	10.000	-11.673	-11.360	0.029	0.696	0.454	0.920	1.520	2.027	2.110	4.856	1.48
0.005	27.70	0.09	0.00024	5.000	-15.839	-15.019	0.388	0.897	0.548	1.122	2.380	3.112	3.333	5.822	0.06
0.005	154.10	0.04	0.00025	5.000	-15.554	-14.863	0.279	0.834	0.521	1.067	2.183	2.893	3.088	5.125	0.16
0.005	312.30	0.03	0.00025	5.000	-15.394	-14.769	0.217	0.794	0.504	1.034	2.076	2.765	2.950	4.693	0.25
0.005	518.50	0.03	0.00025	5.000	-15.084	-14.543	0.155	0.749	0.483	0.993	1.931	2.591	2.756	4.350	0.35
0.005	800.70	0.03	0.00025	5.000	-14.758	-14.296	0.115	0.718	0.468	0.963	1.788	2.418	2.556	4.237	0.46
0.005	1171.10	0.03	0.00025	5.000	-14.237	-13.869	0.075	0.684	0.451	0.928	1.606	2.191	2.284	4.111	0.58
0.005	1676.60	0.03	0.00025	5.000	-14.225	-13.855	0.073	0.682	0.450	0.925	1.610	2.195	2.290	4.081	0.71
0.005	2367.90	0.03	0.00025	5.000	-13.473	-13.173	0.021	0.635	0.428	0.876	1.467	1.976	2.056	3.749	0.87
0.005	3309.80	0.04	0.00025	5.000	-13.193	-12.888	0.025	0.638	0.429	0.880	1.476	1.992	2.072	3.769	1.04
0.005	4616.90	0.06	0.00025	5.000	-12.914	-12.603	0.028	0.642	0.431	0.884	1.487	2.009	2.091	3.793	1.24
0.005	6462.50	0.07	0.00025	5.000	-12.266	-11.960	0.025	0.638	0.429	0.880	1.478	1.994	2.074	3.772	1.48

Table 6: Integrated magnitude and colours cumulated for each shell

$M_{L,T,12}$	$\nu(r_{j/2})$	$\tau(r_{j/2})$	$M_{L,t}$	Age	M_{bol}	M_V	(U-B)	(B-V)	(V-R)	(V-I)	(V-J)	(V-H)	(V-K)	(1550-V)	$r_{j/2}$
(1)	(2)	(3)	(4)	(5)	(6)	(7)	(8)	(9)	(10)	(11)	(12)	(13)	(14)	(15)	(16)
3.0	7.10	0.74	0.14550	15.000	-22.015	-21.072	0.615	1.005	0.613	1.235	2.531	3.260	3.487	2.007	0.06
3.0	50.00	0.29	0.15000	15.000	-22.657	-21.750	0.628	1.017	0.611	1.229	2.492	3.219	3.438	2.562	0.16
3.0	111.60	0.18	0.15010	15.000	-23.027	-22.139	0.622	1.017	0.608	1.224	2.468	3.194	3.409	2.838	0.25
3.0	198.60	0.13	0.14990	15.000	-23.273	-22.400	0.611	1.013	0.605	1.219	2.449	3.174	3.386	2.999	0.35
3.0	325.50	0.10	0.15000	15.000	-23.440	-22.579	0.597	1.008	0.603	1.214	2.432	3.156	3.366	3.094	0.46
3.0	501.40	0.14	0.15000	15.000	-23.495	-22.642	0.585	1.003	0.601	1.210	2.421	3.144	3.352	3.121	0.58
3.0	753.80	0.20	0.15000	15.000	-23.514	-22.667	0.574	0.998	0.599	1.206	2.411	3.133	3.341	3.128	0.71
3.0	1116.00	0.27	0.15000	15.000	-23.522	-22.679	0.567	0.995	0.598	1.204	2.405	3.127	3.334	3.130	0.87
3.0	1632.90	0.35	0.15020	15.000	-23.529	-22.689	0.563	0.993	0.597	1.203	2.401	3.122	3.328	3.132	1.04
3.0	2383.70	0.46	0.14990	15.000	-23.533	-22.695	0.559	0.992	0.596	1.202	2.398	3.119	3.325	3.134	1.24
3.0	3493.20	0.59	0.15020	15.000	-23.536	-22.700	0.557	0.991	0.596	1.201	2.396	3.117	3.323	3.135	1.48
3.0	7.10	0.74	0.14550	10.000	-22.454	-21.497	0.558	0.960	0.596	1.212	2.574	3.311	3.549	3.555	0.06
3.0	50.00	0.29	0.15000	10.000	-23.073	-22.146	0.564	0.977	0.595	1.206	2.534	3.270	3.502	4.111	0.16
3.0	111.60	0.18	0.15010	10.000	-23.431	-22.524	0.558	0.980	0.593	1.201	2.509	3.243	3.471	4.405	0.25
3.0	198.60	0.13	0.14990	10.000	-23.671	-22.778	0.547	0.979	0.591	1.197	2.488	3.221	3.446	4.587	0.35
3.0	325.50	0.10	0.15000	10.000	-23.833	-22.953	0.535	0.975	0.588	1.192	2.469	3.202	3.424	4.701	0.46
3.0	501.40	0.14	0.15000	10.000	-23.886	-23.015	0.525	0.972	0.586	1.188	2.457	3.188	3.409	4.738	0.58
3.0	753.80	0.20	0.15000	10.000	-23.904	-23.039	0.516	0.968	0.585	1.185	2.447	3.178	3.397	4.749	0.71
3.0	1116.00	0.27	0.15000	10.000	-23.912	-23.051	0.510	0.966	0.584	1.183	2.441	3.171	3.390	4.754	0.87
3.0	1632.90	0.35	0.15020	10.000	-23.918	-23.061	0.506	0.964	0.583	1.182	2.437	3.166	3.385	4.758	1.04
3.0	2383.70	0.46	0.14990	10.000	-23.922	-23.067	0.503	0.963	0.583	1.181	2.434	3.163	3.381	4.760	1.24
3.0	3493.20	0.59	0.15020	10.000	-23.925	-23.071	0.502	0.962	0.582	1.180	2.432	3.161	3.379	4.762	1.48
3.0	7.10	0.74	0.14550	5.000	-23.554	-22.462	0.143	0.726	0.514	1.092	2.594	3.340	3.609	-0.039	0.06
3.0	50.00	0.29	0.15000	5.000	-24.004	-22.989	0.239	0.801	0.533	1.114	2.549	3.293	3.549	0.486	0.16
3.0	111.60	0.18	0.15010	5.000	-24.287	-23.313	0.281	0.830	0.539	1.120	2.519	3.261	3.510	0.807	0.25
3.0	198.60	0.13	0.14990	5.000	-24.484	-23.537	0.302	0.844	0.541	1.121	2.495	3.235	3.479	1.029	0.35
3.0	325.50	0.10	0.15000	5.000	-24.620	-23.693	0.310	0.850	0.541	1.120	2.475	3.214	3.454	1.183	0.46
3.0	501.40	0.14	0.15000	5.000	-24.665	-23.748	0.310	0.850	0.541	1.118	2.462	3.201	3.439	1.237	0.58
3.0	753.80	0.20	0.15000	5.000	-24.680	-23.770	0.306	0.848	0.540	1.115	2.453	3.191	3.428	1.257	0.71
3.0	1116.00	0.27	0.15000	5.000	-24.686	-23.780	0.304	0.847	0.539	1.114	2.448	3.185	3.422	1.267	0.87
3.0	1632.90	0.35	0.15020	5.000	-24.691	-23.788	0.302	0.846	0.538	1.113	2.444	3.181	3.417	1.274	1.04
3.0	2383.70	0.46	0.14990	5.000	-24.695	-23.794	0.301	0.845	0.538	1.112	2.442	3.178	3.414	1.280	1.24
3.0	3493.20	0.59	0.15020	5.000	-24.697	-23.798	0.300	0.845	0.538	1.112	2.440	3.176	3.412	1.283	1.48
1.0	9.00	0.52	0.04850	15.000	-20.778	-19.854	0.620	1.011	0.611	1.232	2.509	3.237	3.460	2.287	0.06
1.0	60.60	0.20	0.05001	15.000	-21.427	-20.538	0.620	1.015	0.608	1.224	2.469	3.196	3.411	2.804	0.16
1.0	132.80	0.13	0.05002	15.000	-21.794	-20.925	0.606	1.011	0.605	1.217	2.443	3.168	3.380	3.045	0.25
1.0	233.30	0.09	0.04995	15.000	-22.032	-21.178	0.589	1.005	0.601	1.211	2.422	3.145	3.354	3.174	0.35
1.0	378.30	0.07	0.05001	15.000	-22.188	-21.353	0.564	0.994	0.597	1.202	2.395	3.116	3.321	3.246	0.46
1.0	577.30	0.10	0.05001	15.000	-22.249	-21.424	0.548	0.987	0.594	1.197	2.379	3.099	3.302	3.266	0.58
1.0	860.30	0.14	0.04999	15.000	-22.282	-21.465	0.536	0.981	0.592	1.193	2.369	3.087	3.289	3.273	0.71
1.0	1262.80	0.19	0.05000	15.000	-22.296	-21.485	0.527	0.977	0.590	1.190	2.359	3.077	3.278	3.277	0.87
1.0	1832.50	0.24	0.05006	15.000	-22.306	-21.499	0.521	0.975	0.589	1.188	2.354	3.070	3.271	3.279	1.04
1.0	2653.10	0.32	0.04997	15.000	-22.313	-21.508	0.518	0.973	0.588	1.186	2.350	3.066	3.266	3.280	1.24
1.0	3855.90	0.41	0.05007	15.000	-22.316	-21.512	0.515	0.972	0.588	1.186	2.348	3.064	3.264	3.279	1.48
1.0	9.00	0.52	0.04850	10.000	-21.199	-20.263	0.538	0.959	0.593	1.204	2.540	3.275	3.509	2.851	0.06
1.0	60.60	0.20	0.05001	10.000	-21.831	-20.924	0.545	0.974	0.592	1.199	2.504	3.238	3.465	3.459	0.16
1.0	132.80	0.13	0.05002	10.000	-22.189	-21.302	0.536	0.974	0.589	1.194	2.477	3.210	3.434	3.789	0.25
1.0	233.30	0.09	0.04995	10.000	-22.420	-21.549	0.522	0.971	0.586	1.188	2.455	3.186	3.407	3.994	0.35
1.0	378.30	0.07	0.05001	10.000	-22.574	-21.722	0.502	0.963	0.583	1.180	2.427	3.157	3.373	4.129	0.46
1.0	577.30	0.10	0.05001	10.000	-22.632	-21.792	0.488	0.958	0.580	1.175	2.411	3.138	3.353	4.180	0.58
1.0	860.30	0.14	0.04999	10.000	-22.664	-21.831	0.478	0.954	0.578	1.172	2.400	3.126	3.340	4.207	0.71
1.0	1262.80	0.19	0.05000	10.000	-22.678	-21.851	0.471	0.951	0.577	1.169	2.391	3.116	3.329	4.221	0.87
1.0	1832.50	0.24	0.05006	10.000	-22.688	-21.865	0.466	0.949	0.576	1.167	2.385	3.110	3.321	4.229	1.04
1.0	2653.10	0.32	0.04997	10.000	-22.694	-21.874	0.463	0.947	0.575	1.166	2.381	3.105	3.317	4.235	1.24
1.0	3855.90	0.41	0.05007	10.000	-22.697	-21.878	0.461	0.946	0.575	1.166	2.379	3.103	3.314	4.237	1.48
1.0	9.00	0.52	0.04850	5.000	-21.986	-21.022	0.432	0.900	0.564	1.163	2.587	3.333	3.582	6.348	0.06

Table 6: Integrated magnitude and colours cumulated for each shell *continued*

(1)	(2)	(3)	(4)	(5)	(6)	(7)	(8)	(9)	(10)	(11)	(12)	(13)	(14)	(15)	(16)
1.0	60.60	0.20	0.05001	5.000	-22.556	-21.636	0.434	0.910	0.561	1.154	2.527	3.269	3.510	6.253	0.16
1.0	132.80	0.13	0.05002	5.000	-22.886	-21.992	0.426	0.910	0.559	1.146	2.491	3.231	3.467	6.145	0.25
1.0	233.30	0.09	0.04995	5.000	-23.102	-22.227	0.415	0.906	0.556	1.140	2.463	3.201	3.433	6.030	0.35
1.0	378.30	0.07	0.05001	5.000	-23.243	-22.390	0.399	0.898	0.552	1.132	2.433	3.169	3.397	5.902	0.46
1.0	577.30	0.10	0.05001	5.000	-23.298	-22.456	0.389	0.893	0.550	1.127	2.415	3.150	3.376	5.815	0.58
1.0	860.30	0.14	0.04999	5.000	-23.328	-22.493	0.381	0.889	0.548	1.124	2.404	3.138	3.363	5.749	0.71
1.0	1262.80	0.19	0.05000	5.000	-23.340	-22.512	0.376	0.886	0.547	1.121	2.395	3.128	3.352	5.711	0.87
1.0	1832.50	0.24	0.05006	5.000	-23.349	-22.524	0.372	0.884	0.546	1.120	2.390	3.122	3.345	5.684	1.04
1.0	2653.10	0.32	0.04997	5.000	-23.355	-22.533	0.369	0.883	0.545	1.119	2.386	3.117	3.340	5.666	1.24
1.0	3855.90	0.41	0.05007	5.000	-23.357	-22.536	0.368	0.882	0.545	1.118	2.384	3.115	3.338	5.652	1.48
0.5	10.40	0.42	0.02425	15.000	-19.992	-19.084	0.622	1.014	0.610	1.229	2.490	3.217	3.437	2.556	0.06
0.5	68.30	0.16	0.02500	15.000	-20.639	-19.764	0.612	1.013	0.606	1.220	2.450	3.175	3.387	3.020	0.16
0.5	148.30	0.10	0.02501	15.000	-21.006	-20.152	0.592	1.006	0.602	1.212	2.422	3.146	3.354	3.226	0.25
0.5	258.50	0.07	0.02498	15.000	-21.250	-20.416	0.567	0.996	0.597	1.203	2.394	3.115	3.320	3.333	0.35
0.5	416.30	0.06	0.02500	15.000	-21.414	-20.598	0.542	0.985	0.592	1.194	2.368	3.087	3.289	3.388	0.46
0.5	631.60	0.08	0.02500	15.000	-21.500	-20.697	0.524	0.976	0.589	1.188	2.349	3.066	3.265	3.407	0.58
0.5	936.10	0.11	0.02499	15.000	-21.522	-20.728	0.507	0.968	0.586	1.182	2.334	3.049	3.247	3.404	0.71
0.5	1366.90	0.15	0.02500	15.000	-21.542	-20.757	0.497	0.963	0.584	1.178	2.322	3.036	3.232	3.407	0.87
0.5	1973.40	0.20	0.02503	15.000	-21.556	-20.775	0.490	0.960	0.583	1.176	2.315	3.027	3.223	3.408	1.04
0.5	2842.60	0.25	0.02498	15.000	-21.560	-20.782	0.487	0.958	0.582	1.175	2.312	3.024	3.219	3.406	1.24
0.5	4110.10	0.33	0.02503	15.000	-21.563	-20.786	0.484	0.957	0.581	1.174	2.309	3.021	3.217	3.404	1.48
0.5	10.40	0.42	0.02425	10.000	-20.402	-19.478	0.540	0.969	0.593	1.203	2.522	3.257	3.488	2.836	0.06
0.5	68.30	0.16	0.02500	10.000	-21.034	-20.141	0.538	0.976	0.590	1.196	2.484	3.217	3.442	3.446	0.16
0.5	148.30	0.10	0.02501	10.000	-21.394	-20.522	0.524	0.973	0.587	1.189	2.456	3.187	3.408	3.778	0.25
0.5	258.50	0.07	0.02498	10.000	-21.634	-20.782	0.504	0.966	0.583	1.181	2.427	3.156	3.373	3.992	0.35
0.5	416.30	0.06	0.02500	10.000	-21.794	-20.961	0.483	0.958	0.579	1.173	2.400	3.127	3.340	4.131	0.46
0.5	631.60	0.08	0.02500	10.000	-21.879	-21.059	0.467	0.951	0.576	1.167	2.380	3.105	3.316	4.202	0.58
0.5	936.10	0.11	0.02499	10.000	-21.900	-21.090	0.454	0.945	0.574	1.163	2.365	3.088	3.297	4.221	0.71
0.5	1366.90	0.15	0.02500	10.000	-21.919	-21.118	0.445	0.941	0.572	1.159	2.353	3.075	3.283	4.240	0.87
0.5	1973.40	0.20	0.02503	10.000	-21.933	-21.136	0.439	0.939	0.571	1.157	2.346	3.067	3.273	4.252	1.04
0.5	2842.60	0.25	0.02498	10.000	-21.937	-21.143	0.436	0.937	0.570	1.156	2.343	3.063	3.270	4.255	1.24
0.5	4110.10	0.33	0.02503	10.000	-21.940	-21.147	0.434	0.936	0.570	1.155	2.340	3.060	3.267	4.257	1.48
0.5	10.40	0.42	0.02425	5.000	-21.144	-20.201	0.444	0.914	0.565	1.162	2.560	3.305	3.550	6.296	0.06
0.5	68.30	0.16	0.02500	5.000	-21.729	-20.829	0.434	0.915	0.561	1.150	2.500	3.241	3.478	6.178	0.16
0.5	148.30	0.10	0.02501	5.000	-22.068	-21.193	0.421	0.911	0.557	1.142	2.463	3.202	3.434	6.049	0.25
0.5	258.50	0.07	0.02498	5.000	-22.294	-21.442	0.404	0.903	0.553	1.133	2.430	3.166	3.393	5.911	0.35
0.5	416.30	0.06	0.02500	5.000	-22.445	-21.614	0.387	0.894	0.549	1.125	2.401	3.134	3.358	5.779	0.46
0.5	631.60	0.08	0.02500	5.000	-22.524	-21.707	0.374	0.888	0.546	1.119	2.379	3.111	3.332	5.690	0.58
0.5	936.10	0.11	0.02499	5.000	-22.544	-21.736	0.364	0.882	0.544	1.114	2.364	3.094	3.314	5.606	0.71
0.5	1366.90	0.15	0.02500	5.000	-22.562	-21.763	0.357	0.878	0.542	1.111	2.353	3.081	3.300	5.568	0.87
0.5	1973.40	0.20	0.02503	5.000	-22.575	-21.780	0.352	0.876	0.541	1.109	2.345	3.073	3.291	5.541	1.04
0.5	2842.60	0.25	0.02498	5.000	-22.579	-21.786	0.350	0.874	0.540	1.108	2.342	3.070	3.287	5.521	1.24
0.5	4110.10	0.33	0.02503	5.000	-22.581	-21.790	0.348	0.873	0.540	1.107	2.340	3.067	3.284	5.506	1.48
0.1	14.70	0.25	0.00485	15.000	-18.184	-17.312	0.608	1.011	0.606	1.219	2.446	3.171	3.383	3.000	0.06
0.1	90.60	0.10	0.00500	15.000	-18.838	-17.996	0.580	1.001	0.599	1.207	2.404	3.127	3.332	3.349	0.16
0.1	191.90	0.06	0.00500	15.000	-19.198	-18.382	0.545	0.986	0.593	1.195	2.368	3.087	3.289	3.473	0.25
0.1	328.70	0.04	0.00500	15.000	-19.440	-18.652	0.507	0.968	0.585	1.181	2.326	3.041	3.237	3.521	0.35
0.1	521.40	0.03	0.00500	15.000	-19.619	-18.854	0.472	0.951	0.579	1.168	2.292	3.003	3.196	3.530	0.46
0.1	780.80	0.05	0.00500	15.000	-19.693	-18.957	0.430	0.929	0.570	1.152	2.247	2.950	3.139	3.505	0.58
0.1	1142.80	0.07	0.00500	15.000	-19.745	-19.026	0.411	0.919	0.566	1.144	2.221	2.921	3.107	3.503	0.71
0.1	1648.80	0.09	0.00500	15.000	-19.782	-19.073	0.401	0.914	0.563	1.139	2.205	2.903	3.087	3.504	0.87
0.1	2352.90	0.12	0.00501	15.000	-19.790	-19.085	0.395	0.910	0.562	1.137	2.199	2.896	3.080	3.498	1.04
0.1	3350.20	0.15	0.00500	15.000	-19.797	-19.094	0.391	0.908	0.561	1.135	2.195	2.891	3.074	3.493	1.24
0.1	4787.80	0.20	0.00501	15.000	-19.802	-19.101	0.389	0.906	0.560	1.134	2.192	2.888	3.070	3.490	1.48
0.1	14.70	0.25	0.00485	10.000	-18.580	-17.686	0.535	0.976	0.591	1.196	2.483	3.217	3.442	3.214	0.06
0.1	90.60	0.10	0.00500	10.000	-19.223	-18.361	0.515	0.972	0.585	1.185	2.440	3.171	3.389	3.809	0.16
0.1	191.90	0.06	0.00500	10.000	-19.577	-18.742	0.487	0.961	0.580	1.175	2.403	3.130	3.343	4.116	0.25
0.1	328.70	0.04	0.00500	10.000	-19.817	-19.011	0.454	0.947	0.574	1.162	2.360	3.083	3.291	4.311	0.35
0.1	521.40	0.03	0.00500	10.000	-19.993	-19.211	0.424	0.933	0.568	1.151	2.325	3.044	3.248	4.438	0.46
0.1	780.80	0.05	0.00500	10.000	-20.065	-19.313	0.386	0.916	0.560	1.137	2.279	2.992	3.191	4.487	0.58
0.1	1142.80	0.07	0.00500	10.000	-20.115	-19.380	0.370	0.908	0.557	1.130	2.253	2.962	3.158	4.526	0.71

Table 6: Integrated magnitude and colours cumulated for each shell *continued*

(1)	(2)	(3)	(4)	(5)	(6)	(7)	(8)	(9)	(10)	(11)	(12)	(13)	(14)	(15)	(16)
0.1	1648.80	0.09	0.00500	10.000	-20.151	-19.427	0.361	0.903	0.555	1.126	2.237	2.944	3.137	4.554	0.87
0.1	2352.90	0.12	0.00501	10.000	-20.160	-19.439	0.356	0.901	0.554	1.124	2.231	2.937	3.130	4.557	1.04
0.1	3350.20	0.15	0.00500	10.000	-20.166	-19.448	0.352	0.899	0.553	1.122	2.227	2.932	3.125	4.559	1.24
0.1	4787.80	0.20	0.00501	10.000	-20.170	-19.455	0.350	0.898	0.552	1.121	2.223	2.928	3.121	4.561	1.48
0.1	14.70	0.25	0.00485	5.000	-19.257	-18.361	0.436	0.917	0.561	1.151	2.494	3.235	3.471	6.168	0.06
0.1	90.60	0.10	0.00500	5.000	-19.873	-19.016	0.414	0.909	0.555	1.137	2.438	3.175	3.403	5.980	0.16
0.1	191.90	0.06	0.00500	5.000	-20.215	-19.386	0.390	0.897	0.550	1.125	2.396	3.129	3.352	5.786	0.25
0.1	328.70	0.04	0.00500	5.000	-20.443	-19.645	0.362	0.882	0.543	1.112	2.350	3.079	3.296	5.599	0.35
0.1	521.40	0.03	0.00500	5.000	-20.613	-19.840	0.339	0.869	0.537	1.101	2.313	3.038	3.251	5.414	0.46
0.1	780.80	0.05	0.00500	5.000	-20.682	-19.938	0.310	0.852	0.530	1.087	2.268	2.986	3.195	5.225	0.58
0.1	1142.80	0.07	0.00500	5.000	-20.731	-20.003	0.297	0.844	0.527	1.080	2.242	2.957	3.163	5.168	0.71
0.1	1648.80	0.09	0.00500	5.000	-20.766	-20.049	0.289	0.840	0.525	1.076	2.226	2.939	3.142	5.142	0.87
0.1	2352.90	0.12	0.00501	5.000	-20.774	-20.060	0.285	0.837	0.524	1.075	2.220	2.932	3.135	5.112	1.04
0.1	3350.20	0.15	0.00500	5.000	-20.780	-20.069	0.283	0.836	0.523	1.073	2.215	2.927	3.129	5.092	1.24
0.1	4787.80	0.20	0.00501	5.000	-20.784	-20.076	0.281	0.834	0.523	1.072	2.212	2.923	3.125	5.078	1.48
0.05	17.00	0.20	0.00243	15.000	-17.405	-16.548	0.598	1.008	0.603	1.214	2.425	3.149	3.358	3.234	0.06
0.05	102.40	0.08	0.00250	15.000	-18.049	-17.226	0.559	0.993	0.595	1.199	2.379	3.099	3.302	3.498	0.16
0.05	214.60	0.05	0.00250	15.000	-18.415	-17.621	0.519	0.974	0.588	1.185	2.336	3.052	3.249	3.580	0.25
0.05	364.90	0.03	0.00250	15.000	-18.662	-17.892	0.480	0.956	0.580	1.171	2.300	3.011	3.205	3.597	0.35
0.05	575.20	0.03	0.00250	15.000	-18.838	-18.101	0.427	0.927	0.569	1.151	2.250	2.952	3.142	3.560	0.46
0.05	856.50	0.04	0.00250	15.000	-18.930	-18.226	0.387	0.906	0.560	1.134	2.199	2.894	3.079	3.532	0.58
0.05	1247.10	0.05	0.00250	15.000	-18.989	-18.301	0.372	0.898	0.556	1.127	2.173	2.865	3.047	3.531	0.71
0.05	1790.20	0.07	0.00250	15.000	-19.035	-18.358	0.363	0.892	0.554	1.122	2.156	2.846	3.025	3.531	0.87
0.05	2542.10	0.09	0.00250	15.000	-19.045	-18.372	0.357	0.889	0.553	1.119	2.150	2.838	3.017	3.522	1.04
0.05	3602.20	0.12	0.00250	15.000	-19.053	-18.383	0.353	0.886	0.552	1.117	2.145	2.832	3.011	3.516	1.24
0.05	5122.60	0.16	0.00250	15.000	-19.059	-18.392	0.350	0.885	0.551	1.116	2.141	2.828	3.006	3.512	1.48
0.05	17.00	0.20	0.00243	10.000	-17.796	-16.916	0.530	0.977	0.589	1.192	2.464	3.197	3.419	3.538	0.06
0.05	102.40	0.08	0.00250	10.000	-18.431	-17.587	0.499	0.966	0.582	1.179	2.415	3.144	3.359	4.100	0.16
0.05	214.60	0.05	0.00250	10.000	-18.792	-17.979	0.465	0.952	0.576	1.166	2.371	3.096	3.305	4.389	0.25
0.05	364.90	0.03	0.00250	10.000	-19.036	-18.248	0.432	0.938	0.569	1.154	2.334	3.054	3.259	4.557	0.35
0.05	575.20	0.03	0.00250	10.000	-19.209	-18.455	0.384	0.916	0.560	1.137	2.284	2.995	3.197	4.650	0.46
0.05	856.50	0.04	0.00250	10.000	-19.298	-18.578	0.349	0.898	0.552	1.122	2.233	2.937	3.132	4.699	0.58
0.05	1247.10	0.05	0.00250	10.000	-19.356	-18.652	0.335	0.891	0.549	1.115	2.206	2.907	3.099	4.737	0.71
0.05	1790.20	0.07	0.00250	10.000	-19.401	-18.709	0.327	0.887	0.547	1.111	2.188	2.887	3.076	4.766	0.87
0.05	2542.10	0.09	0.00250	10.000	-19.411	-18.723	0.322	0.884	0.546	1.109	2.182	2.879	3.068	4.767	1.04
0.05	3602.20	0.12	0.00250	10.000	-19.419	-18.734	0.318	0.882	0.545	1.107	2.177	2.873	3.061	4.768	1.24
0.05	5122.60	0.16	0.00250	10.000	-19.425	-18.742	0.315	0.881	0.544	1.106	2.173	2.869	3.057	4.769	1.48
0.05	17.00	0.20	0.00243	5.000	-18.451	-17.576	0.427	0.914	0.558	1.144	2.463	3.202	3.434	6.104	0.06
0.05	102.40	0.08	0.00250	5.000	-19.066	-18.231	0.399	0.902	0.551	1.129	2.406	3.140	3.365	5.872	0.16
0.05	214.60	0.05	0.00250	5.000	-19.416	-18.612	0.370	0.887	0.545	1.115	2.359	3.088	3.307	5.666	0.25
0.05	364.90	0.03	0.00250	5.000	-19.655	-18.877	0.345	0.873	0.539	1.104	2.321	3.045	3.260	5.458	0.35
0.05	575.20	0.03	0.00250	5.000	-19.825	-19.080	0.309	0.852	0.530	1.087	2.270	2.987	3.197	5.179	0.46
0.05	856.50	0.04	0.00250	5.000	-19.912	-19.199	0.281	0.835	0.523	1.073	2.219	2.929	3.133	5.033	0.58
0.05	1247.10	0.05	0.00250	5.000	-19.968	-19.271	0.270	0.828	0.520	1.067	2.193	2.900	3.100	4.999	0.71
0.05	1790.20	0.07	0.00250	5.000	-20.011	-19.326	0.263	0.824	0.518	1.062	2.175	2.880	3.078	4.979	0.87
0.05	2542.10	0.09	0.00250	5.000	-20.021	-19.340	0.259	0.821	0.516	1.060	2.168	2.872	3.069	4.950	1.04
0.05	3602.20	0.12	0.00250	5.000	-20.028	-19.350	0.256	0.819	0.516	1.059	2.163	2.867	3.063	4.930	1.24
0.05	5122.60	0.16	0.00250	5.000	-20.034	-19.358	0.254	0.818	0.515	1.058	2.160	2.862	3.058	4.916	1.48
0.005	27.70	0.09	0.00024	15.000	-14.837	-14.030	0.547	0.988	0.593	1.194	2.358	3.076	3.275	3.778	0.06
0.005	154.10	0.04	0.00025	15.000	-15.477	-14.723	0.470	0.951	0.578	1.166	2.277	2.986	3.176	3.760	0.16
0.005	312.30	0.03	0.00025	15.000	-15.831	-15.114	0.414	0.921	0.566	1.144	2.219	2.919	3.104	3.694	0.25
0.005	518.50	0.03	0.00025	15.000	-16.039	-15.354	0.369	0.895	0.555	1.124	2.169	2.860	3.041	3.621	0.35
0.005	800.70	0.03	0.00025	15.000	-16.171	-15.514	0.337	0.875	0.547	1.109	2.125	2.809	2.985	3.574	0.46
0.005	1171.10	0.03	0.00025	15.000	-16.247	-15.611	0.314	0.862	0.541	1.097	2.090	2.768	2.940	3.543	0.58
0.005	1676.60	0.03	0.00025	15.000	-16.317	-15.699	0.296	0.850	0.536	1.087	2.061	2.734	2.902	3.515	0.71
0.005	2367.90	0.03	0.00025	15.000	-16.350	-15.743	0.284	0.841	0.532	1.080	2.043	2.712	2.879	3.490	0.87
0.005	3309.80	0.04	0.00025	15.000	-16.375	-15.776	0.275	0.835	0.529	1.075	2.030	2.696	2.862	3.474	1.04
0.005	4616.90	0.06	0.00025	15.000	-16.394	-15.800	0.269	0.831	0.528	1.072	2.021	2.685	2.850	3.462	1.24
0.005	6462.50	0.07	0.00025	15.000	-16.404	-15.813	0.266	0.829	0.527	1.070	2.016	2.679	2.843	3.456	1.48
0.005	27.70	0.09	0.00024	10.000	-15.218	-14.387	0.491	0.964	0.581	1.176	2.398	3.126	3.338	4.780	0.06
0.005	154.10	0.04	0.00025	10.000	-15.851	-15.077	0.424	0.935	0.568	1.151	2.314	3.032	3.234	5.104	0.16

Table 6: Integrated magnitude and colours cumulated for each shell *continued*

(1)	(2)	(3)	(4)	(5)	(6)	(7)	(8)	(9)	(10)	(11)	(12)	(13)	(14)	(15)	(16)
0.005	312.30	0.03	0.00025	10.000	-16.200	-15.466	0.373	0.911	0.557	1.131	2.254	2.963	3.159	5.194	0.25
0.005	518.50	0.03	0.00025	10.000	-16.405	-15.704	0.332	0.890	0.549	1.114	2.202	2.903	3.094	5.204	0.35
0.005	800.70	0.03	0.00025	10.000	-16.535	-15.863	0.302	0.874	0.541	1.100	2.157	2.850	3.036	5.203	0.46
0.005	1171.10	0.03	0.00025	10.000	-16.608	-15.959	0.282	0.863	0.536	1.090	2.122	2.809	2.990	5.197	0.58
0.005	1676.60	0.03	0.00025	10.000	-16.677	-16.046	0.265	0.853	0.532	1.081	2.092	2.774	2.951	5.190	0.71
0.005	2367.90	0.03	0.00025	10.000	-16.710	-16.090	0.253	0.847	0.529	1.075	2.074	2.752	2.928	5.173	0.87
0.005	3309.80	0.04	0.00025	10.000	-16.734	-16.122	0.244	0.842	0.527	1.071	2.061	2.736	2.911	5.163	1.04
0.005	4616.90	0.06	0.00025	10.000	-16.752	-16.146	0.239	0.838	0.525	1.068	2.052	2.725	2.898	5.156	1.24
0.005	6462.50	0.07	0.00025	10.000	-16.762	-16.159	0.236	0.837	0.524	1.066	2.047	2.719	2.891	5.151	1.48
0.005	27.70	0.09	0.00024	5.000	-15.837	-15.019	0.388	0.897	0.548	1.122	2.380	3.112	3.333	5.823	0.06
0.005	154.10	0.04	0.00025	5.000	-16.457	-15.696	0.334	0.867	0.536	1.097	2.293	3.015	3.226	5.445	0.16
0.005	312.30	0.03	0.00025	5.000	-16.803	-16.081	0.296	0.845	0.526	1.078	2.233	2.946	3.151	5.162	0.25
0.005	518.50	0.03	0.00025	5.000	-17.005	-16.317	0.265	0.825	0.518	1.062	2.180	2.886	3.084	4.949	0.35
0.005	800.70	0.03	0.00025	5.000	-17.134	-16.474	0.242	0.810	0.512	1.049	2.135	2.833	3.026	4.822	0.46
0.005	1171.10	0.03	0.00025	5.000	-17.207	-16.568	0.225	0.799	0.507	1.040	2.099	2.792	2.981	4.742	0.58
0.005	1676.60	0.03	0.00025	5.000	-17.274	-16.654	0.212	0.790	0.502	1.031	2.069	2.757	2.941	4.675	0.71
0.005	2367.90	0.03	0.00025	5.000	-17.307	-16.697	0.203	0.783	0.500	1.026	2.051	2.735	2.917	4.620	0.87
0.005	3309.80	0.04	0.00025	5.000	-17.331	-16.729	0.196	0.779	0.498	1.022	2.038	2.719	2.900	4.583	1.04
0.005	4616.90	0.06	0.00025	5.000	-17.349	-16.753	0.192	0.776	0.496	1.019	2.028	2.708	2.888	4.558	1.24
0.005	6462.50	0.07	0.00025	5.000	-17.359	-16.766	0.189	0.774	0.495	1.017	2.023	2.701	2.881	4.544	1.48